SILICON-BASED ALLOYS BY CHEMICAL DELITHIATION FOR LITHIUM-ION BATTERIES

by

Leyi Zhao

Submitted in partial fulfilment of the requirements
for the degree of Master of Science

at

Dalhousie University
Halifax, Nova Scotia
February 2016

TABLE OF CONTENTS

LIST OF TABLES

LIST OF FIGURES

ABSTRACT

Li-ion battery research is of great technical and industrial importance. Currently, researchers are seeking negative electrode materials that will lead to higher energy density cells. Si-based alloys are promising candidates. However, the commercialization of Si-based alloys as Li-ion battery negative electrodes is hindered by the volume expansion problem of Si during lithiation. In this work, a chemical delithiation method was studied to prepare amorphous silicon (a-Si) from lithium silicide compounds with alcohol. This method was also utilized to synthesize carbon-silicon (C-Si) and iron-silicon (Fe-Si) alloys as negative electrodes for Li-ion batteries. Using powder X-ray diffraction, Mössbauer spectroscopy, scanning electron microscopy and electrochemical measurements, the structure and electrochemistry of a-Si, C-Si and Fe-Si alloys were investigated. The as-prepared a-Si, C-Si and Fe-Si electrodes displayed improved electrochemical performance and lower volume expansion compared to that of crystalline Si.

LIST OF ABBREVIATIONS AND SYMBOLS

a-Si	Amorphous Silicon
BSE	Backscattered Electron
CCCV	Constant Current, Constant Voltage
CE	Coulombic Efficiency
cr-Si	Crystalline Silicon
CRT	Cathode Ray Tube
CVD	Chemical Vapor Deposition
DEC	Diethyl Carbonate
DMC	Dimethyl Carbonate
EC	Ethylene Carbonate
EFG	Electric Field Gradient
FEC	Monofluoroethylene Carbonate
HWHM	Half Width at Half Maximum
IC	the First Cycle Irreversible Capacity
ICP	Inductively Coupled Plasma
Li-ion	Lithium-ion
LTO	$Li_{4/3}Ti_{5/3}O_4$
NMP	N-Methyl-2-Pyrrolidone
PI	Polyimide
PVDF	Polyvinylidene Fluoride
RC	the First Cycle Reversible Capacity
SEI	Solid-Electrolyte Interphase
PVD	Physical Vapor Deposition
SE	Second Electron

SEM	Scanning Electron Microscopy
XRD	X-ray Diffraction
WC	Tungsten Carbide
°	Degree(s)
°C	Degree(s) Celsius
at.%	Atomic Percent
A	Area / Site Populations
B	Full Width at Half Maximum of the X-ray Diffraction Peak in Radians
c	Speed of Light
d	Distance between Planes in Solid
e	Charge of an Electron
eQ	Electrical Nuclear Quadrupole Moment
eV	Electron Volt
E	Energy
E_D	Doppler-Effect Energy
E_e	Excited State Energy of the Nucleus
E_g	Ground State Energy of the Nucleus
E_K	Mean Kinetic Energy per Atom
E_R	Recoil Kinetic Energy
E_{tot}	Total Energy of the Nucleus
$E\gamma$	Energy of the Emitted Photon
f	Recoil-Free Fraction
$\hbar$	Reduced Planck Constant
h, k, l	Miller Indices
H	Magnetic Field(s)

I	Angular Momentum Quantum Number
k_B	Boltzmann Constant
L	Crystallite Size
m_I	Magnetic Quantum Number
M	Mass
Q	Capacity
T	Temperature
V	Cell Voltage
V, v	Velocity
vol.%	Volumetric Percent
θ	Incident Angle of X-ray / Diffraction Angle of X-ray
δ	Isomer Shift / Center Shift
δE	Difference between the Energy of Nuclear Transition and Energy of Emitted γ-ray Photon
Δ	Electric Quadrupole Splitting
$\mu_{negative}$	Chemical Potential of Negative Electrode
$\mu_{positive}$	Chemical Potential of Positive Electrode
λ	Wavelength
ω	Photon Angular Frequency

ACKNOWLEDGEMENTS

I would like to acknowledge first and foremost my supervisor, Dr. Mark Obrovac for giving me the chance to work in his lab. His guidance, support, and patience over the last two years helped me make this project possible. Thanks to him, I had a wonderful experience in battery research related to academia and industry. I would also like to thank the NSERC CREATE DREAMS (Dalhousie Research in Energy, Advanced Materials and Sustainability) program. Without the financial support from DREAMS, I cannot have an impressive internship in 3M Canada Company.

I would like to thank Dr. Timothy Hatchard for his help and profession in technical support. I would also like to thank Dr. Jeff Dahn for giving me the access to his laboratory equipment. His battery course helped me build the basis of my battery research. My supervisor in 3M Canada, Dr. Ranjith Divigalpitiya, helped me understand how to apply science research into industry.

I would like to thank Dr. Rich Dunlap, Dr. John Gosse, Mr. Andy George, and Ms. Patricia Scallion for their kindness to teach me new equipment. Specially, I would like to thank Dr. Rich Dunlap for helping me analyze Mössbauer spectra. I would also like to thank Ms. Giselle for all the help.

Of course, I would like to thank all current and previous mates in Obrovac lab. I obtained a bunch of help as well as friendship from you guys. In no particular order, these are: Lituo, Xiuyun, Thomas, Zack, Lauren, Douglas, Ryan, John, Justin, Zilai, Hui, Kalani, Annie, Simeng, Jackson, Bethany, Sarah, Alon, Rommy, and Alisha.

Finally, I would like to thank my parents and Mary. I cannot make it without your support and encouragement.

CHAPTER 1 INTRODUCTION

People's lives are now taken over by portable electronics: digital cameras, smartphones, tablets and laptop computers. It was estimated that there were more than 7 billion cell phones and more than 1 billion tablets used by the end of 2015 and the numbers are still growing rapidly [1]. The flourishing development of portable electronics was revolutionized by lithium ion (Li-ion) batteries since they were introduced into market by Sony in 1991 [2].

Li-ion batteries are the most widely used secondary batteries currently in the world due to their attractive features, such as high energy density (up to 685 Wh/L), high specific energy (up to 240 Wh/kg), long cycle life (greater than 1000 cycles), and a broad operation temperature range (commercially available cells may be charged at 0~45°C and discharged at -40~65°C) [2-5].

In the past two decades, Li-ion batteries have been applied to an increasingly various range of products. Now Li-ion batteries are also being used in electrified vehicles such as Tesla Model S^{TM} and BYD E6^{TM} [6, 7], which rival conventional gas powered cars in speed and acceleration. In April 2015, Tesla launched a new Li-ion battery product: Powerwall, which could collect and store solar energy for electrical supply [6].

The share of worldwide rechargeable battery market for Li-ion batteries was predicted to reach 22.5 billion dollars (accounting for 90% of total battery market) in 2020 [8]. The fast expansion of the rechargeable battery market has led to increasing

demands for better Li-ion batteries with longer cycle life and higher energy density [3]. One direction for increasing energy density is seeking alternative negative electrode materials. Currently, graphite is the prime negative electrode material for Li-ion batteries with volumetric and gravimetric capacities of 719 Ah/L and 372 mAh/g, respectively [9]. Si-based materials are potential candidates for new generation negative electrode materials with much higher theoretical volumetric and gravimetric capacities (2194 Ah/L and 3579 mAh/g, respectively) [9]. However, the volume expansion of crystalline silicon (cr-Si) is up 280% after full lithiation, which leads to poor cycling performance [9]. This has become the main barrier for Si-based materials used as Li-ion negative electrodes.

This thesis focuses on Si-based negative electrode materials for Li-ion batteries. Background information on Li-ion batteries and Si-based materials is introduced in Chapter 2, followed by experimental techniques in Chapter 3. Chapter 4 presents a chemical delithiation method to prepare bulk quantities of amorphous silicon (a-Si) from lithium silicides (Li-Si) intermetallic compounds. The a-Si thus formed was found to have layered structures. When cycled as negative electrodes in Li-ion cells, coatings containing layered a-Si were found to have improved cycling characteristics and significantly lower volume expansion during lithiation compared to that of bulk cr-Si.

Chapter 5 and 6 present applications of the chemical delithiation method introduced in Chapter 4. C-Si and Fe-Si alloys were prepared from C-Li-Si or Fe-Li-Si precursors, respectively. The as-prepared C-Si and Fe-Si electrodes were found to have enhanced cycling performance and lower volume expansion during lithiation, when cycled as

electrodes in Li-ion cells compared to that of bulk cr-Si. Finally, Chapter 7 presents conclusion of this thesis work, and suggestions for future work in this research area.

CHAPTER 2 BACKGROUND OF RECHARGEABLE LI-ION BATTERIES AND SI-BASED NEGATIVE ELECTRODES

2.1 BATTERIES

In 1799, Alessandro Volta invented the first battery, which was a Zinc-Copper battery [10]. Since then, various types of batteries have been invented and utilized in a diverse range of applications. Batteries are devices that convert chemical energy directly into electrical energy through electrochemical oxidation-reduction (redox) reactions. Basically, batteries consist of two electrodes connected by an ion conductor (electrolyte). The two electrodes have different electrochemical potentials, determined by the chemistry that occurs. The electrode with more negative potential is the negative electrode, and the one with more positive potential is the positive electrode. When connected with an external circuit, redox reactions occur in both electrodes. Electrons flow spontaneously from the negative electrode to positive electrode via the external circuit. Simultaneously, ions are transported from the negative electrode to the positive electrode via the electrolyte to maintain charge balance. This process is termed "discharge", and the resulting electrical energy can be used by devices connected in series to the external electric circuit.

Based on their capability of being recharged, batteries are classified into primary batteries (non-rechargeable batteries) and secondary batteries (rechargeable batteries). Primary batteries are not capable of being effectively recharged: they are discharged one time and discarded. There are diverse types of primary batteries, among which the very

commonly used are lithium primary batteries and alkaline batteries. Primary batteries won its market due to their high energy density, little maintenance, good shelf life, and ease of use.

Secondary batteries, by comparison, take part in reversible redox reactions. When charged, the negative electrode active material is reduced, while the positive material is oxidized. The first invented and commercialized secondary batteries were lead-acid batteries and now the dominant types are Li-ion, nickel-metal hydride and lead-acid batteries.

2.2 LITHIUM ION (LI-ION) BATTERIES

In its typical conventional format, a Li-ion battery consists of a positive electrode comprising a lithium metal oxide (*e.g.* $LiCoO_2$) or a lithium metal phosphate (*e.g.* $LiFePO_4$), a negative electrode comprising graphite, and an electrolyte consisting of a solution of a lithium salt (*e.g.* $LiPF_6$) in a mixed organic solvent (*e.g.* organic carbonates). Electrode active materials are adhered to metal foil current collectors (*e.g.* copper foil for the negative electrode or aluminum foil for the positive electrode) with a binder (*e.g.* polyvinylidene fluoride (PVDF) or sodium carboxymethyl cellulose/styrene butadiene rubber (CMC/SBR)), and a conductive diluent (*e.g.* carbon black). Within a Li-ion battery, the positive electrode and negative electrode are electrically isolated by microporous polyethylene or polypropylene membrane separators.

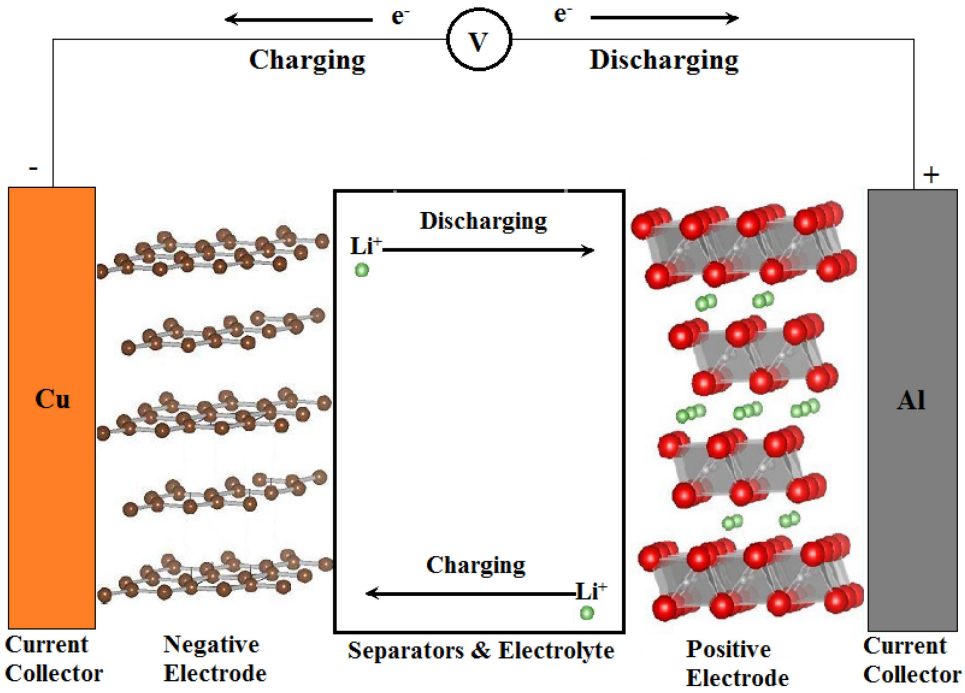

Figure 2.1 Scheme of a common Li-ion cell with $LiMO_2$ (metal oxide material) positive electrode and graphite negative electrode. Red, grey, green, and brown spheres represent oxygen, transitional metal, lithium, and carbon atoms, respectively.

Figure 2.1 shows a typical $LiMO_2$/graphite Li-ion cell scheme. The graphite and $LiMO_2$ active materials reversibly incorporate Li ions in an intercalation/deintercalation process. During charge, Li ions are deintercalated from $LiMO_2$ and intercalate into graphite, while during discharge, the process proceeds spontaneously in the opposite direction. Corresponding reactions are shown in Equation 2.1, 2.2, and 2.3. In the intercalation/ deintercalation process, no significant structural change occurs in the $LiMO_2$ or graphite hosts because graphite negative electrode materials have a layered

structure and $LiMO_2$ positive electrode materials have either a tunneled or a layered structure that can incorporate lithium ions without significant structural distortion.

$$\text{Negative Electrode:} \quad C + xLi^+ + xe^- \underset{\text{Discharge}}{\overset{\text{Charge}}{\rightleftharpoons}} Li_xC \qquad (2.1)$$

$$\text{Positive Electrode:} \quad LiMO_2 \underset{\text{Discharge}}{\overset{\text{Charge}}{\rightleftharpoons}} Li_{1-y}MO_2 + yLi^+ + ye^- \qquad (2.2)$$

$$\text{Overall:} \quad LiMO_2 + y/x\ C \underset{\text{Discharge}}{\overset{\text{Charge}}{\rightleftharpoons}} y/x\ Li_xC + Li_{1-y}MO_2 \qquad (2.3)$$

Different designs of Li-ion cells have been developed to meet market demands, including wound cylindrical, wound prismatic, stacked prismatic and pouch cells. Though different in appearance, commercial Li-ion cells have similar basic compositions.

Li-ion batteries are playing an increasingly important role in human society. However, it is still a problem to scale up common Li-ion batteries in the application for sustainable vehicles or renewable energy plants due to diverse barriers, including safety, cycle life, cost, wide temperature operational range, and materials availability [11]. The chemistry of Li-ion batteries has not changed significantly since their commercialization. It has been commonly accepted that breakthroughs in Li-ion batteries demand creative chemistries for both the electrolyte and the electrode components [2, 11].

2.3 Negative Electrode Materials

At the early development stage of secondary lithium batteries, research focused on the use of lithium metal (Li-metal) as a negative electrode material due to its high

specific capacity. Li-metal batteries showed impressive performance, but also had serious safety issues. The main safety issue was essentially attributed to the dendrite formation as a cell is cycled [12].

Safety problems with Li-metal batteries drove the industry to concentrate on other potential candidates for negative electrode materials. Now, carbonaceous materials have been the prime negative electrode materials since their introduction into the Li-ion battery industry. Other negative electrode materials include $Li_{4/3}Ti_{5/3}O_4$ (LTO) and alloy materials. Further details of carbonaceous materials, LTO and alloy negative electrode materials are discussed below.

2.3.1 Carbonaceous Negative Electrodes

Carbonaceous materials are now the most widely utilized Li-ion battery negative electrode materials. The first generation commercial Li-ion batteries used petroleum coke as negative electrode. Currently, most commercial Li-ion batteries utilize natural or synthetic graphite. Graphite has excellent features, such as good specific capacity (up to 372 mAh/g, corresponding to the formation of LiC_6), good volumetric capacity (up to 719 Ah/L), long cycle life, high coulombic efficiency (CE), small voltage hysteresis, low irreversible capacity, low average voltage, low volume expansion during lithiation, good electronic and thermal conductivity, low price and large natural abundance [4, 9].

The graphite structure is composed of multiple graphene sheets. Within one sheet, each carbon atom connects with three other carbon atoms by sp^2 C-C covalent bonds, forming a hexagonal structure. Adjacent layers connect to each other via Van der Waals

forces, and are stacked in the sequence of "ABAB" (hexagonal crystal structure, common type) or "ABCABC" (rhombohedral crystal structure). Figure 2.2 shows the simplified reversible lithiation / delithiation process of graphite in Li-ion batteries. Actually, when Li-ions are intercalated into graphite, distinct phases (stages) are formed and distinct voltage plateaus are observed [13-15]. In this process, the stacking of graphite changes but the arrangement of C-atoms within layers is maintained and only 10% volume expansion takes place.

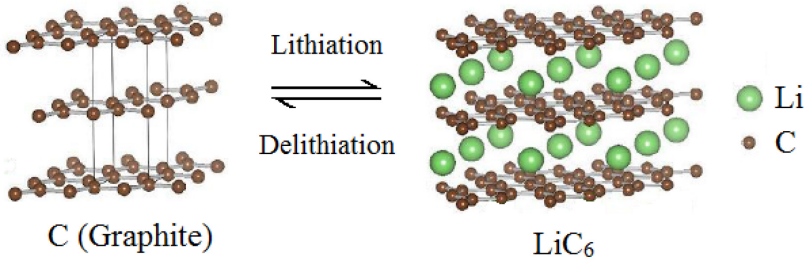

Figure 2.2 Graphite structure in fully lithiated and delithiated states. Brown spheres represent carbon atoms and green spheres represent lithium atoms.

2.3.2 $Li_{4/3}Ti_{5/3}O_4$ Negative Electrode

$Li_{4/3}Ti_{5/3}O_4$ (LTO) is another type of negative electrode material. It has the spinel structure. LTO has good cycling stability and long lifetime. However, LTO has higher potential (~1.5V) *vs.* Li compared to that of C/LiC_6, and lower capacity (175 mAh/g) compared to graphite, leading to lower energy density [16, 17].

2.3.3 Alloy Negative Electrodes

Although graphite has various excellent features as a Li-ion battery negative electrode, the developing market demands next-generation negative electrode materials

with higher energy density. Alloys are promising candidates with high energy density [18]. Figure 2.3 shows the volumetric and gravimetric capacities of a variety of Li-metal alloys calculated in the fully delithiated state compared to graphite [9]. Gravimetric capacities of alloy negative electrodes are 2~10 times higher than that of graphite. For example, the theoretical capacity of Si at room temperature is an order of magnitude higher than that of graphite. Considering volume expansion, alloy negative electrodes also offer 2~3 times higher volumetric capacities than graphite. Many ongoing researchers have focused on these alloys, including, but not limited to silicon (Si), Tin (Sn), antimony (Sb), aluminum (Al), and magnesium (Mg) based alloys [9, 17-20].

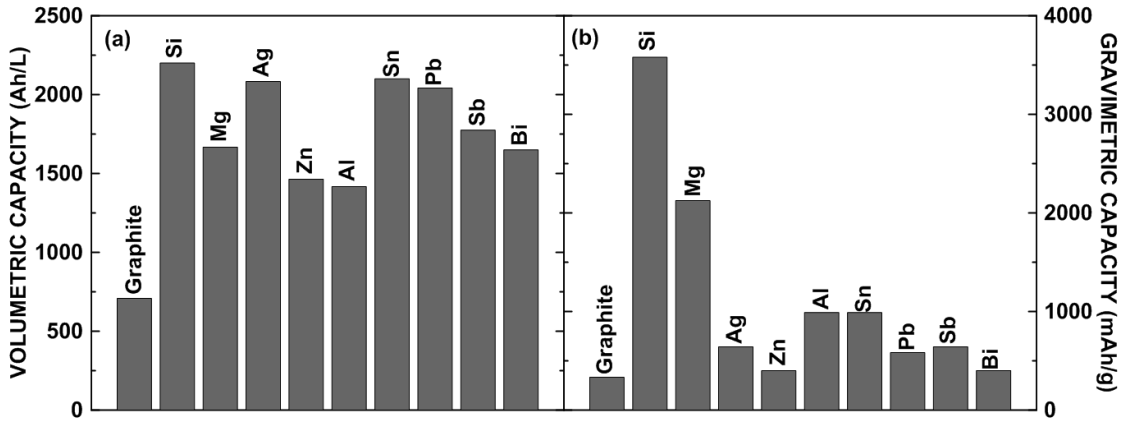

Figure 2.3 (a) Volumetric capacities calculated at the state of full lithiation and (b) gravimetric capacities of selected elements. Reproduced with permission from Reference 9.

However, the commercialization of alloys as Li-ion negative electrode materials has been hindered by their short cycle life and high irreversible capacity [17]. These are caused by large volume change alloys have during cycling (leading to disconnection of

alloy particles) [21, 22], the formation of solid-electrolyte interphase (SEI) (that constantly consume Li) [23, 24], the entrapment of Li in host alloys [22, 25] and the irreversible reaction between Li and alloy surface oxide layers [26].

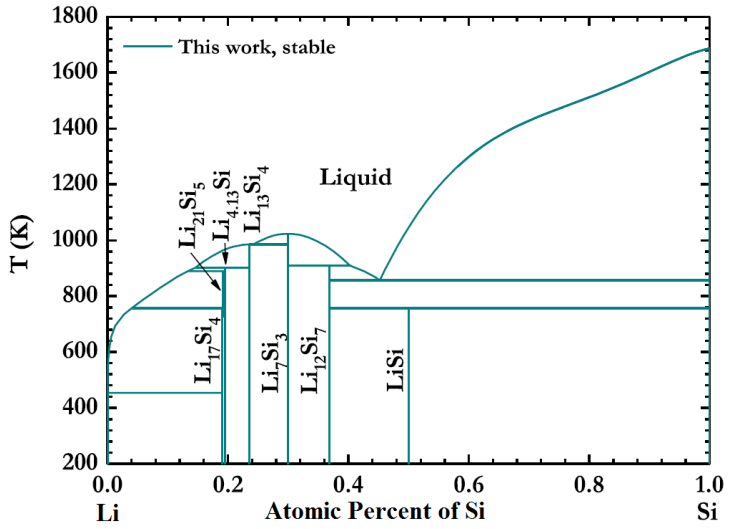

Figure 2.4 Li-Si binary phase diagram. Reprinted with permission from Reference 28.

Si-based alloys offer the highest volumetric and gravimetric capacities among all alloys shown in Figure 2.3, and have been recognized as one of the most promising negative electrode materials for Li-ion batteries [19]. Research about the electrochemical reactions of Li with Si at elevated temperatures has shown that the reactions follow the Li-Si phase diagram, with different voltage plateaus occurring for two-phase regions, corresponding to the formation of $Li_{12}Si_7$, Li_7Si_3, $Li_{13}Si_4$ and $Li_{21}Si_5$ [27]. The latest study has found that $Li_{17}Si_4$ is the Li-richest Li-Si phase, as shown in Figure 2.4 [28], corresponding to a capacity of 4055 mAh/g. Many papers state that $Li_{21}Si_5$ (4008

mAh/g) or $Li_{22}Si_5$ (4199 mAh/g) is the fully lithiated phase of Si at room temperature. However, Obrovac *et al*. showed that a $Li_{15}Si_4$ (3579 mAh/g) phase forms when the voltage (*vs*. Li/Li+) is below 50 mV at room temperature in a Li-ion half-cell with Si as the working electrode [29]. The crystalline $Li_{15}Si_4$ (cr-$Li_{15}Si_4$) phase is metastable. In the $Li_{15}Si_4$ structure, all silicon atoms are isolated and have equivalent crystallographic sites [9]. While many papers showed the initial lithiation capacity go beyond 3579 mAh/g at room temperature, one can likely attribute the extra capacity to surface reactions stemming from either lithiation of surface oxides or SEI formation [9]. It was also suspected that $Li_{15}Si_4$ can accommodate extra Li, accounting for extra capacity [30].

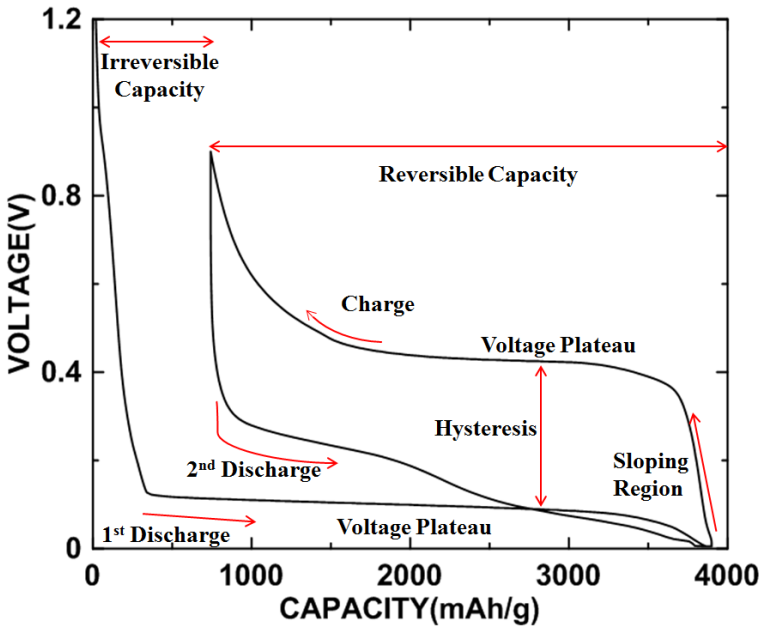

Figure 2.5 Voltage curve of a Li-(crystalline silicon) half-cell cycled at 30 °C.

Figure 2.5 and Figure 2.6 illustrate the main features of a voltage curve and a differential capacity curve of cr-Si *vs*. Li, respectively. Typically, plateaus in voltage

curves and sharp peaks in differential capacity curves are indicative of two-phase regions in the electrode phase system, while sloping regions in voltage curves usually indicate single-phase regions. In Figure 2.5, the plateau that occurs during the 1st lithiation is indicative of a two-phase region (cr-Si/amorphous Li_ySi (a-Li_ySi) phase) at ~170 mV, corresponding to peak 1 in Figure 2.6 [31]. The a-Li_ySi phase is further lithiated to a-Li_xSi phase, and then suddenly crystalize into cr-$Li_{15}Si_4$ (the fully lithiated phase of Si at room temperature) when the voltage goes below 50 mV [29]. The higher voltage plateau at ~0.45 V during delithiation in Figure 2.5 indicates another two-phase region (cr-$Li_{15}Si_4$/a-Li_zSi) [31], corresponding to peak 2 in Figure 2.6. During the 2nd lithiation, the voltage curve follows two sloping plateaus in Figure 2.5, indicative of single-phase regions, corresponding to peak 3 and 4 in Figure 2.6 [31]. The a-Li_xSi phase forms cr-$Li_{15}Si_4$ again if exposed to voltage less than 50 mV, corresponding to peak 5 in Figure 2.6. These phase transformations are illustrated in Figure 2.7.

Irreversible capacity, as labelled in Figure 2.5, is defined as the capacity difference between the first lithiation and the subsequent delithiation half-cycle. For cr-Si, its irreversible capacity is mainly caused by the formation of solid-electrolyte interphase (SEI) and electrically disconnected particles due to large volume change during lithiation and delithiation [30, 32].

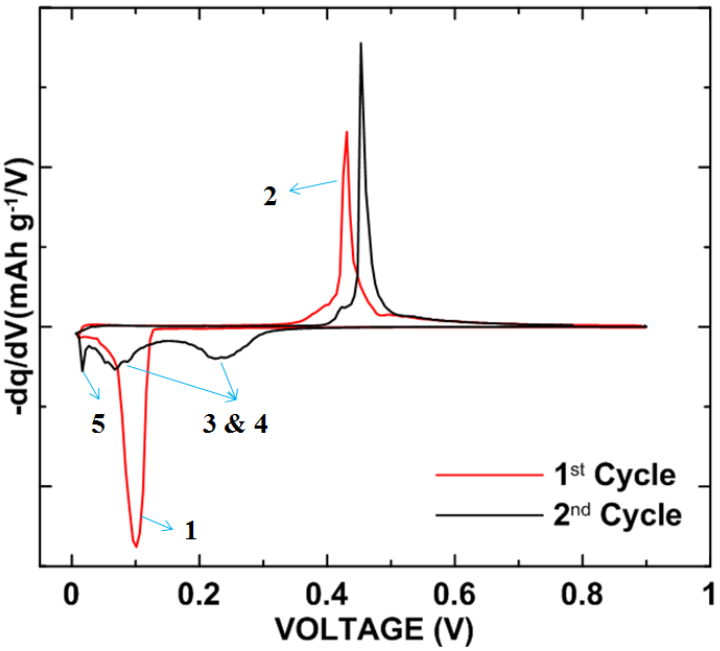

Figure 2.6 Differential capacity curve of a Li-(crystalline silicon) half-cell cycled at 30 °C.

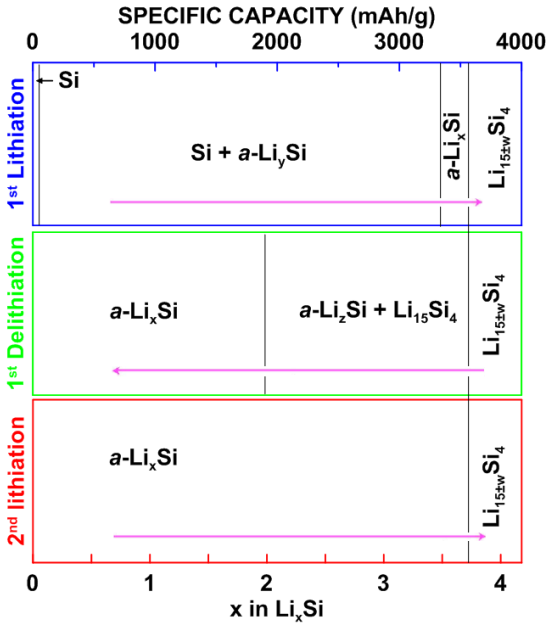

Figure 2.7 Phase transformations of Si as a Li cell negative electrode. Reproduced with permission from Reference 30.

The difference between charge and discharge voltage can be explained in terms of hysteresis. Hysteresis is a significant factor accounting for the energy loss and low battery efficiency. It is also an indicator of battery impedance. As demonstrated in Figure 2.5, cr-Si voltage curve displays large hysteresis. Actually, all known alloy voltage profiles exhibit significant hysteresis and are distinct from voltage curves obtained from intercalation materials such as graphite [9]. There is not a definitive explanation to the origin of voltage hysteresis so far. Previous studies have tried to explain the hysteresis by kinetic resistance [33], bond breaking [34], thermodynamic considerations [35], stress-potential coupling [36], and nucleation energy [37].

Although the theoretical capacity of Si is high, the use of bulk cr-Si negative electrode is hindered by its large volume expansion problem. During lithiation, the insertion of a large amount of Li ions results in the large volume expansion of silicon (up to 280% when fully lithiated) [31]. Repeated expansion and contraction during cycling can further result in structural pulverization, disconnection between particles, and disruption of the solid electrolyte interphase (SEI); ultimately leading to large irreversible capacity and poor cycling performance. Proposed solutions to mitigate the issues associated with silicon volume expansion involve utilizing nano-structural, porous or amorphous silicon materials [38-43], combining silicon with carbonaceous materials [44-46], incorporating silicon in active / inactive alloys [47], and using electrolyte additives [48, 49] and advanced binders [50].

2.3.3.1 Nano-structural, Porous and Amorphous Si

In previous studies, silicon has been prepared by metal extraction from Zintl phases [51-53]. Recently, a number of researchers have investigated the demagnesiation of Mg_2Si to form porous silicon or templated silicon-nanostructures by metathesis reaction [54-57]. This process tends to produce crystallized porous silicon. Most recently, Liang *et al*. reported the preparation of nanoporous silicon through air-oxidation demagnesiation of Mg_2Si that had improved cycling performance in Li cells over bulk silicon [58].

Amorphous silicon (a-Si) has a sloping voltage profile, making it amenable to using voltage limits as a means to adjust capacity. In previous studies, it has been shown that a-Si synthesized by chemical or physical deposition or by ball milling has improved cycling performance compared to that of bulk cr-Si [40-43]. Obrovac *et al*. showed that a-Si can be formed during the delithiation process from $Li_{15}Si_4$ in cycling at room temperature [29]. They also reported that bulk a-Si could be prepared by delithiating $Li_{12}Si_7$ with iodine in tetrahydrofuran [29]. This type of a-Si showed superior cycling characteristics compared to bulk cr-Si, but it was not pursued further due to the inconvenient preparation process.

Recent studies reported the synthesis of layered a-Si by means of exfoliation of layered $CaSi_2$ [59-61] or the extraction of alkali silicides [62, 63]. When used as negative electrodes in Li-ion cells, these silicon materials displayed superior cycling performance compared to that of bulk cr-Si [61, 62]. One possible explanation is that these materials

contain large open volume between adjacent silicon layers and, therefore, particles' expansion may be diluted by the volume between silicon layers, leading to the superior cycling performance. However, the volume expansion behavior of these layered silicon materials have not been reported. In this thesis, a convenient method is described to synthesize layered a-Si by delithiation of Li-Si intermetallic compounds. The as-prepared a-Si materials displayed improved cycling performance compared to bulk cr-Si.

2.3.3.2 Carbon-Silicon Alloys

The fabrication of carbon and silicon composites (C-Si) is another way to mitigate the problem associated with silicon volume expansion. In C-Si materials, carbon acts as a "diluent" to the volume expansion of silicon. Besides, fabrication of C-Si materials can combine the advantages of carbon (high electronic conductivity and long cycle life) and silicon (high capacity).

The most reported approach for synthesizing C-Si materials is ball milling, including mixing silicon with graphite [64-66] or other carbon precursors [67-69]. C-Si (including C coated by Si and Si coated by C) materials containing micro- and nano-porous complex structures have been produced by methods such as chemical vapor deposition (CVD) and physical vapor deposition (PVD) [70-72]. Many C-Si materials display better cycling stability than bulk cr-Si and higher capacity than pure carbon materials [64-72]. To accommodate the large volume expansion of silicon, the introduction of void spaces between the carbon coatings and silicon materials has been proposed. The "core-shell" (carbon covered on silicon) materials have been designed and tested as Li-ion battery

negative electrodes, which have good cycling performance [73, 74]. In this thesis, C-Si materials were prepared by delithiation of C-Li-Si alloys. When utilized as negative electrodes of Li-ion cells, the as-prepared C-Si alloys have superior electrochemical characteristics compared to that of bulk cr-Si.

2.3.3.3 Metal-Silicon Alloys

One way to reduce the influence of Si expansion is to combine the active material with an inactive one [46]. The principles for designing active / inactive alloys have been discussed in Reference 31. Essentially, the volume expansion of the active part is diluted by the inactive matrix during lithiation, so that the whole negative electrode can experience lower volume expansion and therefore achieve improved cycle life [75]. It has been found that the formation of $Li_{15}Si_4$ is suppressed in (active Si) / inactive alloys, leading to improved cycling performance [45]. Some active / inactive alloys containing Si have been commercialized (*e.g.* 3M L-20772 Si "V6" alloy) [75].

Among all the active / inactive systems, the iron-silicon (Fe-Si) system has been broadly studied as negative electrodes for Li-ion cells [45, 64, 76-80]. Fe-Si alloys have been made by ball milling in many previous studies [64, 76-79]. By using ball milling, researchers typically focused on how the composition and microstructure of alloys can affect their cycling performance. $FeSi_2$ and FeSi have been identified as inactive phases in ball milled Fe-Si alloys, which have been suggested to dilute the volume expansion and, as a result, improve cycling performance [76-78]. Another way to prepare Fe-Si alloy is by sputtering. Fleischauer *et al*. prepared Fe-Si films containing a-Si and Si_xFe_{1-x}

($0.5<x<1$) by sputtering as negative electrodes for Li-ion cells [80]. It was observed that the capacity of these Fe-Si electrodes was almost linearly dependent on silicon content. Fe-Si alloys have also been blended with other materials, such as graphite [79] and glass ionomer cements [81], *etc*. These alloys displayed superior cycling performance than that of bulk cr-Si [79, 81].

Other silicon alloys have also been studied as Li-ion battery negative electrodes, such as Cu-Si [82] and Ni-Si [83], *etc*. These materials exhibited improved cycling performance compared to that of bulk cr-Si [82, 83].

Anani *et al.* reported that Li ternary silicides (Li-Metal-Si) had a more favorable voltage profile and a higher reversible capacity than Li-Si binary alloys based on thermodynamic calculations [84, 85]. However, the preparation of negative electrodes for Li cells via the delithiation of Li-Metal-Si ternary compounds has never been reported.

CHAPTER 3 EXPERIMENTAL TECHNIQUES

3.1 X-RAY DIFFRACTION (XRD) SPECTROSCOPY

3.1.1 X-ray Diffraction Theory

X-radiation is a form of electromagnetic radiation, with a wavelength range between 10^{-11}~10^{-8} m (corresponding to frequencies from 3×10^{19} Hz to 3×10^{16} Hz, between ultraviolet light and gamma rays). X-radiation, also named as Röntgen radiation, was first discovered by W. C. Röntgen in 1895. X-ray diffraction (XRD) is one application of X-radiation and now XRD has become a powerful and useful technique to identify the crystalline phases present in materials.

In an XRD instrument, X-rays are most commonly generated within a sealed diode vacuum tube by the interaction of high-speed electrons with a heavy metal target (*e.g.* copper, tungsten or nickel). When a high voltage is applied, electrons will be accelerated towards the metal target with sufficient kinetic energy, so that when electrons strike an atom in the metal target, an electron will be knocked out of the core shell. After this, another electron in the atom from a higher energy level drops down immediately to fill the vacancy. This results in the emission of an X-ray photon from the atom with a sharply defined energy, equal to the difference between the initial and final energy states of the electron. Such X-rays are known as characteristic X-rays which produce spectral lines with discrete energies [86].

Copper Kα (CuKα) radiation is a common type of X-radiation used for crystallography. CuKα radiation is emitted when the impact of an incident high-speed

electron ejects an electron out of the K shell (1s shell) of a Cu atom, leaving a vacancy which is filled instantly by an electron from an outer shell. The K-shell vacancy can be filled by an electron from any of the outer shells, but is commonly filled by electrons from the L or M shell, giving rise to Kα or Kβ lines, respectively. The Kα line is stronger than the Kβ line since it is more probable that a K-shell vacancy is filled by an L electron than by an M electron [86]. An L shell contains two energy levels: L2 ($2P_{1/2}$) and L3 ($2P_{3/2}$), which gives rise to transitions with slightly different energy. The $K\alpha_1$ radiation is associated with the transition from L3 to K shell. The energy difference between these two states is 8.048 keV (corresponding to a photon with a wavelength of 1.540562 Å) [87]. The $K\alpha_2$ radiation relates to the transition from L2 to K shell with an energy difference of 8.028 keV (corresponding to a photon with a wavelength of 1.544398 Å) [87].

Many XRD experiments require near-monochromatic radiation, but the beam from an X-ray contains both the strong Kα line and the weak Kβ line. Therefore, some XRD instruments are equipped with a filter (made of materials with an atomic number 1 or 2 less than the target metal) or a monochromator. When the beam passes through a filter, the intensity of undesirable components can be reduced relative to the intensity of the Kα line [86]. A monochromator is a device transmitting a mechanically selectable narrow band of radiation chosen from a wider range of wavelength. However, the similar wavelengths of $K\alpha_1$ and $K\alpha_2$ radiation make it very difficult to be separated with a monochromator.

After being emitted from the vacuum tube, X-ray beams pass through various slits, which control the width of the incident X-ray beam. Once striking the target sample, the incident beams will be scattered and create diffracted X-ray beams. The wavelength of incident X-rays is similar in size to interatomic distance of a crystal plane. Therefore, characteristic diffraction patterns can be detected due to constructive / destructive interference of different X-ray beams scattered from an ordered arrangement of atoms. The constructive interference condition can be quantitatively described by Bragg's Law:

$$n\lambda = 2d \sin \theta. \qquad (3.1)$$

In this equation, n is an integer corresponding to the order of the reflection, λ is the wavelength of incident X-ray (1.54 Å for CuKα), d is the distance between planes, and θ is the angle between incident X-rays and diffracting planes. Equation 3.1 is derived from trigonometry, as shown in Figure 3.1.

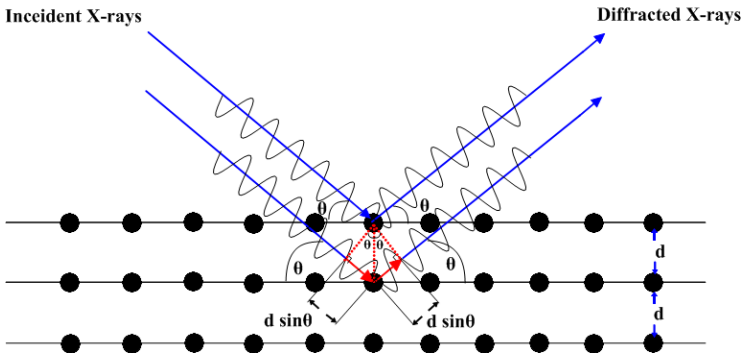

Figure 3.1 Bragg scattering from crystalline planes in a solid.

When the difference in the distance travelled by adjacent X-ray beams equals to an integer multiple of its wavelength, the photons will be in phase and the amplitudes of their waves will add to be constructive interference, increasing radiation intensity. By

contrast, if the difference between the distance travelled by adjacent X-rays equals to an odd integer multiple of half the wavelength, the photons will be out of phase, resulting in destructive interference.

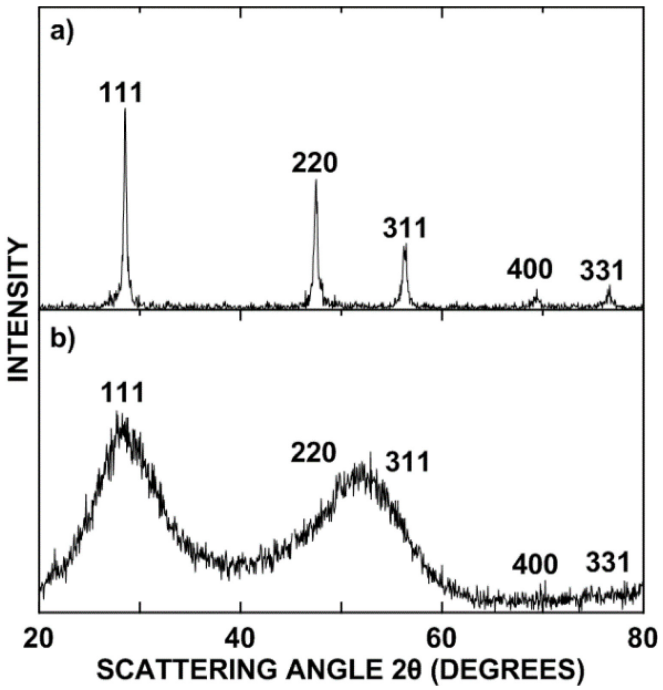

Figure 3.2 XRD patterns of (a) crystalline silicon and (b) amorphous silicon.

Crystalline solids consist of planes of atoms that can be resolved into many atomic planes with different interplanar distances. Therefore, a coordinate system (unit vectors *a*, *b*, and *c* are the edges of the unit cell) was introduced, and for cubic crystals it is an orthogonal system. With the coordinate system, any atomic plane can be distinguished by its Miller indices: *h*, *k* and *l* (three reciprocal intercepts of the plane and are reduced to the smallest integers) [86]. A Miller index will be 0 if the plane described by *hkl* does not intercept the axis of the corresponding vector. XRD data are recorded as the intensity of diffracted X-rays *vs.* the scattering angle (2θ, the angle between the incident and

diffracted X-rays). When constructive interference occurs, peaks in the scattered X-ray intensity can be observed. Depending on peak positions and Bragg's Law, the lattice interplanar distances can be calculated.

XRD patterns of highly crystalline materials contain sharp and often high intensity peaks. For example, the XRD pattern of crystalline silicon has sharp peaks with diverse heights at different angles, as shown in Figure 3.2(a). Each peak is labelled with a corresponding *hkl* plane number. However, battery materials may also be amorphous, nanostructured or disordered. Amorphous solids have structures characterized by an almost complete lack of periodicity, resulting in incoherent scattering and broad peaks corresponding to average atomic arrangements. Nanostructured or disordered materials contain ordered regions, which are on the order of 10~1000 times the wavelength of X-radiation, leading to lower scattering intensity and peak broadening. Figure 3.2(b) shows the XRD pattern of amorphous silicon containing two broad peaks instead of sharp peaks between 20~80 degrees.

If there is no inhomogeneous lattice strain, crystallite size can be estimated with the Scherrer formula (Equation 3.2):

$$L = \frac{\kappa \lambda}{B \cos\theta}, \tag{3.2}$$

where L is the average dimension of the crystallite, κ is a numerical constant (typically 0.9 as a first approximation), λ is the wavelength of incident X-rays, B is full width at half maximum of the X-ray diffraction peak in radians, and θ is the angle between incident X-rays and diffracting planes.

In this thesis, XRD analysis is used to identify samples by comparing the peak positions and intensities between the experimental XRD patterns and data from a standard database. This analysis can be performed by using software like Match! (© 2003-2011 Crystal Impact). Further structural information, such as lattice constants, site occupations, and atom positions, can be collected by fitting an experimental XRD pattern and calculating an optimized pattern based on trial crystal structures by Rietveld refinement. This process can be performed by using software like Rietica (© 1997-2007 B. A. Hunter).

3.1.2 X-ray Diffraction Sample Preparation

In the thesis, all XRD patterns were collected with a Rigaku Ultima IV diffractometer equipped with a copper target, a scintillation counter detector with a diffracted beam monochromator and a D/TeX Ultra linear detector with K-beta filter. The scintillation detector with a diffracted beam monochromator was used to collect XRD data of all powder samples. The X-ray generator accelerating voltage was 45 kV and the filament current was set at 40 mA.

For XRD measurements, air stable powders were packed on a Si crystal within a stainless steel plate (shown in Figure 3.3(a)) and pressed into uniform surface with a glass slide. The Si crystal helps to avoid Bragg diffraction and gives near-zero background. Air-sensitive powders were packed in the same way into a custom designed gas tight sample holder with an aluminized Mylar^{TM} window, as shown in Figure 3.3(b). The window material never satisfied the Bragg condition and thus does not contribute to

the XRD pattern. The gas tight holder can be sealed in an inert atmosphere (*e.g.* an argon filled glovebox) to avoid contact with air. XRD data for all samples were collected at a scattering angle (2θ) range of 20 to 80 degrees (or 20 to 60 degrees) with a single step of 0.05 degree and a 3 second (or 6 second) dwell time.

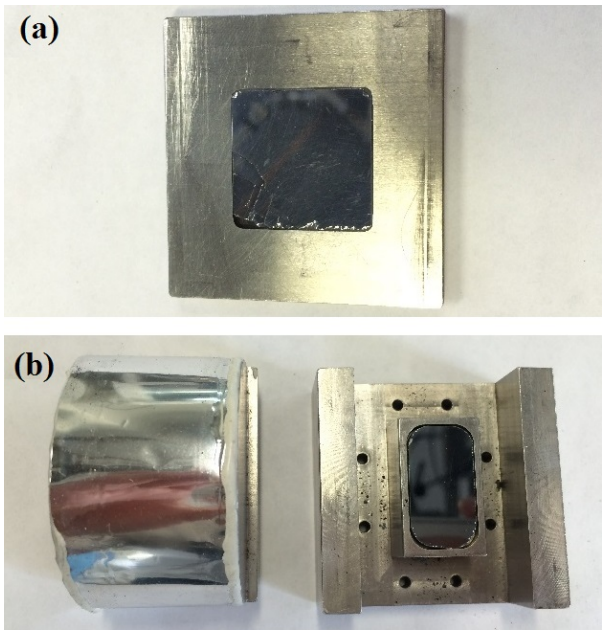

Figure 3.3 (a) The XRD holder for air-stable samples with a zero background silicon wafer and (b) the gas tight XRD holder (DPM Solutions, Hebbville NS) for air-sensitive samples with a zero background silicon wafer.

3.2 Scanning Electron Microscopy

Scanning electron microscopy is a powerful technique for investigating surface topographical information of materials. The resolution of scanning electron microscope (SEM) images can reach nm level and SEMs can operate at magnifications that are easily adjusted from about 10× ~ 300,000× [88].

During operation of the SEM, electrons are produced by a thermionic field in an electron gun and accelerated by applying a potential (0.1~50 keV). High-speed electrons travel through a condenser lens and an electromagnetic field, which raster the electron beam over the specimen surface, where a number of interactions occur. All these processes maintained at high vacuum environment. The electron beam can interact with the coulomb field of both the specimen atoms' nucleus and electrons, causing the emission of secondary electrons, back scattered electrons and X-rays.

When a beam electron interacts with the specimen atom electron, inelastic events occur, resulting in a transfer of energy to the atom and an ejection of an electron from this atom as a secondary electron (SE). SEs are less than 50 eV in energy, by convention. If the vacancy due to the ejection of a SE is filled by an outer shell electron, an X-ray of that energy transition is produced. Most SEs fall in an energy range between 2~5 eV.

When an electron beam interacts with the specimen atom nucleus, elastic events occur, resulting in a change in direction of the beam electron without a significant change in its energy (<1eV). If the elastically scattered beam electron is deflected back out of the specimen surface, the electron is termed as a backscattered electron (BSE). BSEs can have an energy range from 50 eV to nearly the incident beam energy. Most BSEs retain >50% of the incident beam energy. The fraction of incident electrons transforming into BSEs strongly depends on the atomic number of the scattering atom, which directly affects the image brightness. Therefore, BSEs can be used to detect contrast between surfaces with different chemical compositions.

The emitted electrons/X-rays can be collected by detectors, and the output can be used to modulate the brightness of a cathode ray tube (CRT). The x-y inputs of CRT are in synchronism with the x-y voltages rastering the electron beam. In this way, an image is produced on the CRT screen and every point that the beam strikes on the specimen is mapped directly onto a corresponding point on the screen.

In this thesis work, particle size and morphology of samples were studied with a Phenom G2-pro Scanning Electron Microscope (Nanoscience, Arizona) and a Hitachi S-4700 FEG Scanning Electron Microscope.

3.3 MÖSSBAUER SPECTROSCOPY

The phenomenon of the emission or absorption of a γ-ray photon without loss of energy due to recoil of the nucleus and without thermal broadening is known as the Mössbauer effect [89]. The Mössbauer effect has been detected in a total of 88 γ-ray emissions from 72 isotopes of 42 different elements [89]. Mössbauer effect spectroscopy was devised by Rudolf Mössbauer in 1958 [90]. By far the most commonly used isotope in Mössbauer spectroscopy studies is ^{57}Fe because it has a natural abundance of ~2% in bulk Fe and γ-ray photons can be produced using a ^{57}Co radioactive source. Now Mössbauer spectroscopy has become a versatile technique applied in many fields like physics, biology, metallurgy and chemistry. It can provide precise information about the chemical, structural and magnetic properties of materials [91].

If the energy of an isolated atom in the gas phase is defined as:

$$E = E_e - E_g, \tag{3.3}$$

where E_e and E_g are the excited and ground state energies of the nucleus, respectively, then the total energy of the nucleus of mass M moving at initial velocity V_x will be

$$E_{tot} = E + \frac{1}{2}MV_x^2. \tag{3.4}$$

If a γ-ray photon is emitted from the nucleus the total energy is:

$$E_{tot} = E_\gamma + \frac{1}{2}M(V_x + v)^2, \tag{3.5}$$

where $E\gamma$ is the energy of the emitted photon and v is the change in velocity (can be positive or negative) of the nucleus. The difference between the energy of the nuclear transition and energy of the emitted γ-ray photon is:

$$\delta E = E - E_\gamma = \frac{1}{2}MV_x v + \frac{1}{2}Mv^2 = E_D + E_R, \tag{3.6}$$

where E_D and E_R are the Doppler-effect energy and the recoil kinetic energy, respectively. The mean kinetic energy per atom in a gas with random thermal motion is:

$$E_K = \frac{1}{2}M\overline{V}_x^2 \cong \frac{1}{2}k_B T. \tag{3.7}$$

The Doppler shift in the γ-ray energy originates from random thermal motion and the recoil of the atom. The mean Doppler-effect energy $\overline{E_D}$ can be written in terms of the mean recoil kinetic energy:

$$\overline{E_D} = 2\sqrt{\overline{E_K}E_R}\ . \tag{3.8}$$

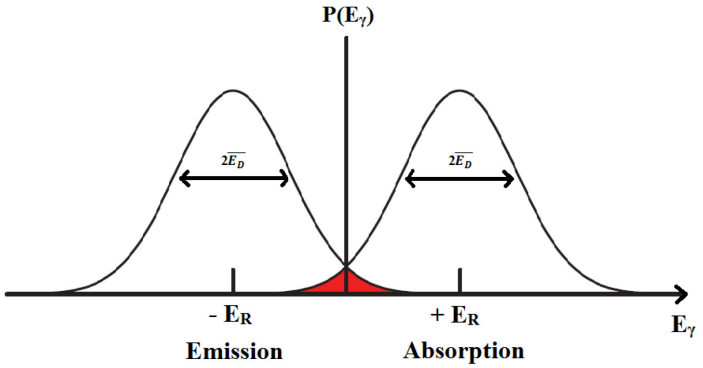

Figure 3.4 Distributions of energies produced from a recoiling nuclear emitter and absorber. The shaded area is the resonance overlap region. Reproduced with permission from Reference 92.

The energy distribution for emission and absorption of a γ-ray photon is illustrated in Figure 3.4. The shaded overlap area is called the recoil free fraction. In order to produce a resonant signal, the two energies need to overlap as shown in the shaded area. Generally, the fraction of the overlap region is extremely small, making it an impractical technique [91].

E_R can be expressed as:

$$E_R = \frac{E_\gamma^2}{2Mc^2}, \tag{3.9}$$

where c is the speed of light. Rudolf Mössbauer discovered that a significant fraction of emission and absorption events will be recoil-free if the atoms are bound in a solid, instead of free atoms. In a solid, the recoil energy of a free nuclei (10^{-4} ~ 10^{-1} eV) is much less than the bond energy (1~10 eV). Therefore, the emitting atom cannot recoil freely; but instead, the whole crystal recoils. This mean the effective mass (mass of the whole crystal) is much larger than the recoil energy. In other words, E_R approaches zero.

The mean Doppler-effect energy ($\overline{E_D}$) also approaches zero according to Equation 2.9. When recoil energy is transferred to the crystal (*i.e.* does not lead to a change in the crystal vibrational energy), the emission and absorption peaks in Figure 3.4 will shift to zero and the overlap between them grows larger. The probability of this happening is called the recoil-free fraction, *f*, and is described by Equation 3.10:

$$f = 1 - \frac{E_R}{\hbar\omega}, \tag{3.10}$$

where $\hbar$ is the reduced Planck constant and ω is the photon angular frequency.

In the case of ^{57}Fe Mössbauer spectroscopy, the excitation of Fe nuclei originates from metastable ^{57}Co (half-life of 270 days) as shown in Figure 3.5. ^{57}Co decays to the unstable second excited state of ^{57}Fe by electron capture. With a probability of 85%, the second excited state of ^{57}Fe decays to the first excited state, which has a half-life of ~100 ns. A short time later, ^{57}Fe decays to the ground state. The transition from 3/2 to 1/2 is important for the Mössbauer effect.

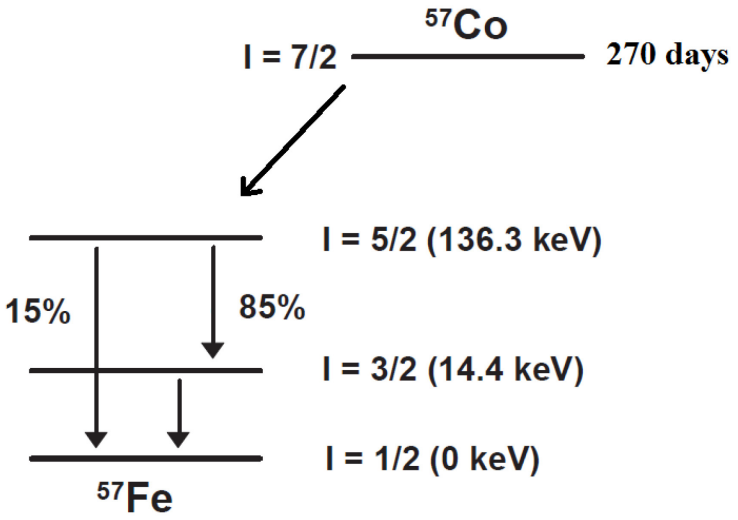

Figure 3.5 ^{57}Fe decay scheme. Reproduced with permission from Reference 92.

The nuclear transition energy can be slightly changed by hyperfine interactions between the nucleus and its environment. Such miniscule variations of the probing γ-ray energy are changed by the use of the Doppler Effect. This can be achieved by oscillating a radioactive source with a velocity of few mm/s [89, 91]. When the modulated γ-ray energy matches exactly the energy of an absorbing nuclear transition, the γ-ray can be resonantly absorbed and a peak can be observed.

There are three main types of hyperfine interactions: isomer shift (center shift), quadrupole splitting and magnetic splitting.

Isomer shift (δ), also named as center shift, originates from the changes of s-electrons density in the nucleus and the non-zero volume of the nucleus. Changing the total electronic charge over the nucleus volume alters the coulombic potential at the nucleus, leading to a monopole interaction. Any difference in the s-electrons environment between the absorber and source produces a shift in the resonance transition energy. The shift cannot be measured directly. Therefore, it is quoted relative to a known absorber. In the case of ^{57}Fe, Mössbauer spectra are often quoted relative to α-Fe at room temperature [91]. Isomer shift values give information about the oxidation states, spin states, and bonding properties.

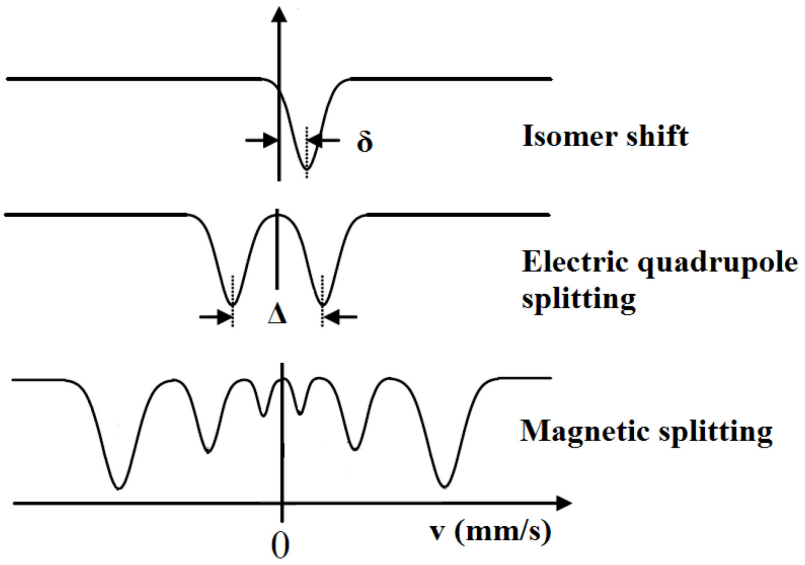

Figure 3.6 Scheme of isomer shift (center shift), electric quadrupole splitting and magnetic splitting.

Electric quadrupole splitting (Δ) arises through the quadrupole interaction between the electrical nuclear quadrupole moment *eQ* (for a total angular momentum quantum number greater than ½) and an inhomogeneous electrical field (electric field gradient, EFG). In the case of the ^{57}Fe, the ground state has $I = 1/2$ and the excited Mössbauer-state has $I = 3/2$. The excited state is split into two substates: $m_I = \pm 1/2$ and $m_I = \pm 3/2$ [91]. The information derived from the quadrupole splitting refers to molecular symmetry, oxidation state, and spin state.

Magnetic splitting, also named Zeeman splitting, occurs through the interaction between the nuclear dipole moment and the non-zero magnetic field. Six lines are obtained for ^{57}Fe in its Mössbauer spectrum. Figure 3.6 shows the scheme of isomer shift (center shift), electric quadrupole splitting and magnetic splitting.

In this thesis, all ^{57}Fe Mössbauer effect measurements were performed with a See Co. constant acceleration spectrometer equipped with an Rh^{57}Co source at room temperature. The velocity scale was calibrated relative to α-Fe at room temperature. Mössbauer spectra was analyzed with the Recoil software package (© 1998 Ken Largarec and Denis G. Rancourt).

3.4 ELECTROCHEMICAL TECHNIQUES

In a two-electrode metal-ion cell, there is a positive electrode and a negative electrode separated by electron-insulating separators drenched in an ion-conductive electrolyte. The cell is connected with an external circuit in operation. The negative electrode is where oxidation occurs during discharge and the positive electrode is where reduction occurs during discharge. To determine the cell voltage (V) of a Li-ion cell, Equation 3.11 is used:

$$V = \frac{-(\mu_{positive} - \mu_{negative})}{ne}, \qquad (3.11)$$

where V is the cell voltage measured in volts, $\mu_{positive}$ and $\mu_{negative}$ are the chemical potentials of positive and negative electrodes, respectively, n is the number of active electrons per Li ion (n = 1 for lithium) and e is the charge of an electron. In this thesis work, all electrochemical measurements were conducted with half-cells, in which the studied materials performed as working electrodes and are cycled against a lithium metal foil (reference/counter electrode).

Capacity (Q) is defined as the total amount of electrical charge involved in electrochemical reactions in units of coulombs or, more commonly used in this thesis,

milliampere-hours (mAh). The gravimetric capacity of a material is determined by the capacity per unit mass of the active material, in units of mAh/g among the battery community. The volumetric capacity is measured in units of mAh/cm^3 or Ah/L. The term "C-rate" indicates the cycling current required to charge or discharges a cell in one hour, which can be calculated from using the theoretical capacity of the studied material in mAh. For instance, a C/5 rate corresponds to the current required to charge or discharge a cell in 5 hours.

Cycling data of cells can be displayed as a voltage-capacity curve (or voltage curve), capacity-cycle number curve, a dQ/dV-voltage curve (or differential capacity curve) and a voltage-time curve.

3.4.1 Electrode Fabrication

In this study, composite electrodes comprising powdered materials were utilized. Active powder materials (amorphous Si, C-Si, Fe-Si, *etc*.) were prepared in different ways and detailed procedures are discussed in Chapters 4, 5 and 6. Electrodes consisted of powder active materials, binder (polyimide (PI) HD MicroSystems PI 2555) and conductive diluent (Super-P, carbon black, Erachem Europe) in a volume ratio of 67.5:19.5:18. These components were loaded in air and mixed in a binder soluble solvent (N-methyl-2-pyrrolidone, Sigma Aldrich, anhydrous 99.5%) using a planetary ball mill (Retsch PM200) with four 7/16" tungsten carbide (WC) balls for 1 hour at 100 rpm, resulting in the formation of homogeneous slurries. The resulting slurries were spread on copper foil (Furukawa Electric, Japan) with a 0.004" notch bar to form a coating layer of

even thickness. After this, the coated foil was dried in air or under vacuum at 120 °C for 1 hour. All disk-like working electrodes (diameter 13 mm) used in coin-type cells were punched from the coated foils with an electrode punch. This thesis involves different types of active materials and each material may require different formulas or treatments. Therefore, further details regarding preparation will be introduced in following chapters.

3.4.2 Half-cells

Coin cells are commonly used hardware for testing battery materials [93, 94]. In this thesis, 2325 coin-type cells were assembled in an argon filled glove box to evaluate the performance of electrode materials in Li half-cells [95]. Figure 3.7 illustrates the general structure of a 2325 coin-type cell used in this study. Li disks were punched from a thick Li foil (99.9%, Sigma Aldrich) as reference/counter electrodes (not shown in Figure 3.7). A stainless steel spacer and a stainless steel spring were used to provide proper pressure on electrodes and ensure good electrical contact. Two layers of Celgard 2300 separators and one working electrode were assembled in each coin cell. A polyethylene gasket performed as an insulator between the top and bottom casings, preventing electrical contact and cell short. The electrolyte was 1 M $LiPF_6$ (BASF, 98%) dissolved in 30:60:10 (by volume) ethylene carbonate (EC):diethyl carbonate (DEC):monofluoroethylene carbonate (FEC) (all from Novolyte Technologies).

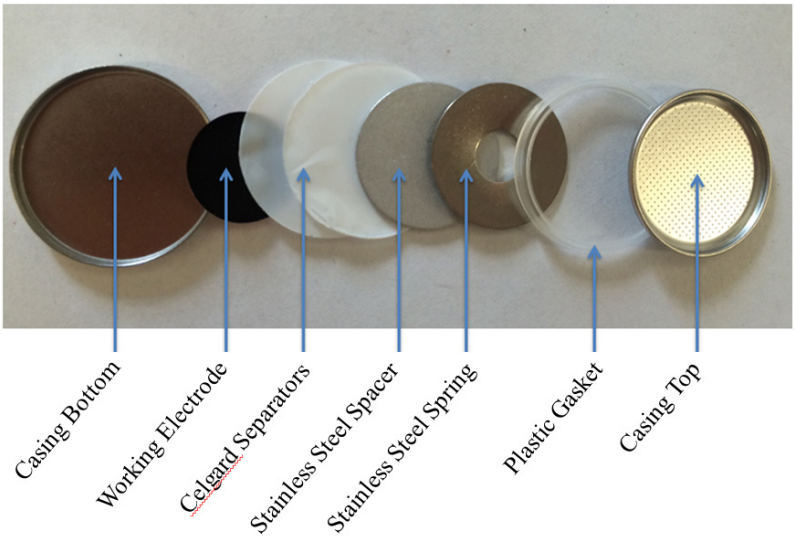

Figure 3.7 Schematic structure of the 2325 coin-type cell used in this thesis work. Note that the stainless steel spacer is coated with Li metal foil (not shown) as the reference/counter electrode of half-cells.

3.4.3 Galvanostatic Cycling

The electrochemical performance of coin cells was measured with a Maccor Series 4000 Automated Test System (Maccor Inc., Tulsa OK) with a current accuracy of 0.05% of full scale current. This system has the capability to perform many electrochemical techniques, such as galvanic cycling, cyclic voltammetry, constant power cycling, *etc.*, and has the ability to be programmed to combine multiple techniques. With such techniques, one can measure the thermodynamics processes behind cycling, interpret phase changes and diffusion, compare the behavior of different electrode materials and determine their commercial eligibility.

When cycling cells, a constant current, constant voltage (CCCV) method was used to mimic the cycling protocol of commercial Li-ion cells. In this procedure, half-cells are

first discharged (lithiation of the working electrode) at a constant current (CC). During this process, the cell potential decreased until it reached a lower potential limit. Then half-cells were discharged at the lower potential (constant voltage, CV) until the current decreases to a lower current limit. Following the CV step, cells were charged (delithiation of the working electrode) at the same constant current (CC) to a desired upper potential limit. These form a full cycle.

Cells discussed in Chapter 4, 5 and 6 were cycled at 30.0 ± 0.1 °C between 0.005 V - 0.9 V at a C/20 rate and trickle discharged to C/40 rate for the 1st cycle and at a C/5 rate and trickle discharged to a C/20 rate for the following cycles. All coin cells had a rest period of 15 minute at open circuit at the end of each half-cycle.

3.5 GAS PYCNOMETRY

Gas pycnometry is one of the most reliable methods to obtain accurate, absolute, skeletal, and apparent volume of solid materials based on the Archimedes principle of displacement of an inert gas medium, such as nitrogen, argon, or helium. This method is non-destructive so that the tested samples can be retrieved.

For gas pycnometry, a dry solid sample of known mass (m_S) is placed in a sample chamber (known volume V_S). The sample chamber is connected with a reference chamber (known volume V_R) through a valve. First, the sample chamber is sealed and filled with an inert gas up to a certain pressure. The pressure decreases and reaches equilibrium (initial pressure (P_I)) at a certain time as a result of gas penetration into the pore structure of the sample. Then the valve connecting the two chambers is opened, and

the inert gas flows from the sample chamber to the reference chamber. When equilibrium is reached again, the final pressure is also recorded (P_F). The solid volume of the sample V_{Solid} can be calculated accord to Equation 3.12 below:

$$V_{Solid} = V_S - \left(\frac{P_F}{P_I - P_F}\right) \times V_R \tag{3.12}$$

Then the density of the sample can be calculated by Equation 3.13:

$$\rho = \frac{m_S}{V_{Solid}} \tag{3.13}$$

The gas pycnometer must be calibrated regularly with certified calibration spheres to keep the accuracy of measurements. Significantly wrong results are obtained if the calibration is not done regularly. It is noticeable that the gas pycnometry measurements are performed under isothermal conditions.

In this thesis work, densities of all samples were measured with a helium pycnometer (AccuPyc II 1340, Micrometritics).

CHAPTER 4 LAYERED AMORPHOUS SILICON PREPARED BY DELITHIATION

4.1 INTRODUCTION

As discussed in Chapter 2, silicon has high theoretical capacity (2194 Ah/L, 3579 mA h/g, corresponding to the formation of $Li_{15}Si_4$) [29]. However, the commercialization of crystalline silicon (cr-Si) as negative electrodes for Li-ion batteries is hindered by its large volume expansion (up to 280% after full lithiation) [31]. To mitigate this issue, researchers have tried utilizing nano-structural, porous or amorphous silicon materials.

Previous studies have reported diverse methods to prepare nano-structural, porous or amorphous silicon as negative electrodes for Li-ion batteries. Obrovac *et al*. prepared bulk amorphous silicon (a-Si) by delithiating $Li_{12}Si_7$ with iodine in tetrahydrofuran [29]. Recent studies have investigated the demagnesiation of Mg_2Si to form crystalline porous Si or templated Si-nanostructures [54-57]. Most recently, the synthesis of layered a-Si has been reported by means of exfoliation of layered $CaSi_2$ [59-61] or the demetallization of alkali silicides with alcohols or anhydrous ammonia [62, 63]. When used as negative electrodes in Li-ion cells, these materials showed better cycling performance compared to that of bulk cr-Si [61, 62].

In this chapter, lithium silicide intermetallic compounds (Li-Si) were first synthesized. Bulk quantities of a-Si were prepared by the delithiation of Li-Si with alcohols. This resulted in the formation layered a-Si in high yield. The layered a-Si was

found to have superior cycling performance and surprisingly low volume expansion compared to bulk cr-Si.

Besides delithiation with alcohols, other methods were also studied to prepare silicon. Relevant procedures and results are also reported in this chapter.

4.2 EXPERIMENTAL

Synthesis of Layered Amorphous Si

The Li-Si intermetallic compounds $Li_{12}Si_7$, Li_7Si_3, $Li_{13}Si_4$ or $Li_{22}Si_5$ were first synthesized by arc melting ~1.5 g of a stoichiometric ratio of Li (99.90% Li ribbon, Sigma) and Si (98.40% Si lump, Alfa Aesar) with a 7% excess of Li (to offset Li loss from vaporization) under an argon flow. After cooling, the resulting ingots were then ground into powder with a mortar and pestle in an argon-filled glove box.

Powder of the Li-Si intermetallic compounds was then delithiated by first adding ~1.0 g of the Li-Si powder into a 3-neck flask with a magnetic stirrer in an Ar-filled glovebox. The flask was then placed in fumehood and an Ar-flow was introduced and exhausted via an oil bubbler. Approximately 120 mL of either ethanol (99.89%, containing 0.10% H_2O, Commercial Alcohols) or isopropanol (99.50%, containing 0.20% H_2O, Fisher Scientific) (hereafter termed delithiants) was then added quickly to the flask and the mixture was then stirred continuously. When isopropanol was used as the delithiant, the reaction was extremely slow at room temperature. Therefore a water-cooled condenser was affixed to the top of the flask and the delithiation reactions with isopropanol were carried out under refluxing conditions at 80 °C for 3 hours. When

ethanol was used as the delithiant, the reaction proceeded sufficiently fast at room temperature and it reached completion after reacting overnight. No condenser was required when an ethanol delithiant was used. After the delithiation reactions, the product was transferred into a Büchner funnel (using 44.25 mm filter paper, Whatman) and was washed with distilled water for 3 times, HCl (1 mole/L, prepared from 37% HCl, Aldrich) for 3 times and then distilled water again until the pH of the washing water was ~7. The black, water-stable product was then heated in tube furnace at 120 °C for 3 hours under an argon flow. Some ethanol delithiated a-Si from $Li_{12}Si_7$ was further heated at 550 °C or 600 °C for 2 hours under an Ar-flow to investigate the influence of heat-treatment. Hereafter, the method described in this paragraph (reaction of Li-Si with alcohols, washing with Büchner funnel and heating) is termed Method 1.

Other methods were also studied. $Li_{12}Si_7$ (~1.0 g) were loaded in a 3-neck flask using the same method as described in the last paragraph. The 3-neck flash was placed in fumehood and an Ar-flow was introduced and exhausted through the flask. Approximately 120 mL of hexane (>98.50%, Fisher Scientific), isopropanol (99.50%, containing 0.20% H_2O, Fisher Scientific) or dimethyl carbonate (DMC) (>99%, Fisher Scientific) was then added quickly to the flask and the mixture was then stirred continuously. A water-cooled condenser was affixed to the top of the flask and the delithiation reactions were carried out under refluxing conditions at 80 °C for 3 hours. After the delithiation reaction, the mixture was isolated via centrifuging, instead of washing with a Büchner funnel, and the supernatant was abandoned. The solid phase was

washed repeatedly with the corresponding solvent used in delithiation reactions via centrifuging. The solid phase of the product was then heated in tube furnace at 350 °C for 3 hours under an Ar-flow. Hereafter, the method described in this paragraph (reaction of Li-Si with hexane/isopropanol/DMC, centrifuging and heating) is termed Method 2. Method 2 did not yield good silicon products. Therefore, the as-formed products were not cycled as electrodes.

Characterization by Microscopy and X-ray Diffraction

XRD patterns were collected with a Rigaku Ultima IV diffractometer equipped with a copper target, a dual position graphite diffracted beam mono-chromator and a scintillation counter detector. Particle size and morphology of samples were studied with a Phenom G2-pro Scanning Electron Microscope (Nanoscience, Arizona) and a Hitachi S-4700 FEG Scanning Electron Microscope. Sample densities were measured with a helium pycnometer (AccuPyc II 1340, Micrometritics).

Electrochemical Characterization

Electrode slurries were prepared by mixing a-Si (prepared with Method 1) or cr-Si (325 mesh, Aldrich), optionally graphite (SFG6L, Timcal, average size of 3 μm), carbon black (Super-P, Erachem Europe) and polyimide (PI, PI-2555, HD Microsystems) in N-methyl pyrrolidinone (NMP, 99.50%, Sigma). Electrode coatings consisted of either a Si/carbon black/PI ratio of 67.5/19.3/13.2 by weight (62.5/18/19.5 by volume) formulation or a Si/graphite/carbon black/PI ratio of 43.3/24.2/19.3/13.2 by weight (40/22.5/18/19.5 by volume) formulation. The slurries were mixed for 1 hour using a

planetary ball mill (Retsch PM 200) with four 7/16" WC balls at 100 rpm. The resulting slurries were coated on copper foil (Furukawa Electric, Japan) with a 0.004 inch coating bar and dried at 120 °C in air for 1 hour. Some electrodes were calendered using an adjustable gap calender with 6" diameter rolls (DPM Solutions, Nova Scotia, Canada) to achieve a porosity of 20~25%, so that good electrode kinetics could be maintained [45]. Electrode disks (d = 13 mm) were punched from the coated foil and then heated in a tube furnace for 3 hours at 300 °C under argon flow in order to cure the PI binder.

Electrodes were transferred into an argon-filled glove box and assembled in 2325 coin-type cells with a lithium foil reference/ counter electrode and an electrolyte composed of 1M $LiPF_6$ (BASF) in a solution of monofluoroethylene carbonate (FEC), ethylene carbonate (EC) and diethyl carbonate (DEC) (volume ratio 1:3:6, all from Novolyte Technologies). Two layers of Celgard 2300 separators, a stainless steel spacer and a stainless steel spring were used in each cell. All cells were cycled at 30.0 ± 0.1 °C with a Maccor Series 4000 Automated Test System between 5 mV and 900 mV at a C/20 rate and trickle discharged (lithiation) to C/40 rate for the first cycle; and at a C/5 rate and trickle discharged to a C/20 rate for following cycles. Cells had a rest period of 15 min at open circuit at the end of each half-cycle. C-rate was calculated based on 3579 mAh/g for Si and 372 mAh/g for graphite. Electrode thicknesses were measured in an argon-filled glove box to within ±1 μm with a Mitutoyo 293-340 precision micrometer before assembling cells and after full lithiation (C/20 constant current, C/40 trickle, 5 mV limit).

4.3 Results and Discussion

Method 1

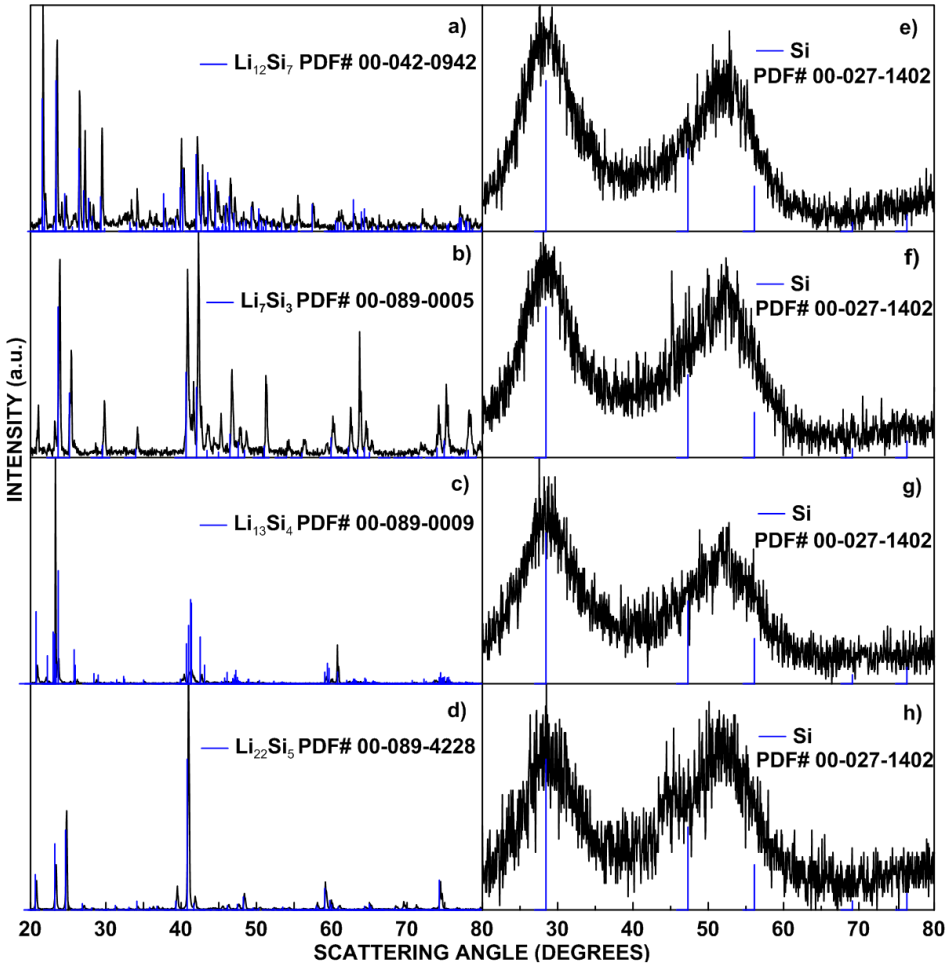

Figure 4.1 XRD patterns of synthesized $Li_{12}Si_7$, Li_7Si_3, $Li_{13}Si_4$, and $Li_{22}Si_5$ (a-d, respectively). XRD patterns of a-Si prepared from $Li_{12}Si_7$, Li_7Si_3, $Li_{13}Si_4$, and $Li_{22}Si_5$ with ethanol are shown in (e-h), respectively.

Figure 4.1(a-d) show the XRD patterns of the $Li_{12}Si_7$, Li_7Si_3, $Li_{13}Si_4$, and $Li_{22}Si_5$ phases as synthesized by arc melting. All of these phases were nearly phase pure as made with only slight impurity peaks, arising from other Li-Si phases.

Bulk quantities of air / water stable a-Si powders were prepared by delithiation of $Li_{12}Si_7$, Li_7Si_3, $Li_{13}Si_4$, and $Li_{22}Si_5$ by reaction with either ethanol or isopropanol in an Ar atmosphere, presumably according to the reaction below:

$$LiSi_x\ (s) + R\text{-}OH\ (l) \rightarrow R\text{-}OLi\ (s) + \tfrac{1}{2}\ H_2\ (g) + xSi\ (s). \qquad (4.1)$$

The alkoxide products were insoluble in their parent alcohols, and were subsequently removed by rinsing the product with HCl and water. The resulting delithiated Si was produced in yields of about 70% and 60% using ethanol and isopropanol delithiants, respectively.

Figure 4.1(e-h) show the XRD patterns of delithiated Si prepared from $Li_{12}Si_7$, Li_7Si_3, $Li_{13}Si_4$, and $Li_{22}Si_5$, respectively, with ethanol as the delithiant. All XRD patterns are characteristic of a-Si, except that formed from the delithiation of $Li_{22}Si_5$, which shows a minor and broad impurity peak near 44°. Amorphous Si was also obtained when $Li_{12}Si_7$ was delithiated using isopropanol. However, because of the ease of use of ethanol as a delithiant and the higher yield of a-Si produced, ethanol was chosen as the main delithiant used in this study. Except $Li_{22}Si_5$, all of the Li-Si intermetallic compounds reacted slowly with ethanol, resulting in little temperature change and slow bubbling. In the case of $Li_{22}Si_5$, a vigorous reaction occurred, causing the ethanol to boil.

Figure 4.2(a-d) show SEM images of the ethanol delithiated a-Si from $Li_{12}Si_7$, Li_7Si_3, $Li_{13}Si_4$, and $Li_{22}Si_5$, respectively. Figure 4.3(a-b) show two SEM images of the ethanol delithiated a-Si from $Li_{12}Si_7$. All samples had overall particle sizes ranging from about 5 μm to 40 μm. The sample particles have surprizing features in their

microstructure. In particular, a-Si formed from ethanol delithiation of $Li_{12}Si_7$, Li_7Si_3, and $Li_{13}Si_4$ show features characteristic of a layered microstructure.

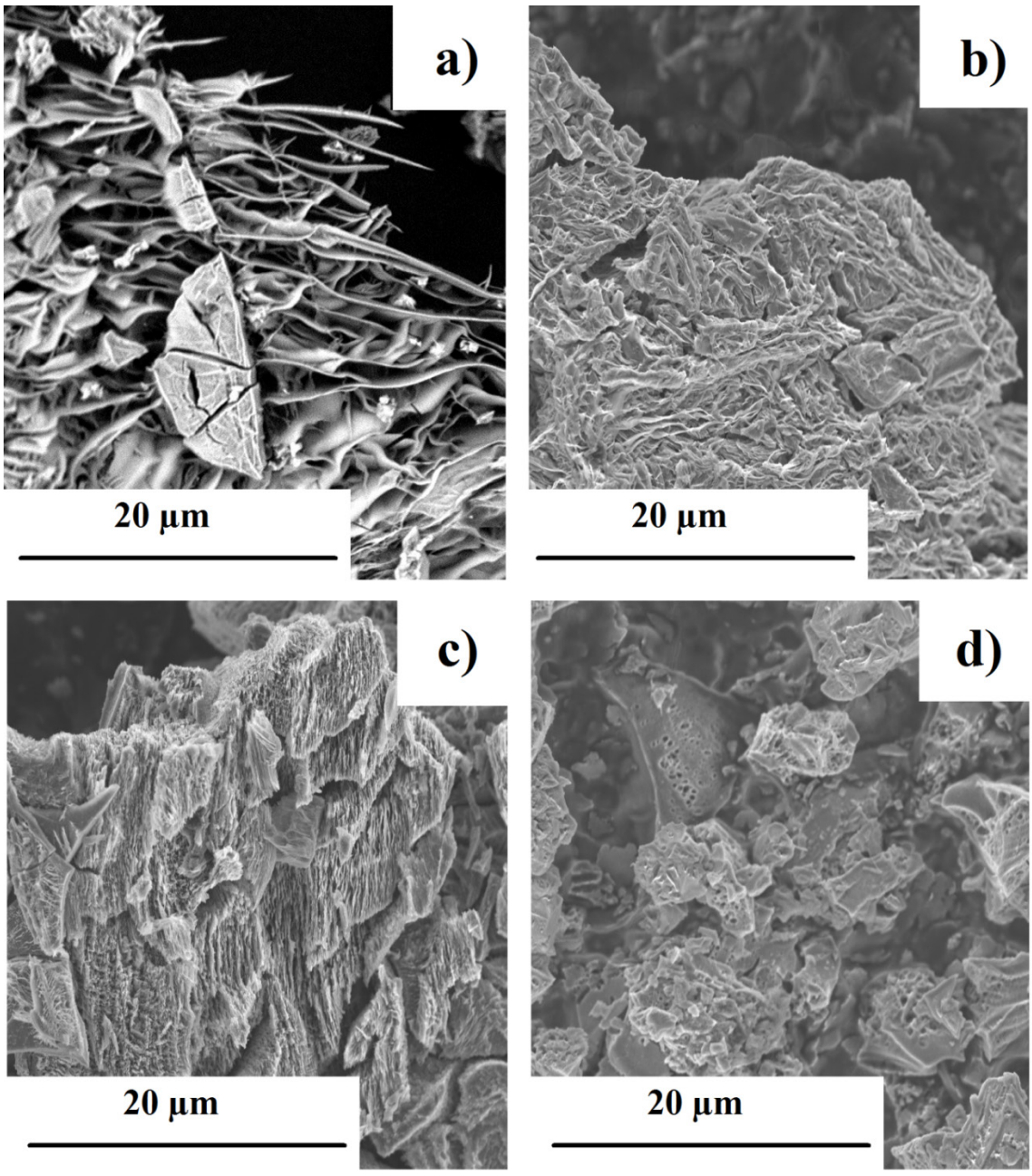

Figure 4.2 SEM images of a-Si prepared from the delithiation of $Li_{12}Si_7$, Li_7Si_3, $Li_{13}Si_4$, and $Li_{22}Si_5$ with ethanol are shown in (a-d), respectively.

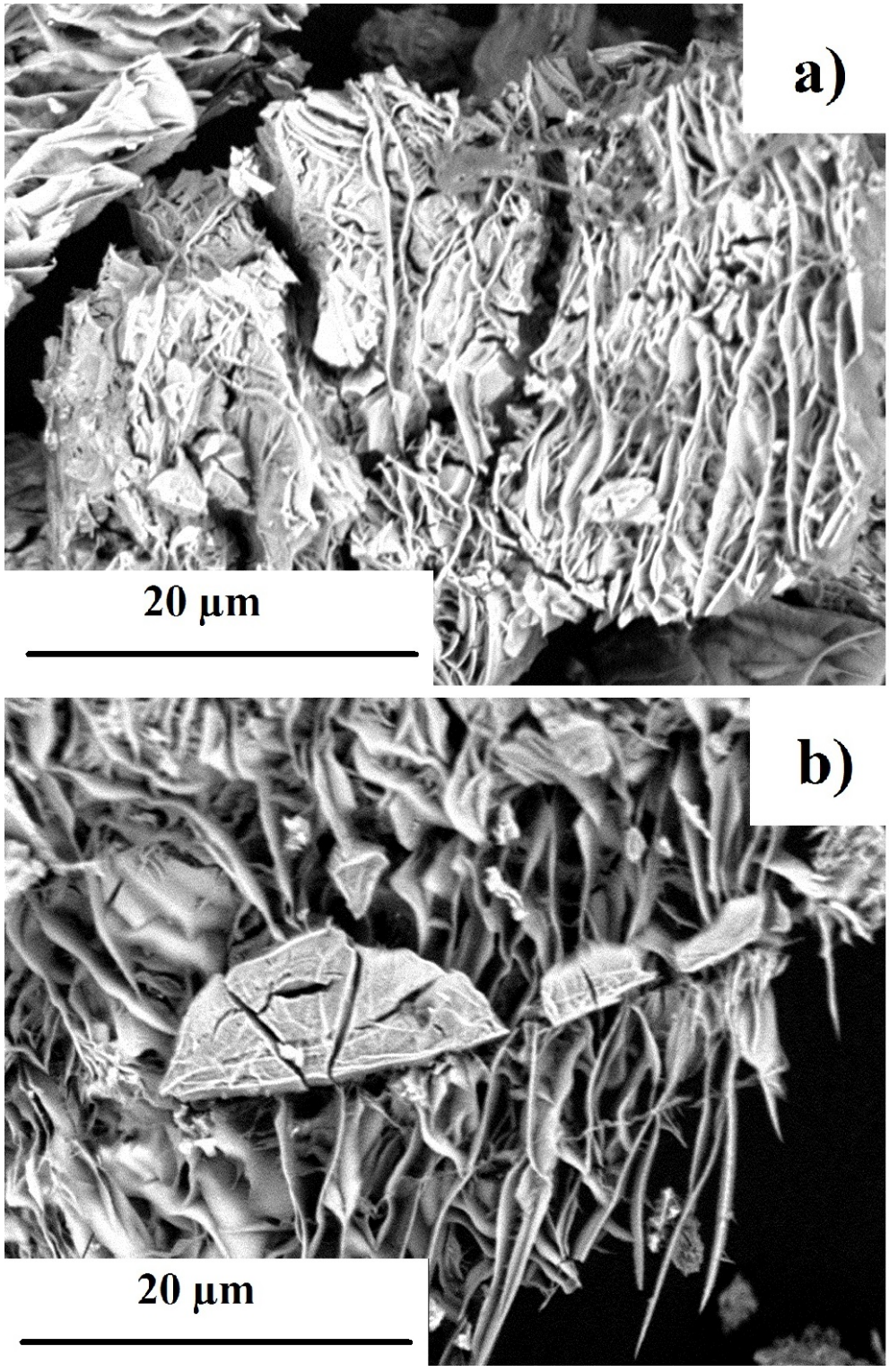

Figure 4.3 SEM images of a-Si prepared from the delithiation of $Li_{12}Si_7$ with ethanol.

The layeres are most striking in ethanol delithiated $Li_{12}Si_7$ and appear to be exfoliated, with large void spaces between the layers. In delithiated $Li_{13}Si_4$ the layered features are non-exfoliated with little void space between them, while delithiated Li_7Si_3 is comprised of disordered and highly buckled layeres. No layered structure could be identified in the sample of delithiated $Li_{22}Si_5$, which appears to be composed of non-porous particles.

According to previous studies, Si is present as small clusters in crystalline Li-Si phases [96, 97]. Figure 4.4 shows the crystalline structures of different Li-Si phases. All structural representations shown in Figure 4.4 were generated using VESTA [98]. Crystalline parameters (*e.g.* space group, cell dimensions, optimized coordinates of Wyckoff sites, *etc*.) of $Li_{22}Si_5$ were obtained from Reference 99. Crystalline parameters of all other Li-Si phases were obtained from Reference 96. $Li_{12}Si_7$ (or $Li_{24}Si_{14}$) has an orthorhombic lattice, containing two types of clusters, Si_5 rings and Si_4 Y-shaped clusters (Figure 4.4(d-f)). Each Si_5 ring is surrounded by 6 Li and each Si_4 Y-shaped cluster is surrounded by 12 Li. The stoichiometric ratio of Si_5 clusters to Si_4 clusters in $Li_{12}Si_7$ is 2:1. The unit cell of $Li_{12}Si_7$ can be described as $(Li_6^{6+}[Si_5]^{6-})_2(Li_{12}^{10+}[Si_4]^{10-})$ [96] or $(Li_6^{4+}[Si_5]^{6-})_2(Li_{12}^{12+}[Si_4]^{10-})$ [100]. Li_7Si_3 has a trigonal lattice, containing Si_2 dumbbells (Figure 4.4(c)). $Li_{13}Si_4$ has an orthorhombic lattice, containing a mixture of Si_2 dumbbells and single Si atoms (Figure 4.4(b)). $Li_{22}Si_5$ has a cubic lattice, containing only single Si atoms (Figure 4.4(a)). There are planar anisotropies in $Li_{12}Si_7$, Li_7Si_3 and $Li_{13}Si_4$ crystal structures, which may induce layering upon chemical delithiation.

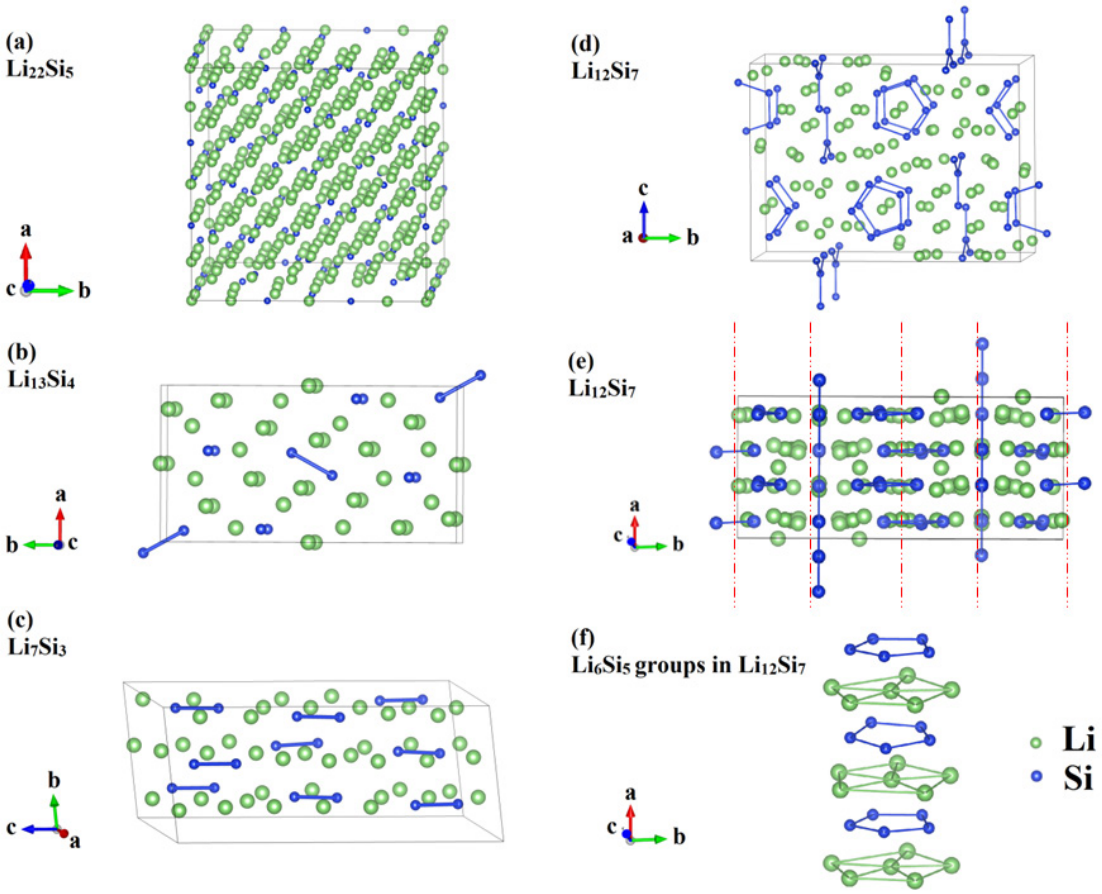

Figure 4.4 The crystalline Li-Si structures. Structures are not to scale relative to each other.

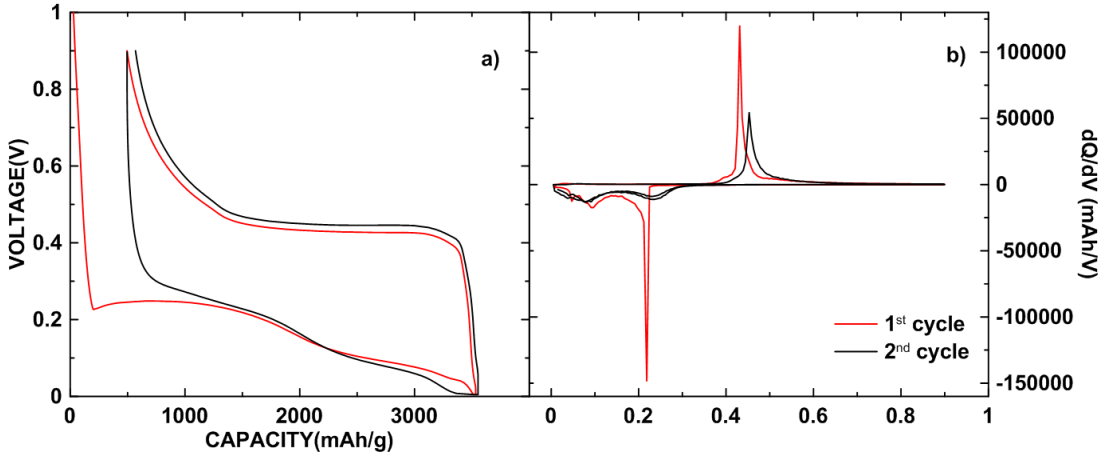

Figure 4.5 (a) Voltage profile and (b) differential capacity curve of a-Si made from ethanol delithiated $Li_{12}Si_7$.

Figure 4.5 shows the voltage curve and differential capacity curve of layered a-Si produced from ethanol delithiated $Li_{12}Si_7$. The voltage curve is typical of a-Si, with a sloping lithiation voltage curve and a plateau during delithiation corresponding to the cr-$Li_{15}Si_4$/a-Li_xSi 2-phase region [29-31]. All other a-Si samples made from delithiation in this study had similar voltage and differential capacity curves.

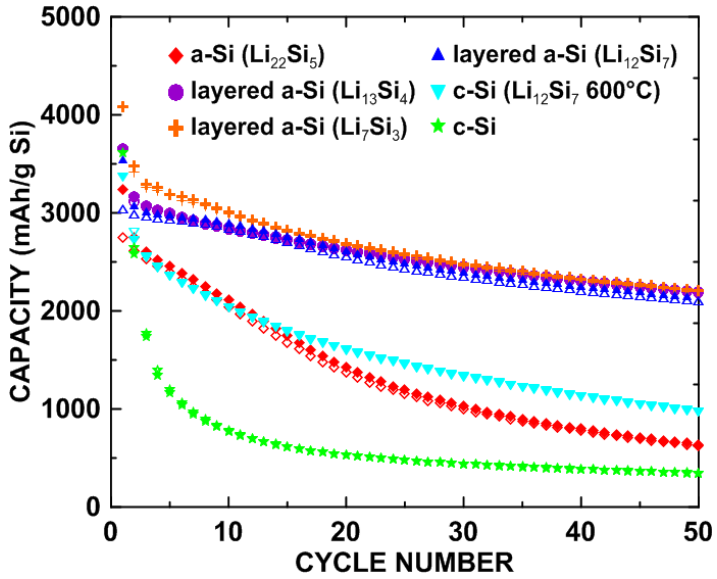

Figure 4.6 Cycling performance of cr-Si, a-Si electrodes prepared from ethanol delithiation of the indicated lithium silicide precursors, and of cr-Si made from a-Si heated to 600 °C. These coatings do not comprise graphite.

Figure 4.6 shows the cycling performance of a cr-Si electrode and a-Si electrodes made from ethanol delithiated $Li_{12}Si_7$, Li_7Si_3, $Li_{13}Si_4$, and $Li_{22}Si_5$ phases. The cycling performance of cr-Si cycled in its full voltage range is poor, as has been previously observed [31]. The cycling performance of a-Si prepared from delithiated $Li_{22}Si_5$, which had a non-porous structure, is slightly improved from that of bulk cr-Si. In contrast, the

cycling performance of a-Si as prepared from $Li_{12}Si_7$, Li_7Si_3, and $Li_{13}Si_4$, which resulted in layered structures, have greatly improved cycling performance as compared with cr-Si and maintain above 2000 mAh/g capacity after 50 cycles.

Table 4.1 Cycling performance of coin cells in this chapter. Here, RC = the 1st cycle reversible capacity, IC = the 1st cycle irreversible capacity, 50th Capacity = specific capacity after 50 cycles, Retention = 50th Capacity/RC, Exp. = volume expansion.

Delithiant	**Active Materials**	**RC (mA h/g)**	**IC (%)**	**50th Capacity (mA h/g)**	**Retention (%)**	**Exp. (%)**
-	cr-Si	2648±19	27±2	348±17	13	241±14
Ethanol	a-Si	3037±27	14±2	2293±32	76	135±3
Ethanol	a-Si/SFG6L (40/22.5)	2240±9	18±1	1680±8	75	72±6
Isopropanol	a-Si	2787±20	18±2	502±22	18	56±7
Isopropanol	a-Si/SFG6L (40/22.5)	1842±13	19±2	1437±11	78	52±3

To investigate the reason for the improved cycling performance of the layered a-Si electrodes, the volume expansion of electrodes containing cr-Si and a-Si made from $Li_{12}Si_7$ delithiation were measured before and after one full lithiation. It has been shown that the volume expansion of alloy electrodes is directly related to the expansion of alloy particles, with minimum change in electrode porosity [45]. The volume expansion of the cr-Si was measured to be 241±14 %, which is near the theoretical volume expansion of Si

(280% [31]). In contrast, the volume expansion of the layered a-Si electrode is much less, being only 135±3% at full lithiation. In order for this to occur, the volume expansion of Si during lithiation must be being accommodated in the void space between the layers of the layered a-Si. This greatly reduced volume expansion is likely the reason for the vastly improved cycling of the layered a-Si electrodes compared to the bulk cr-Si electrode.

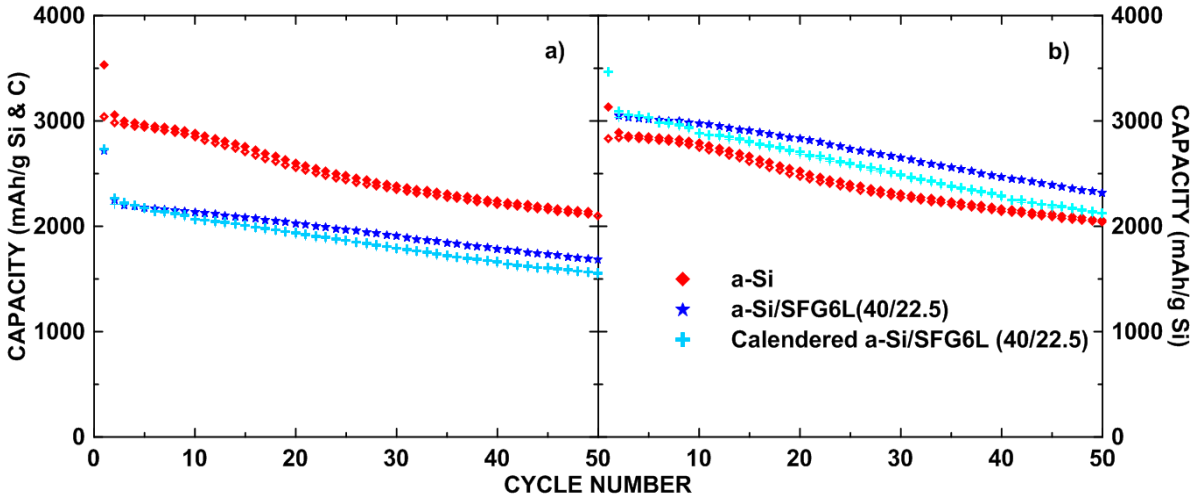

Figure 4.7 Cycling performance of a-Si, a-Si/SFG6L (40/22.5), and calendered a-Si/SFG6L (40/22.5) electrodes. The capacity is plotted in terms of (a) the total active material weight and (b) the a-Si active weight. All a-Si were prepared from $Li_{12}Si_7$ using ethanol.

It has been shown previously that the energy density and cycling performance of alloy electrodes can be improved if the alloy is blended with graphite and calendared to low porosity (~20%) [45]. Figure 4.7 shows the cycling performance of a-Si, a-Si/SFG6L (40/22.5), and calendered a-Si/SFG6L (40/22.5) electrodes. Table 4.1 lists the

volume expansion and cycling performance parameters of the electrodes shown in Figure 4.7. Here, all a-Si materials are prepared from $Li_{12}Si_7$ with ethanol delithiant. In Figure 4.7(a) the capacity is plotted in terms of the total active material weight. Figure 4.7(b) shows the capacities plotted with respect to the a-Si active weight, so that the a-Si performance in the electrodes could be compared. This was accomplished by subtracting the graphite and PI contributions from the cell capacity (graphite and PI were assumed to have reversible capacities of 372 mAh/g and 400 mAh/g, respectively). When graphite is added to the electrode, the utilized capacity of a-Si increases and cycling performance is improved. This effect has been observed previously [45]. When the a-Si/graphite electrode is calendered, the cycling performance does not change greatly, which is different from the previous study on non-porous alloys [45]. The layered a-Si structure may become damaged during the calendering process.

To investigate the influence of heat-treatment, a-Si powder made of ethanol delithiated $Li_{12}Si_7$ was heated at 550 °C or 600 °C for two hours. Figure 4.8(a-c) show the XRD patterns of the a-Si before and after heat-treatment. SEM images of the heated samples are shown in Figures 4.8(d-f).

When the heating temperature was 550 °C, sharp silicon peaks appeared in the XRD pattern, as shown in Figure 4.8(b). The SEM image of this sample indicates that sintering has commenced at the edges of the layers, which have started to become rounded due to the effects of surface tension. As the annealing temperature was increased to 600 °C, the XRD pattern became characteristic of cr-Si, as shown in Figure

4.8(c). The SEM image of this sample is shown in Figure 4.8(f). The layer structure has collapsed and the layers have become fused together, with the resulting volume contraction causing large cracks in the particle. The cycling performance of the 600 °C heated a-Si is included in Figure 4.6. Although its cycling performance is improved compared to that of bulk cr-Si, it is much worse compared to that of a-Si without heat-treatment.

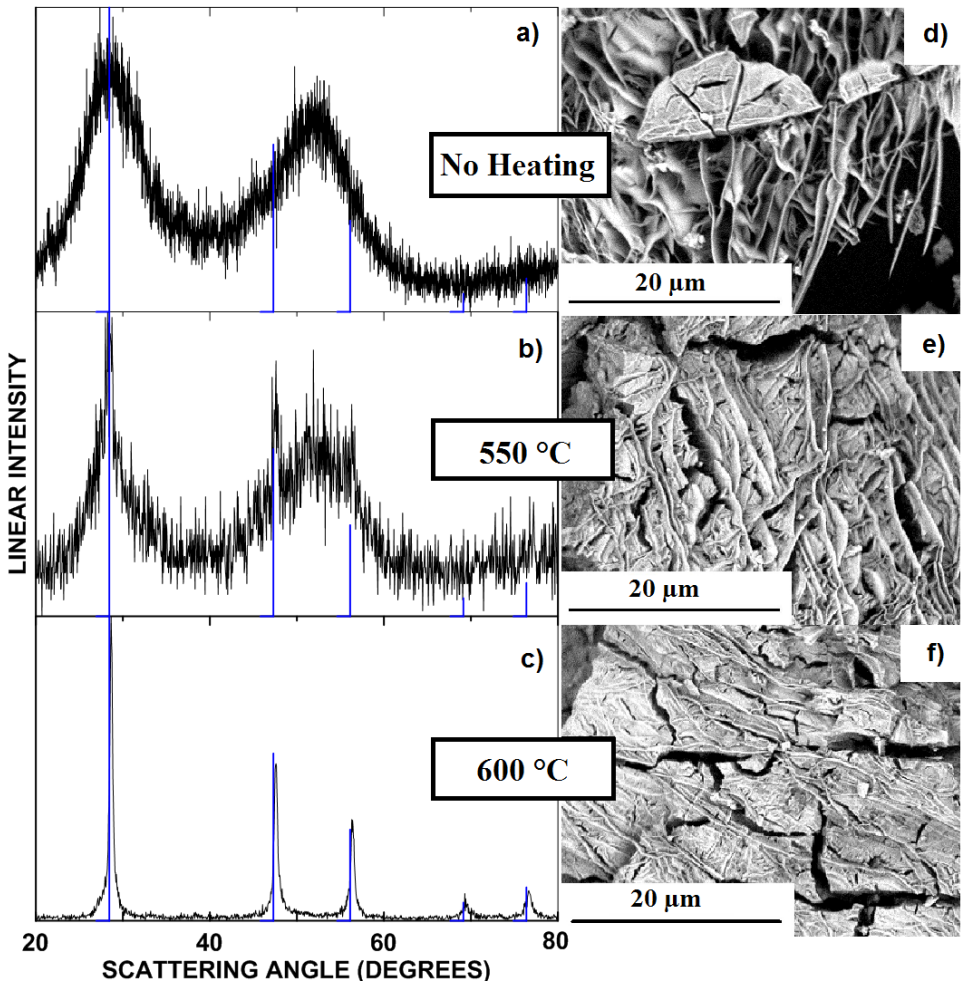

Figure 4.8 XRD patterns and SEM images of a-Si without heat-treatment and heated to 550 °C and 600 °C (a-c and d-f, respectively). The a-Si was prepared from ethanol delithiated $Li_{12}Si_7$. (Silicon: PDF# 00-027-1402).

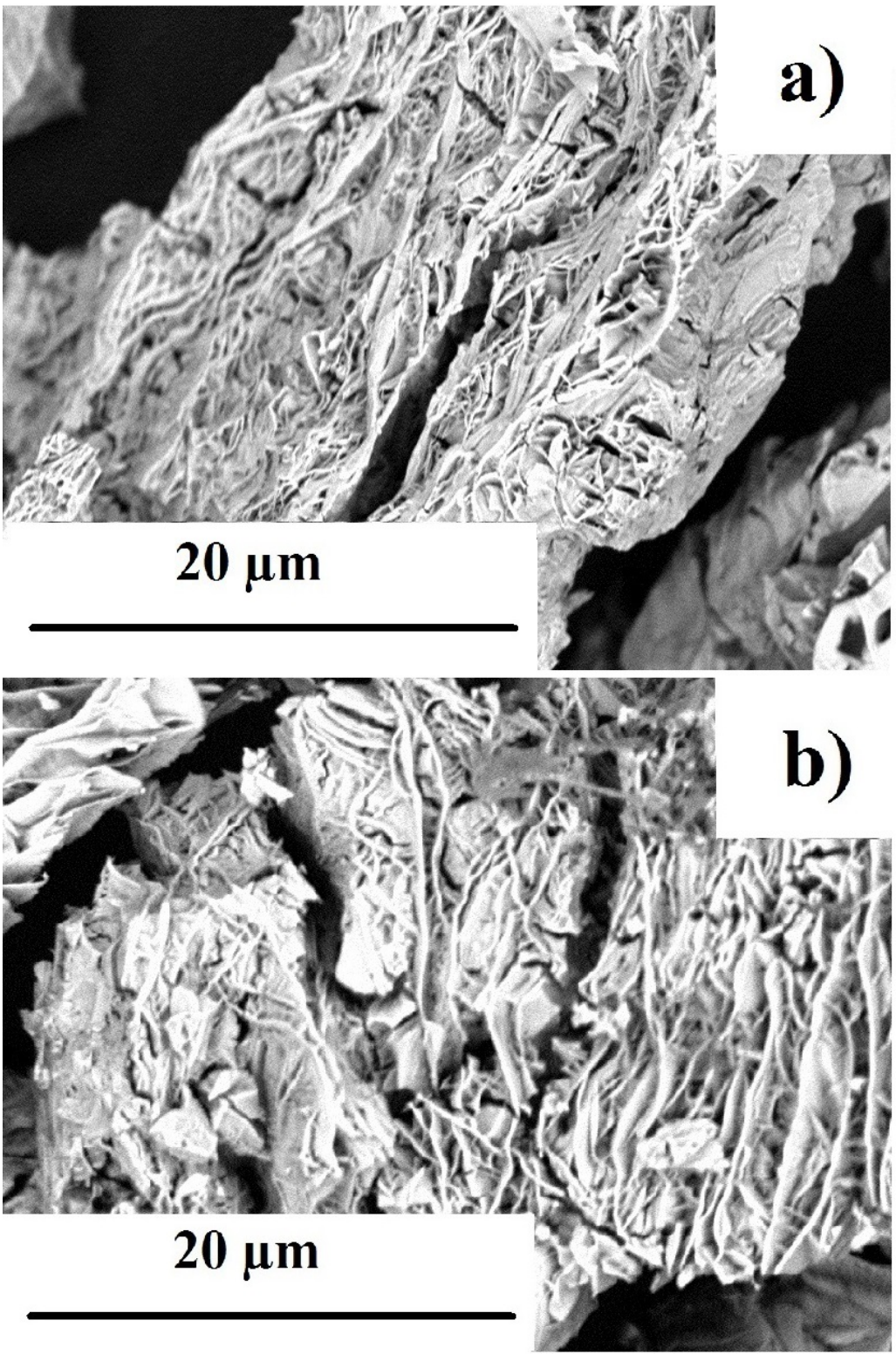

Figure 4.9 SEM images of a-Si prepared from $Li_{12}Si_7$ using (a) isopropanol and (b) ethanol as the delithiant.

To investigate the effect of the delithiant on sample morphology and cycling performance, a-Si was also prepared from $Li_{12}Si_7$ using isopropanol. Figure 4.9(a) shows the SEM image of a-Si prepared from isopropanol delithiant. Compared to a-Si prepared using ethanol, Figure 4.9(b), the a-Si prepared using isopropanol delithiant is comprised of less organized and more compact layers.

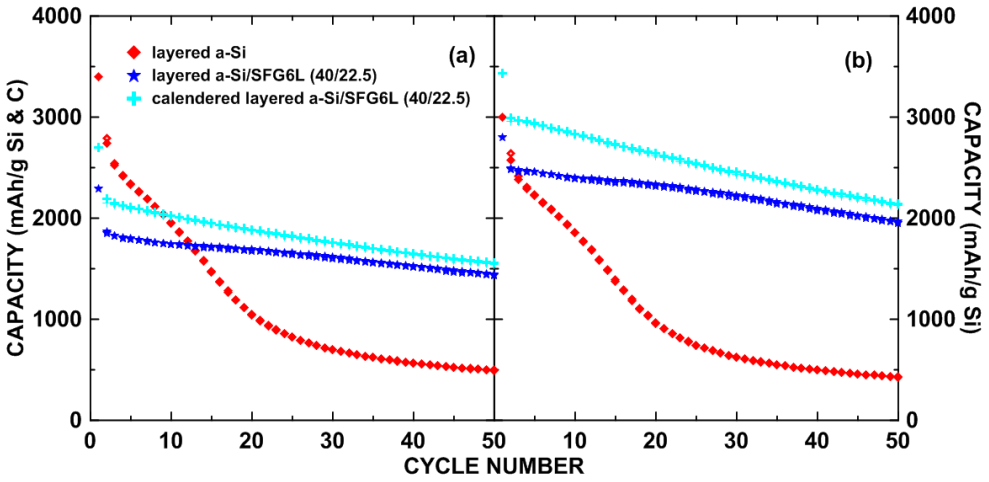

Figure 4.10 Cycling performance of a-Si, a-Si/SFG6L (40/22.5), and calendered a-Si/SFG6L (40/22.5) electrodes. The capacity is plotted in terms of (a) the total active material weight and (b) the a-Si active weight. All a-Si were prepared from Li12Si7 using isopropanol.

Figure 4.10 shows the cycling performance of electrodes formulated with a-Si prepared using isopropanol delithiant and their volume expansion and cycling performance parameters are listed in Table 4.1. In Figure 4.10(a) the capacity is plotted with respect to the total active weight, while in Figure 4.10(b) the capacity of the a-Si component is plotted only to the a-Si active weight, using the same procedure as with

Figure 4.7. The a-Si electrode with no graphite has severe capacity fade and much worse cycling performance compared to the electrode formulated with a-Si prepared with ethanol delithiant and no graphite, shown in Figure 4.7. Surpizingly the measured volume expansion of the a-Si prepared with isopropanol is only 56%, which is much smaller than that observed above for a-Si prepared from ethanol delithiant. This is not fully understood, but the delithiant used apparently has a significant impact on the resulting a-Si microstructure and cycling performance. Figure 4.10 also shows the cycling performance of the a-Si prepared from isopropanol when blended with graphite and also in calendered electrodes. These electrodes have almost identical performance as the a-Si/graphite electrodes using a-Si prepared using ethanol, shown in Figure 4.7. This suggests that the poor cycling performance of a-Si prepared from isopropanol electrodes with no graphite may have arison from a connectivity issue with the a-Si particles.

Method 2

XRD patterns of products made by Method 2 are shown in Figure 4.11. The finial products prepared with hexane and DMC did not yield silicon according to Figure 4.11(a) and (c). In comparison, after $Li_{12}Si_7$ reacted with isopropanol and was heated, the product had two obvious broad peaks, indicative of amorphous silicon, as shown in Figure 4.11(b). However, unidentified impurity peaks were also observed. Products prepared by Method 2 were not tested as electrodes. Method 2 was not further pursued because its poor results.

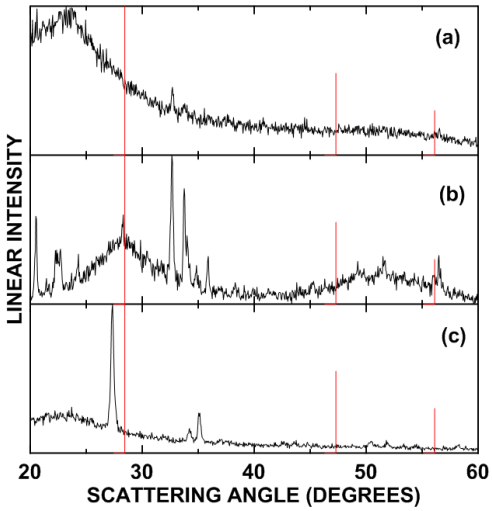

Figure 4.11 Products synthesized by Method 2 with (a) hexane, (b) isopropanol, and (c) DMC as delithiants, respectively. (Silicon: PDF# 00-027-1402).

4.4 CONCLUSION

In this chapter, bulk quantities of amorphous silicon were prepared by alcohol delithiation of Li-Si compounds (Method 1). Both ethanol and isopropanol were used for this purpose. Ethanol was found to be a more convenient delithiant than isopropanol and resulted in higher yields and products having superior cycling performance. Amorphous Si prepared from ethanol delithiation of $Li_{12}Si_7$, Li_7Si_3, $Li_{13}Si_4$, and $Li_{22}Si_5$ resulted in layered products, except in the case of $Li_{22}Si_5$, which was composed of dense particles. Amorphous Si prepared from ethanol delithiation of $Li_{12}Si_7$ had the most orderly layered structure, with the layers being highly exfoliated.

All amorphous Si samples prepared from alcohol delithiation had superior cycling performance compared to that of crystalline Si. This may be attributed to the low volume expansion (as low as 52 %) measured for these particles during cycling. It is thought that

the porous layered structure of these materials can accommodate the Si volume expansion during lithiation, resulting in low overall particle expansion. When heated to high temperatures, the layered structure collapsed and cycling performance deteriorated as a result.

The Method 1 reported here represents a means of producing low expansion nanostructured Si by using bulk chemical methods. Further applications of the alcohol delithiation method for making Si-based alloys are discussed in the next two chapters.

CHAPTER 5 CARBON-SILICON ALLOYS PREPARED BY DELITHIATION

5.1 INTRODUCTION

In Chapter 2, diverse methods to mitigate the Si volume expansion problem were discussed. One possible solution is the fabrication of carbon-silicon (C-Si) alloys. In C-Si alloys, carbon matrix acts as a "diluent" to the volume expansion of Si. Besides, fabrication of C-Si materials can combine the advantages of carbon (high electronic conductivity and long cycle life) and silicon (high capacity). C and Si are almost insoluble, according to their binary phase diagram, shown in Figure 5.1. SiC is the only equilibrium binary Si-C phase.

Ball milling has been widely applied to synthesize C-Si alloys, including mixing silicon with graphite [64-66] or other carbon precursors [67-69]. C-Si alloys (including C coated by Si and Si coated by C) containing micro-porous and nano-porous complex structures have also been produced by proper engineering procedures, such as chemical vapor deposition (CVD) and physical vapor deposition (PVD) [70-72]. Many C-Si alloys displayed improved cycling stability than bulk cr-Si and higher capacity than pure carbon materials [64-72]. Recently, the introduction of void spaces between the carbon coatings and silicon materials has been proposed to accommodate the large volume expansion of Si. The "core-shell" (carbon covered on silicon) materials have been designed and tested as Li-ion cell negative electrodes, which showed superior cycling performance than that of bulk cr-Si [73, 74].

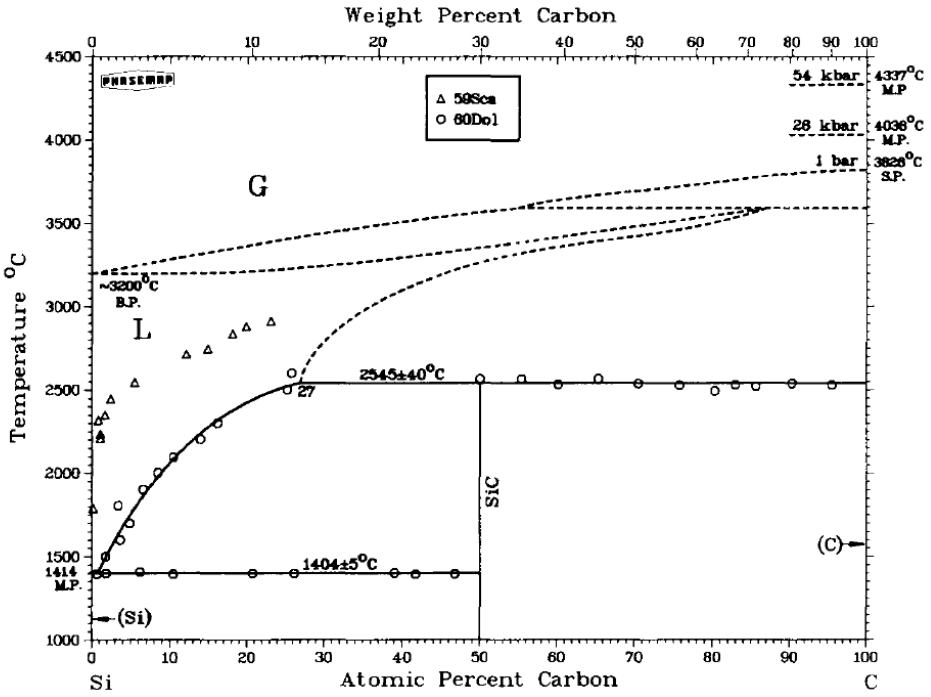

Figure 5.1 C-Si binary phase diagram [101].

In this chapter, carbon-lithium-silicon (C-Li-Si) alloys were prepared as precursors. C-Si alloys were synthesized by the delithiation of C-Li-Si using the alcohol delithiation method introduced in Chapter 4. C-Si alloys in serial C:Si stoichiometric ratios were studied with XRD and SEM. When tested as electrodes in Li cells, the as-prepared C-Si alloys showed superior electrochemical characteristics and lower volume expansion than that of bulk cr-Si.

5.2 EXPERIMENTAL

Synthesis of C-Si Alloys

The $Li_{12}Si_7$ intermetallic compounds were first synthesized with an arc furnace by melting about 1.2 g of Li (99.90% Li ribbon, Sigma) and Si (98.40% Si lump, Alfa Aesar) with a 7% excess of Li (to offset Li loss from vaporization) in a stoichiometric ratio

under an Ar-flow. After cooling down, the resulting Li-Si hemispherical slug was ground into powder with a mortar and pestle in an Ar-filled glove box.

The $Li_{12}Si_7$ powder was then mixed with graphite (MAG-E, Hitachi, average size of 20 μm) in a 65 mL hardened steel vial containing 115 g of 3/16" stainless steel balls under an argon atmosphere for 2 hours (rotating 180° every hour) using a SPEX mill (Model 8000-D, Spex Certiprip, Metuchen, M.J.). C-Li-Si alloys in serial C:Si stoichiometric ratios were prepared as shown in Table 5.1.

Table 5.1 Mass of $Li_{12}Si_7$ and MAG-E for the preparation of C-Li-Si alloys.

C:Si (Stoich. Ratio)	**$Li_{12}Si_7$ (g)**	**MAG-E (g)**
90:10	0.5433	1.4688
80:20	0.8503	1.0217
70:30	1.0476	0.7343
60:40	1.1851	0.5340
50:50	1.2865	0.3864
40:60	1.3642	0.2732

The C-Li-Si alloys were delithiated by adding ~1.5 g of C-Li-Si powder into a round bottom flask affixed with a Vigreux condenser. About 120 mL of ethanol (99.89%, containing 0.10% H_2O, Commercial Alcohols) was added to the flask and stirred continuously by a magnetic stirrer. The reaction proceeded overnight. The whole process was conducted in an Ar-filled glovebox.

After delithiation reactions, the resulting product was transferred into a Büchner funnel (with 44.25 mm filter paper, Whatman) and was washed with distilled water for 3 times, HCl (1 mol/L, prepared from 37% HCl, Aldrich) for 3 times and distilled water again until the pH of the washing water was about 7. The air / water stable product was then heated in a tube furnace at 120 °C for 1 hour and 300 °C for 3 hours under an Ar-flow.

X-ray Diffraction (XRD), Scan Electron Microscopy

XRD patterns were collected with a Rigaku Ultima IV diffractometer equipped with a copper target, a dual position graphite diffracted beam mono-chromator and a scintillation counter detector. XRD data were collected at a scattering angle (2θ) range of 20 to 80 degrees with a single step of 0.05 degree and a 6 second (or 3 second) dwell time. Particle size and morphology of C-Si alloys were studied with a Hitachi S-4700 FEG Scanning Electron Microscope. Sample density was measured by a helium Pycnometer (AccuPyc II 1340, Micrometritics).

Electrochemical Characterization

Electrode slurries were prepared by mixing C-Si alloys (active material), carbon black (Super-P, Erachem Europe) and polyimide (PI, PI-2555, HD Microsystems) in N-methyl pyrrolidinone (NMP, 99.50%, Sigma). The formulation of all electrode coatings was C-Si/carbon black/PI in a ratio of 62.5/18/19.5 by volume. The slurries were prepared with a planetary ball mill (Retsch PM 200) with four 7/16" WC balls at 100 rpm for 1 hour. The resulting slurries were coated on copper foil (Furukawa Electric, Japan)

with a 0.004 inch coating bar and then dried at 120 °C in air for 1 hour. Circular working electrodes (d=13 mm) were punched from the coated foil and heated in a tube furnace at 300 °C under an Ar-flow for 3 hours, in order to cure the PI binder.

Electrodes were transferred into an Ar-filled glove box and assembled in 2325 coin-type cells, as shown in Figure 3.7, with a lithium foil reference/counter electrode. Two layers of Celgard 2300 separators, one stainless steel spring and one spacer were used in each coin cell. 1M $LiPF_6$ (BASF) in a solution of Monofluoroethylene carbonate (FEC), ethylene carbonate (EC) and diethyl carbonate (DEC) (in a volume ratio of 1:3:6, all from Novolyte Technologies) was used as electrolyte. All coin cells were cycled at 30.0±0.1 °C between 0.005 V - 0.9 V with a Maccor Series 4000 Automated Test System at a C/20 rate and trickle discharged to C/40 rate for the 1^{st} cycle, and at a C/5 rate and trickle discharged to a C/20 rate for the following cycles. All coin cells had a rest period of 15 minutes at open circuit at the end of each half-cycle. C-rate was calculated based on capacity of 3579 mAh/g for Si [29] and of 600 mAh/g for ball milled graphite [102]. To test the volume expansion of C-Si electrodes, electrode thicknesses were measured in an Ar-filled glove box to within ±1 μm with a Mitutoyo 293-340 precision micrometer before assembling cells and after one full lithiation (C/20 constant current with a C/40 trickle, and 5 mV as lower voltage limit).

5.3 Results and Discussion

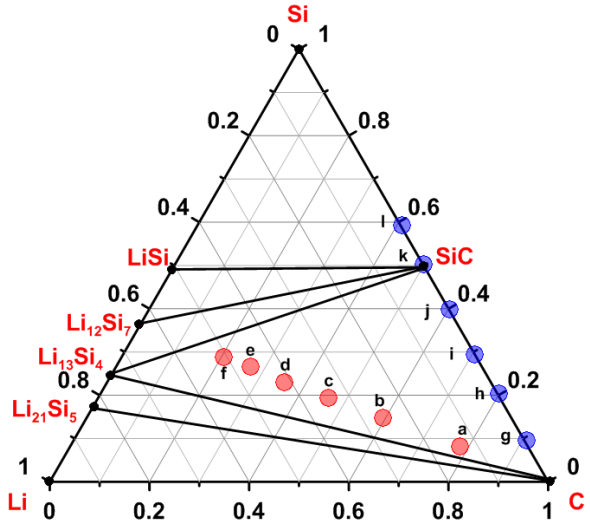

Figure 5.2 The C-Li-Si ternary system at 0 K as predicted by the Materials Project [103, 104]. Red dots (a-f) represent the compositions of C-Li-Si alloys synthesized by ball milling in C:Si stoichiometric ratios of 90:10, 80:20, 70:30, 60:40, 50:50, and 40:60, respectively; blue dots (g-l) represent the compositions of C-Si alloys in C:Si stoichiometric ratios of 90:10, 80:20, 70:30, 60:40, 50:50, and 40:60, respectively, after delithiation.

Figure 5.2 shows the C-Li-Si ternary system. Red dots represent compositions of C-Li-Si precursors and blue dots represent compositions of C-Si alloys. Figure 5.3(a-f) show the XRD patterns of C-Li-Si alloys after mixing $Li_{12}Si_7$ with MAG-E in serial C:Si stoichiometric ratios, corresponding to red dots (a-f) in Figure 5.2. There are two broad peaks in each of Figure 5.3(a-f). To identify these two peaks, $Li_{12}Si_7$ and MAG-E were milled separately using the same condition to synthesize C-Li-Si alloys. XRD patterns of $Li_{12}Si_7$ and MAG-E before and after ball milling were shown in Figure 5.4. After 2 hours

milling, both $Li_{12}Si_7$ and MAG-E had broad peaks at similar positions, indicative of amorphous phases. One can speculate that the two broad peaks in Figure 5.3(a-f) are a combination of the two broad peaks in XRD patterns of $Li_{12}Si_7$ and MAG-E after ball milling. The broad peaks in Figure 5.4(d) also suggest that the crystalline structure of MAG-E has been destroyed.

Previous research has shown that SiC compounds form after ball milling Si and C powders [94, 105]. However, no SiC peaks appear in Figure 5.3(a-f). To identify if there was SiC formed during ball milling C-Li-Si alloys, crystalline Si (-325 mesh, 98%, Aldrich) and graphite (MAG-E, Hitachi, average size of 20 μm) powders were milled in 1:1 mole ratio using the same conditions to prepare C-Li-Si alloys. As shown in Figure 5.5, SiC peaks can be easily observed from the product of milling Si and C, indicative of the formation of a nano-crystalline SiC phase. This implies that while Si ball milled directly with C forms SiC, SiC formation can be avoided by alloying the Si with Li prior to ball milling, as shown in Figure 5.3(a-f). It should be noted that ball milling is a non-equilibrium process, therefore resulting C-Li-Si alloys may not comprise the phases suggested by the equilibrium phase diagram, shown in Figure 5.2.

Bulk quantities of air / water stable C-Si powders were prepared by delithiation of C-Li-Si alloys with ethanol in an Ar-filled glovebox, probably according to the reaction:

$$Li_{1+z}Si_xC_y\,(s) + R\text{-}OH\,(l) \rightarrow R\text{-}OLi\,(s) + \tfrac{1}{2}\,H_2\,(g) + Li_zSi_xC_y\,(s). \qquad (5.1)$$

The alkoxide products (R-OLi) were insoluble in ethanol, and were subsequently washed away by rinsing with HCl and water. There is possibly Li remained in $Li_zSi_xC_y$ alloys after reaction. The remaining Li was washed away by rinsing with HCl and water. The resulting C-Si powders were produced in an average yield of 79 % by weight.

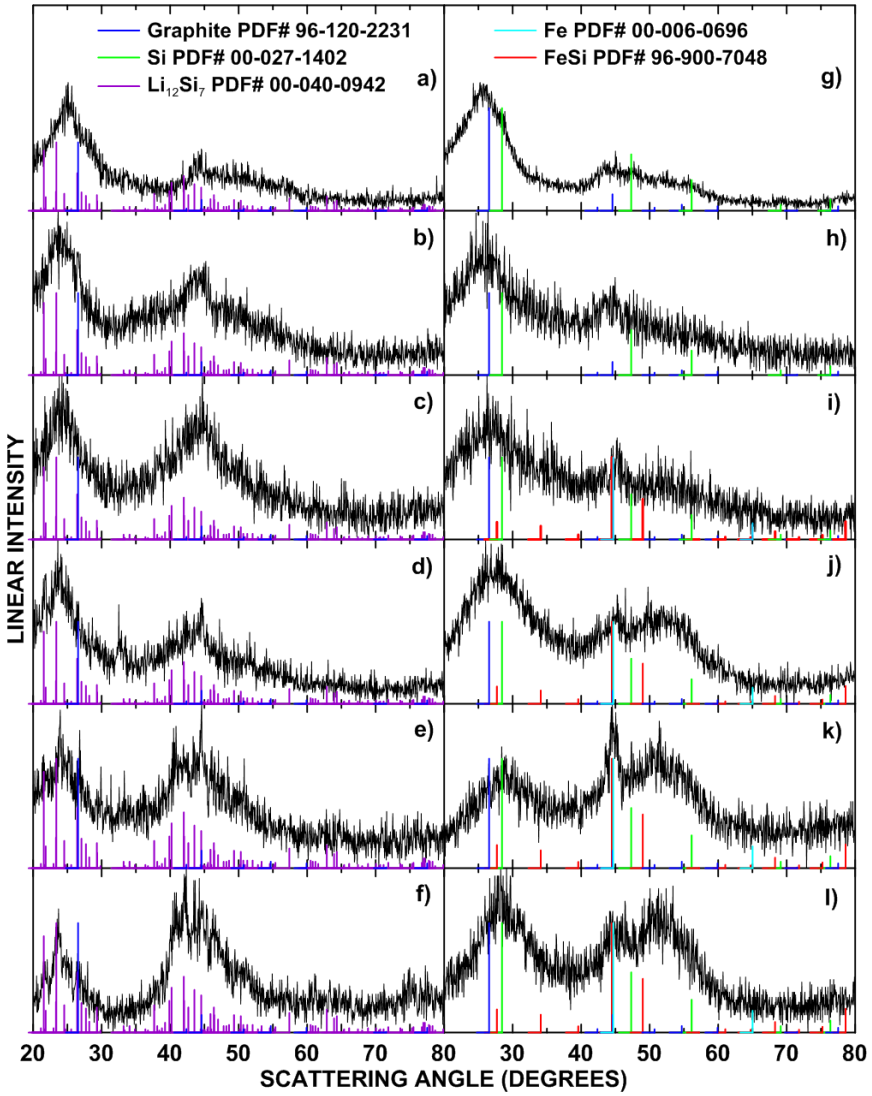

Figure 5.3 XRD patterns of (a-f) C-Li-Si alloys and (g-l) C-Si alloys in C:Si stoichiometric ratios of 90:10, 80:20, 70:30, 60:40, 50:50, and 40:60, respectively.

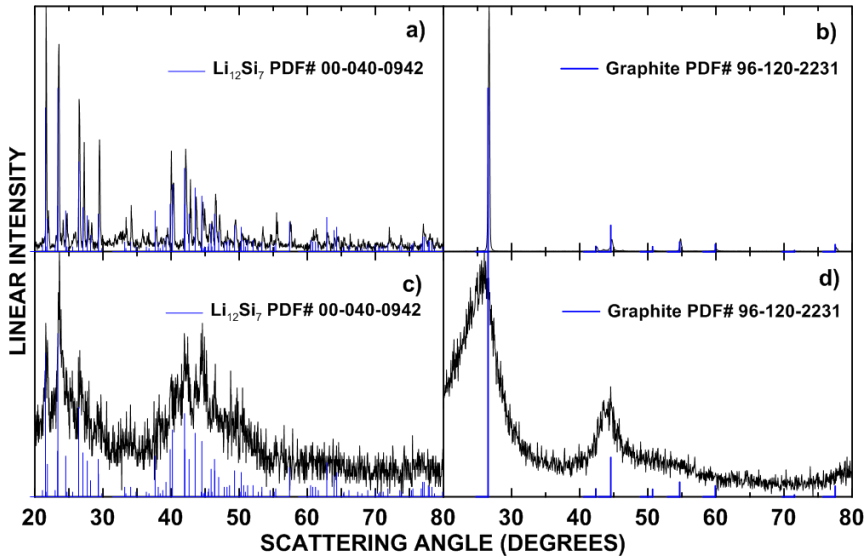

Figure 5.4 XRD patterns of (a) $Li_{12}Si_7$ prepared by arc melting, (b) MAG-E, (c) $Li_{12}Si_7$ after 2 hours ball milling, and (d) MAG-E after 2 hours ball milling.

Figure 5.3(g-l) show the XRD patterns of C-Si alloys in serial C:Si stoichiometric ratios, corresponding to blue dots (g-l) in Figure 5.2. According to Chapter 4, two broad peaks near 29 and 51 degrees should appear in XRD patterns of delithiated Li-Si products, indicative of a-Si. In Figure 5.3(g-i) (corresponding to $C_{90}Si_{10}$, $C_{80}Si_{20}$, and $C_{70}Si_{30}$, respectively), there is a high broad peak near 29 degrees and a low broad peak near 45 degrees, indicative of amorphous carbon, which is similar to Figure 5.4(d). There is also a very low broad hump around 51 degrees, indicative of a-Si, as was desired. In Figure 5.3(j-l) (corresponding to $C_{60}Si_{40}$, $C_{50}Si_{50}$, and $C_{40}Si_{60}$, respectively), the broad hump around 51 degrees becomes higher, indicative of more a-Si content. In Figure 5.3(h-l), a narrow peak appears at ~45°. This peak is speculated to be from FeSi or Fe

impurities, where the Fe is introduced from stainless steel balls during ball milling. Further testing by inductively coupled plasma (ICP) analysis and Mössbauer spectroscopy is in progress to measure the Fe impurity content and its identity. To summarize the results presented in Figure 5.3(g-l), C-Si alloys composed of amorphous C and a-Si with Fe or FeSi impurities were obtained after milling and delithiating C-Li-Si alloys.

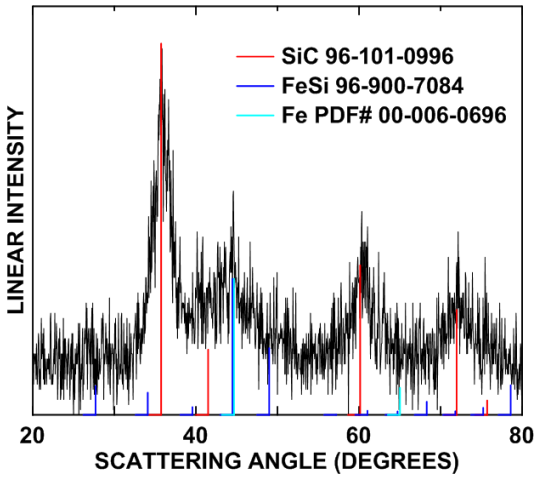

Figure 5.5 XRD pattern of ball milled Si-C in 1:1 mole ratio.

The morphology and particle size of C-Si powders were characterized by SEM. Figure 5.6 shows the SEM images of the C-Si alloys at different magnifications. The overall particle size of all samples ranges from 5 μm to 40 μm. Most particles have a diameter of 10~20 μm. Different C:Si ratios seem not to influence particle sizes.

Unlike a-Si in Figure 4.2(a), no layered structure was observed in the C-Si alloys in Figure 5.6. Large particles are composed of smaller particles, which are cemented together. No obvious difference can be observed among different C-Si powders.

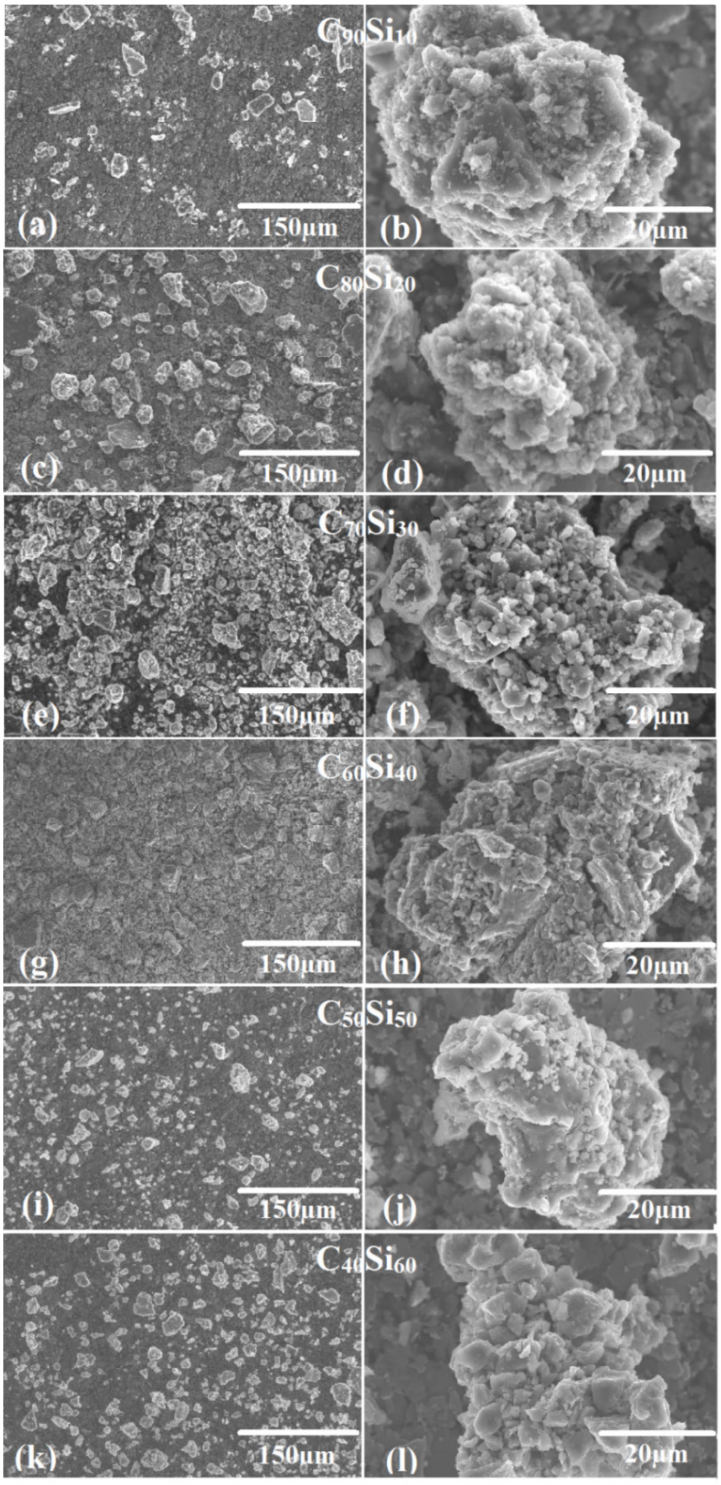

Figure 5.6 SEM images of C-Si alloys with C:Si stoichiometric ratios of 90:10, 80:20, 70:30, 60:40, 50:50, and 40:60 (a-l, respectively) at different magnifications.

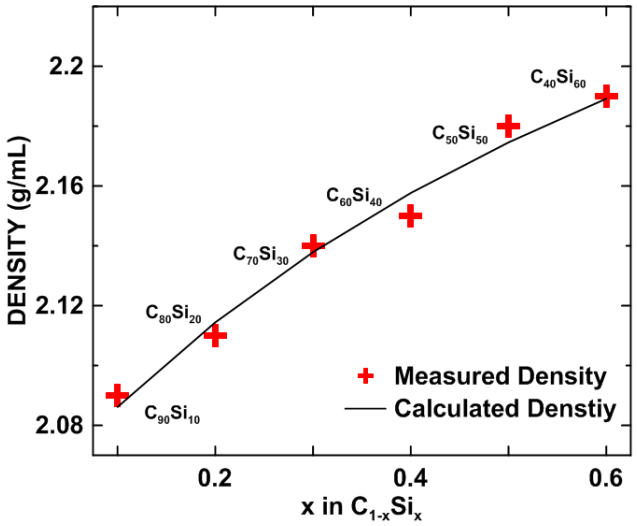

Figure 5.7 Density of C-Si alloys as measured by a helium Pycnometer (AccuPyc II 1340, Micrometritics). Red spots represent the measured values and the black solid line represents the calculated values.

Table 5.2 Density of C-Si alloys in g/mL.

	$C_{90}Si_{10}$	$C_{80}Si_{20}$	$C_{70}Si_{30}$	$C_{60}Si_{40}$	$C_{50}Si_{50}$	$C_{40}Si_{60}$
Density (g/mL)	2.0908 ±0.0057	2.1138 ±0.0013	2.1380 ±0.0060	2.1531 ±0.0037	2.1788 ±0.0054	2.1945 ±0.0040

C-Si alloy density increases dependent on the silicon content, as shown in Figure 5.7 (data were listed in Table 5.2). This trend in density corresponds well to a mixture of ball milled C and Si, if the density of ball milled C and Si are assumed to be 2.05 g/ml and 2.23 g/ml, respectively. Considering that all sample densities are less than that of a simple mixture of graphite and cr-Si, this implies that any Fe contamination is small.

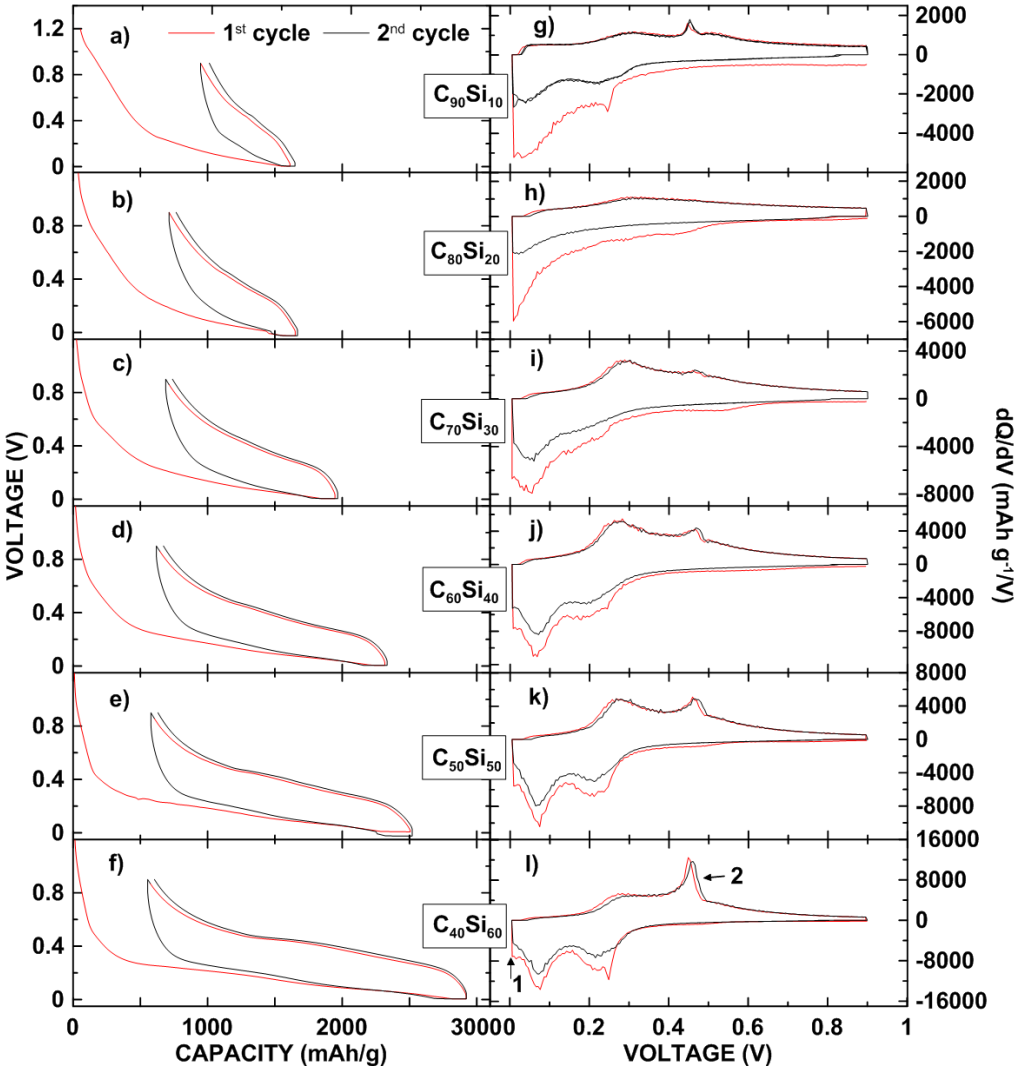

Figure 5.8 Voltage curves and differential capacity curves of C-Si electrodes. Peak 1 might indicate the formation of cr-$Li_{15}Si_4$. Peak 2 might indicate a two-phase region of cr-$Li_{15}Si_4$/a-Li_zSi.

Figure 5.8 shows the voltage curves and differential capacity curves of C-Si electrodes. There are no plateaus indicating staging near 0.15 V in Figure 5.8(a-f), and no sharp peaks near 0.15 V in Figure 5.8(g-l), suggesting the layered structure of graphite has been destroyed [106]. Most voltage curves of C-Si ($C_{90}Si_{10}$, $C_{70}Si_{30}$, $C_{60}Si_{40}$, $C_{50}Si_{50}$,

and $C_{40}Si_{60}$) electrodes have two sloping plateaus near 0.1 V and 0.2 V during the 1st lithiation in Figure 5.8(a, c-f), corresponding to two broad peaks in Figure 5.8(g, i-l). This is indicative of typical single-phase regions of a-Si lithiation [31, 107]. Figure 5.8(a, c-f) also have two plateaus near 0.4 V during delithiation, indicating a single-phase region of a-Li_xSi delithiation [31]. In contrast, the a-Si electrode shows a well-defined plateau in Figure 4.5(a) and a sharp peak in Figure 4.5(b) during delithiation, indicating a two-phase region (cr-$Li_{15}Si_4$/a-Li_zSi). This difference suggests that no crystalline $Li_{15}Si_4$ formed during lithiation of the C-Si electrodes even though the voltage was below 50 mV. This is consistent with previous research that the crystallization of $Li_{15}Si_4$ during lithiation is not a feature typically seen in nanostructured alloy negative electrodes [9]. However, $C_{40}Si_{60}$ seems have small narrow peaks (peak 1 and 2 as labeled in Figure 5.8(l)), suggesting that high Si content may lead to the formation of cr-$Li_{15}Si_4$. The $C_{80}Si_{20}$ electrode is an exception. Its voltage curve is smooth and continuous during lithiation and there are no distinct peaks in its differential capacity curve.

Figure 5.9 and Table 5.3 show the cycling performance of C-Si electrodes in Li cells. As the silicon content increases, the reversible capacity and the specific capacity after 50 cycles of the C-Si electrodes increase greatly. When the silicon content is low ($C_{90}Si_{10}$, $C_{80}Si_{20}$, and $C_{70}Si_{30}$), the cycling is very stable and the retention after 50 cycles is high (>90%). However, high carbon contents result in high irreversible capacity. Figure 5.9(b) shows the coulombic efficiency (CE) of C-Si electrodes. The CE of low-

silicon-content electrodes ($C_{80}Si_{20}$, $C_{70}Si_{30}$, and $C_{60}Si_{40}$) increases rapidly to 99.8% in the first 10 cycles and keeps stable until the 50th cycle. The CE of the $C_{90}Si_{10}$ electrode also increases rapidly in the first 10 cycles and keeps increasing to 99.5% until the 50th cycle. When the Si content is high ($C_{50}Si_{50}$ and $C_{40}Si_{60}$), the CE jumps to 99.7% in the first 10 cycles, but decreases afterwards, especially in the case of $C_{40}Si_{60}$ electrode.

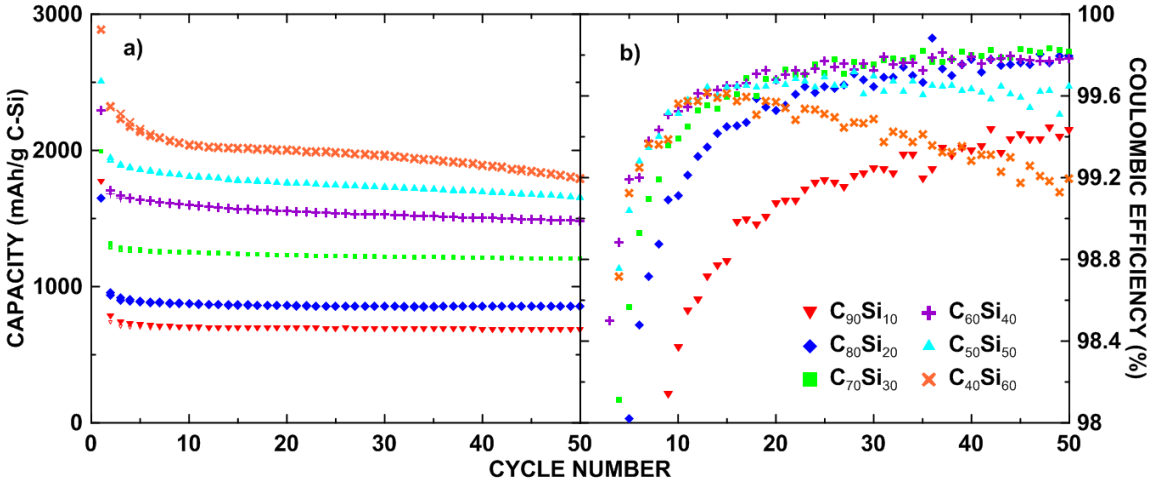

Figure 5.9 (a) Cycling performance and (b) coulombic efficiency (CE) of C-Si electrodes.

Figure 5.10 shows the calculated and measured capacities of serial C-Si electrodes. It was assumed that C:Si ratios remained unchanged before and after ball milling and chemical delithiation. The calculation (for the red line) of C-Si electrode capacities was based on 3579 mAh/g of silicon and 600 mAh/g of ball milled carbon [102]. It is observed that the capacity of C-Si electrode is almost linearly dependent on the silicon content. The measured capacities are 55~79% of the calculated values (of the red line). These low values could arise from a number of sources: lower reversible

capacity of a-Si (3037±27 mAh/g) than theoretical capacity (3579 mAh/g) according to Chapter 4, dissolution of Si during chemical delithiation, formation of Si-O phases during chemical delithiation, the formation of FeSi from Fe impurities during ball milling or the formation of amorphous SiC phases that were undetectable by XRD. Another reason to explain the difference between the measured and calculated capacity is that the capacity of ball milled carbon is not 600 mAh/g [102]. The dashed line in Figure 5.10 shows the most match calculated capacity by assuming 2792 mAh/g of Si and 22 mAh/g of ball milled carbon. The capacity of Si (2792 mAh/g) is close to the measured a-Si reversible capacity (3037±27 mAh/g according to Chapter 4) while the capacity of ball milled carbon (22 mAh/g) is much lower than 600 mAh/g from Reference 102.

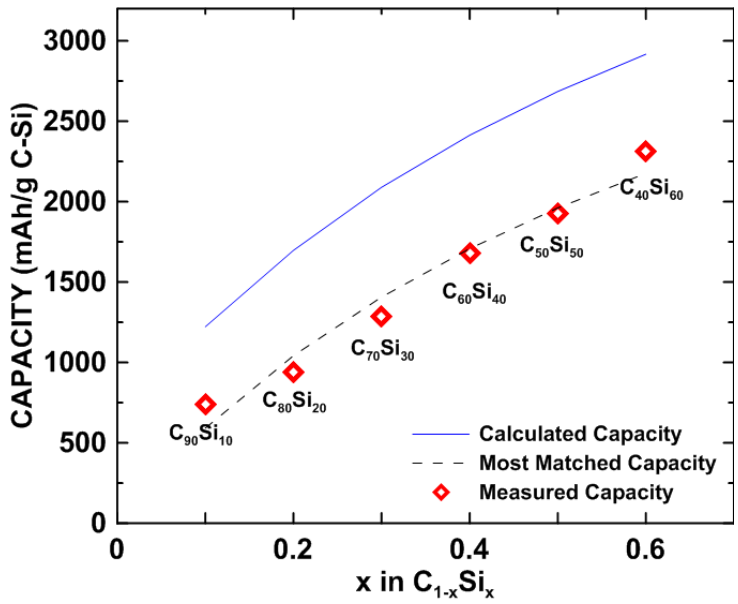

Figure 5.10 Calculated, measured and the most matched reversible capacities of C-Si electrodes *vs.* x in $C_{1-x}Si_x$.

Table 5.3 Cycling performance of serial C-Si electrodes. Here, RC = the 1st cycle reversible capacity, IC = the 1st cycle irreversible capacity percentage, 50th Capacity = specific capacity after 50 cycles, Ret. = 50th Capacity/RC, Exp. = volume expansion, initial and final porosity were obtained by calculating.

Active Material	**RC (mAh/g)**	**IC (%)**	**50th Capacity (mAh/g)**	**Ret. (%)**	**Exp. (%)**	**Initial Porosity (%)**	**Final Porosity (%)**	**Porosity Reduction (%)**
$C_{90}Si_{10}$	738±2	58±0	678±1	92	21±1	81±2	64±4	21±4
$C_{80}Si_{20}$	937±5	43±1	854±4	91	25±5	89±2	78±1	12.4±1
$C_{70}Si_{30}$	1287±11	35±2	1204±8	94	78±15	79±2	68±5	13.9±4
$C_{60}Si_{40}$	1683±13	27±1	1484±9	88	157±11	81±2	78±2	3.7±1
$C_{50}Si_{50}$	1927±11	23±2	1655±8	86	120±13	77±2	67±2	13±3
$C_{40}Si_{60}$	2315±17	20±2	1803±11	78	213±13	79±1	76±1	3.8±1

To investigate the volume expansion of C-Si electrodes, electrode thickness was measured before and after one full lithiation. As shown in Table 5.3, higher silicon content leads to larger volume expansion. When the silicon content is low ($C_{90}Si_{10}$, $C_{80}Si_{20}$, and $C_{70}Si_{30}$), the volume expansion is as low as 21%, corresponding to stable cycling performance and high retention. As the silicon content increases ($C_{60}Si_{40}$ and $C_{50}Si_{50}$), the volume expansion after one full lithiation rises to >100% (similar to that of a-Si delithiated from $Li_{12}Si_7$ with ethanol). It is noticeable that although $C_{50}Si_{50}$ contains

more silicon than $C_{60}Si_{40}$, the volume expansion of $C_{50}Si_{50}$ electrode is smaller. $C_{40}Si_{60}$ is composed of the most Si among all synthesized C-Si alloys and its volume expansion is 213%, which is much higher than that of a-Si shown in Table 4.1 (135%). This might account from different structures of $C_{40}Si_{60}$ and a-Si made with ethanol. The a-Si discussed in Chapter 4 has a layered structure, which might accommodate the Si volume expansion during lithiation. $C_{40}Si_{60}$ does not have a layered structure, and thus its volume expansion is high.

However, it is interesting that the cycling stability of $C_{40}Si_{60}$ (retention 78%) is similar to that of a-Si (retention 76%), even though the volume expansion of $C_{40}Si_{60}$ electrode is high. It is speculated that carbon helps Si particles keep from becoming isolated.

Table 5.4 Density of electrode components in g/mL

	PI	**Super-P**	**MAG-E**
Density (g/mL)	1.43	2.00	2.26

In a previous study, it has been shown that the volume expansion of alloy electrodes is mainly related to the expansion of alloy particles with small change in electrode porosity [45]. To calculate the initial porosity, the solid volume of each electrode component was first determined using the density listed in Table 5.2 and Table 5.4. The electrode pore volume equaled to the difference of the total coating volume minus the solids volume. Initial porosity is expressed as the proportion of pore volume to

the total coating volume. To calculate the final porosity, it was first assumed that carbon has a volume expansion of 10% when full lithiated and a capacity of 600 mAh/g [102]. Then the volume expansion of silicon was calculated by assuming the molar volume of Li in Li-Si after full lithiation is 9mL/(mol Li) [108]. The volume change caused by the lithiation of carbon and silicon plus the initial solid volume gave the final solid volume. Similarly, the final porosity is expressed as the proportion of the final pore volume to the total coating volume. Different from the previous study [45], the porosity of some delithiated C-Si electrodes reduced greatly. The $C_{80}Si_{20}$, $C_{70}Si_{30}$, and $C_{50}Si_{50}$ electrodes have porosity reduction of >10%, and the $C_{90}Si_{10}$ electrode has a porosity reduction of >20%. Here, the reduction of porosity indicates that porosity within the C-Si particles can accommodate alloy volume expansion. This may account for the stable cycling performance of these alloys.

A model has been proposed to illustrate the structure transitions of C-Li-Si alloys during ethanol delithiation and of C-Si alloys during lithiation/delithiation, as shown in Figure 5.11. After milling, evenly distributed C-Li-Si alloys are formed, composed of Li-Si compounds and amorphous C. Since ball milled amorphous Si is known to store Li at voltages up to 3 V vs Li, which is higher than the potential of Li in Si alloys, the amorphous carbon phase likely contains lithium. After reacting with ethanol overnight, Li is extracted from C-Li-Si alloys, leaving hollows where Si particles reside. When C-Si alloys are cycled as electrodes, Si converts into Li-Si phases during lithiation, resulting in

the volume expansion of Si. The Li-Si phase converts back into Si during delithiation, resulting in the volume contraction of Li-Si. During the contraction process, some Si particles remain in contact with the C matrix while other Si particles are isolated. The isolated Si particles cannot be lithiated again, resulting in capacity loss. C is also lithiated/delithiated but its volume expansion is very low (not shown in Figure 5.11).

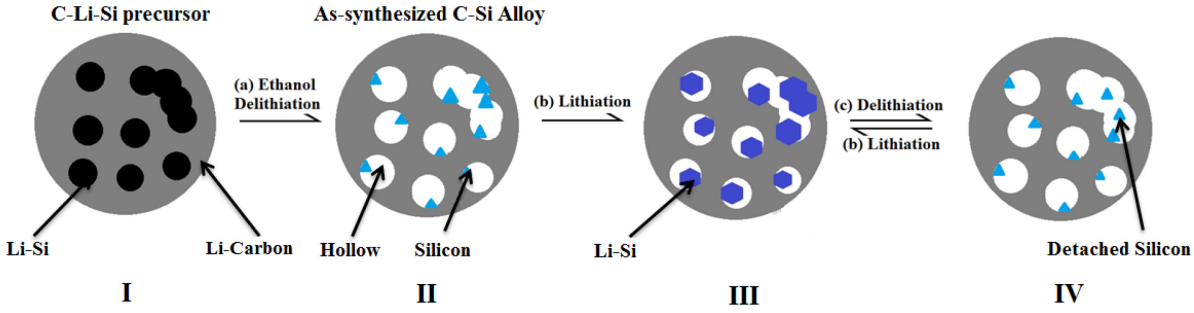

Figure 5.11 Possible structure transitions of C-Li-Si during (a) ethanol delithiation and structure transitions of C-Si alloys during (b) lithiation and (c) delithiation.

When the Si content is low ($C_{90}Si_{10}$, $C_{80}Si_{20}$, and $C_{70}Si_{30}$), C matrix works effectively to diminish the volume expansion of Si, and thus the whole volume expansion of C-Si electrode is low. However, if the Si content becomes higher ($C_{60}Si_{40}$, $C_{50}Si_{50}$, and $C_{40}Si_{60}$), there is not enough room for "hollows" to form in the C matrix. Thus, the whole C-Si electrode volume expansion is high. This model can also help to understand why the porosity reduction of some C-Si electrodes was so large. The calculated porosity includes the space between different particles (C-Si, PI and carbon black particles) and hollows (within C-Si particles). After lithiation, the proportion of the space between particles to the whole volume might not change so much, according to the previous study

[45], but the proportion of hollows became smaller, as shown in Figure 5.12. Therefore the calculated porosity of C-Si electrodes reduced greatly after lithiation.

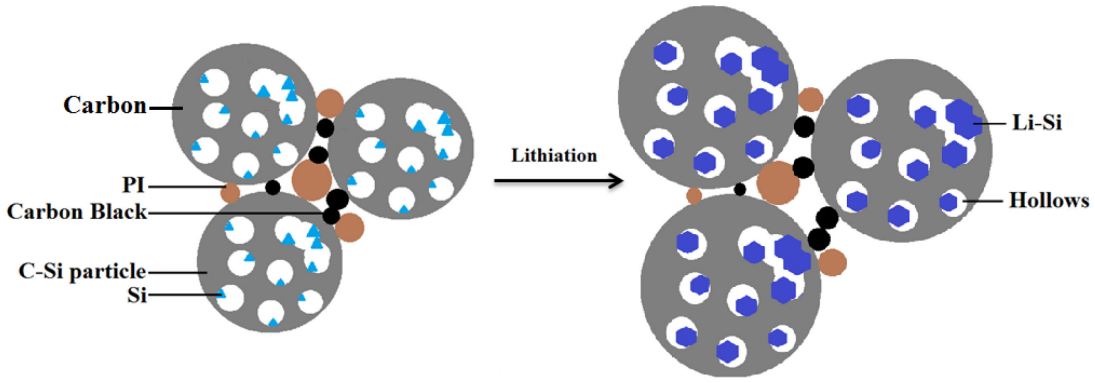

Figure 5.12 Possible structure transitions of C-Si electrodes after one full lithiation.

5.4 CONCLUSION

In this chapter, bulk quantities of C-Si alloys were prepared by ethanol delithiation of C-Li-Si precursors with serial C:Si stoichiometric ratios. XRD, SEM and electrochemical measurements were performed and analyzed. C-Si electrodes exhibited lower volume expansion (as low as 21%) compare to that of bulk cr-Si. This might account from the carbon matrix working as a "diluent" and the hollows formed within C-Si alloys accommodating the volume expansion of the Si phase. C-Si alloys also exhibited superior cycling performance than that of bulk cr-Si. After 50 cycles at C/5 rate, the capacity of cells with C-Si electrodes remained as high as 1800mAh/g. The differential capacity curves show that no transition occurs between crystalline $Li_{15}Si_4$ and amorphous lithiated silicon when the voltage is below 0.05 V.

The chemical delithiation method applied in this chapter represents an effective means of producing C-Si alloys with low volume expansion, good cycling performance and high capacity.

CHAPTER 6 METAL-SILICON ALLOYS PREPARED BY DELITHIATION

6.1 INTRODUCTION

As discussed in Chapter 2, combining active material (Si) with an inactive one is a method to diminish the volume expansion problem of Si [47]. The principles for designing active / inactive alloys have been discussed in Reference 99. Essentially, the volume expansion of the active part is diluted by the inactive matrix during lithiation, so that the whole negative electrode can experience lower volume expansion and therefore achieve improved cycle life [75].

Among all the active / inactive systems, the iron-silicon (Fe-Si) system has been broadly studied as negative electrodes in Li cells [76-81]. Fe-Si alloys have been prepared by ball milling in a number of previous studies [76-79, 81]. By using ball milling, researchers typically focused on how the composition and microstructure of alloys can affect their cycling performance. According to Fe-Si binary phase diagram shown in Figure 6.1, Fe and Si can form a number of different phases. $FeSi_2$ and FeSi have been identified as inactive phases in ball milled Fe-Si alloys, which have been suggested to dilute volume expansion and, as a result, improve cycling performance [76-78, 81]. Another way to prepare Fe-Si alloy is sputtering. Fleischauer *et al*. prepared Fe-Si films containing a-Si and Si_xFe_{1-x} ($0.5<x<1$) by sputtering as negative electrodes for Li-ion cells [80]. It was observed that the capacity of these Fe-Si alloys was almost linearly dependent on the Si content. Other Si-based active / inactive alloys have also

been studied as negative electrodes for Li-ion batteries, such as Cu-Si [82, 109, 110] and Ni-Si [83, 111], *etc*. These materials exhibited improved cycling performance compared to that of bulk cr-Si [82, 83, 109-111]. According to the Ni-Si and Cu-Si phase diagrams in Figure 6.2 and 6.3, Ni and Cu can form a number of binary phases with Si. Cu_3Si and Cu_5Si were detected from Cu-Si alloys in previous studies [82, 109, 110]. NiSi and $NiSi_2$ were detected from Ni-Si alloys in previous studies [111].

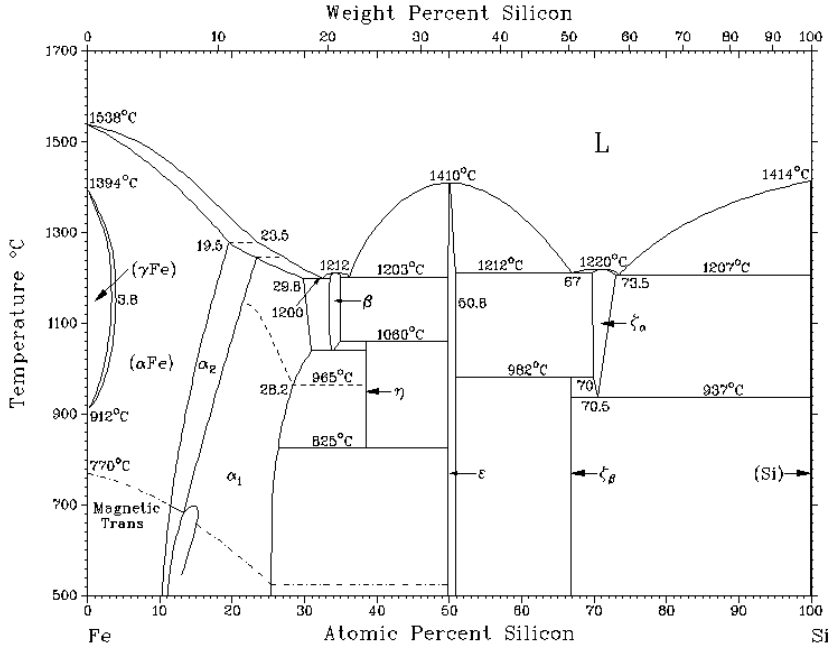

Figure 6.1 Fe-Si binary phase diagram [112].

Anani *et al.* has reported that Li ternary silicides (Li-Metal-Si) have a more favorable voltage profile and a higher reversible capacity than Li-Si binary alloys based on thermodynamic calculations [84, 85]. However, the preparation of negative electrodes for Li cells via the delithiation of Li- Metal-Si ternary compounds has not been reported. Li, Si and Ni or Cu can also form ternary compounds ($LiNi_2Si$ and $LiCu_2Si$,

respectively). It might be interesting to investigate if chemical delithiation is an effective method to prepared negative electrodes for Li cells from Li ternary silicides.

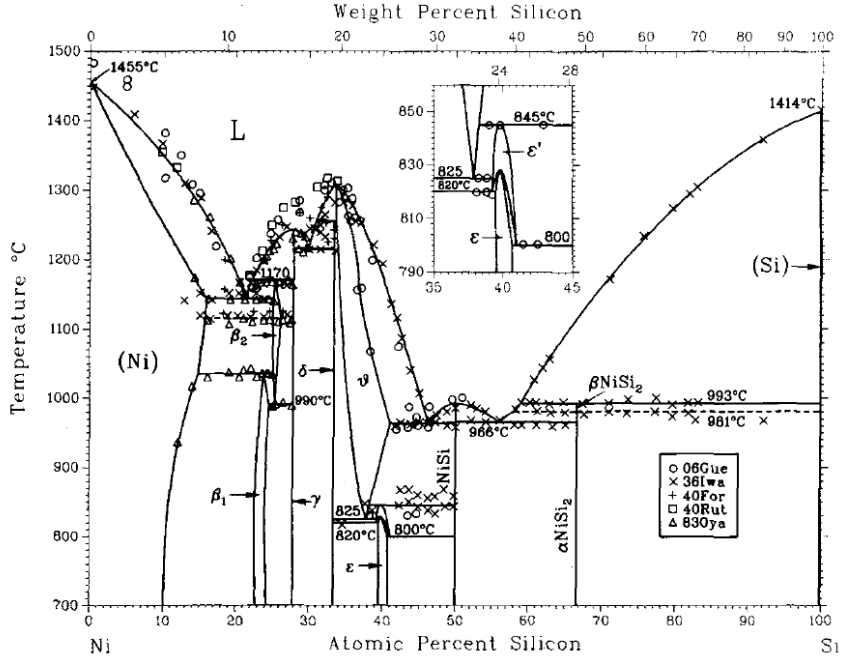

Figure 6.2 Ni-Si binary phase diagram [113].

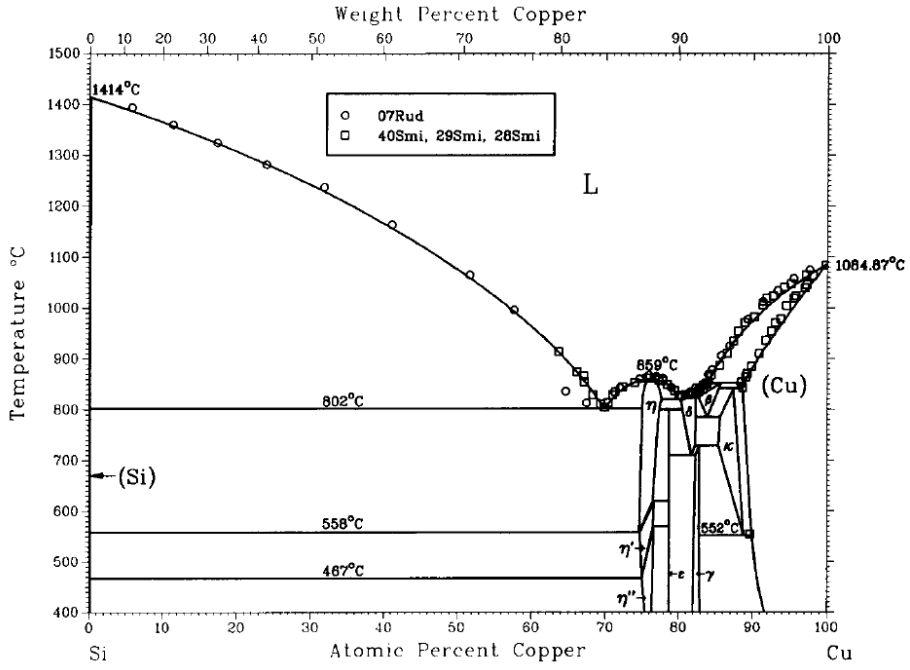

Figure 6.3 Cu-Si binary phase diagram [114].

In this chapter, Fe-Li-Si alloys were first synthesized by ball milling. The Fe-Si alloys were then prepared by the delithiation of Fe-Li-Si with ethanol using the method introduced in Chapter 4. XRD, SEM, Mössbauer spectra and electrochemical measurements of Fe-Si alloys were performed and analyzed.

Besides, Cu-Si and Ni-Si alloys were prepared and studied. Li-Ni-Si and Cu-Li-Si alloys were first synthesized by ball milling Li-Si with Ni or Cu powder. The Ni-Si and Cu-Si alloys were then prepared by delithiation of Li-Ni-Si or Cu-Li-Si precursors with ethanol using the method introduced in Chapter 4. XRD and electrochemical measurements of Ni-Si and Cu-Si alloys were performed and analyzed.

6.2 EXPERIMENTAL

Synthesis of Fe-Si alloys

The $Li_{12}Si_7$ compounds were prepared using an arc furnace. About 1.2 g lithium (99.90% Li ribbon, Sigma) and silicon (98.40% Si lump, Alfa Aesar) were melted under an Ar-flow with a 7% excess of lithium to offset Li loss from vaporization. After cooling down, the resulting $Li_{12}Si_7$ chunk was ground into powder with a pestle and mortar in an Ar-filled glove box.

The Fe-Li-Si precursors were prepared by milling Fe powder (-325 mesh, 99.9+%, Aldrich) and $Li_{12}Si_7$ powder with 115 g of 3/16" stainless steel balls under an Ar atmosphere for 2 hours in a 65 mL hardened steel vial using a SPEX mill (Model 8000-D, Spex Certiprip, Metuchen, M.J.). Here, the mass of Fe and $Li_{12}Si_7$ powder to prepare Fe-Li-Si alloys are listed in Table 6.1.

Table 6.1 Mass of Fe and $Li_{12}Si_7$ powder for the preparation of Fe-Li-Si alloys.

Fe:Si in Stoich. Ratio	**Fe:Si in Volume Ratio**	**Fe (g)**	**$Li_{12}Si_7$ (g)**
80:20	70:30	4.1020	0.7419
72:28	60:40	3.2411	0.9119
63:37	50:50	2.5051	1.0572
53:47	40:60	1.8686	1.1829
42:58	30:70	1.3127	1.2926

The as-prepared Fe-Li-Si precursors were added (2~3 g) into a 3-neck flask with a magnetic stirrer in an Ar-filled glovebox. The flask was then set in fumehood with an Ar-flow introduced and exhausted through an oil bubbler to maintain an inert atmosphere. Then 120 mL of ethanol (99.89%, containing 0.10% H_2O, Commercial Alcohols) was added to the flask and the mixture was stirred continuously overnight. The whole delithiation process was conducted at room temperature.

After overnight reaction, the resulting black product was washed using a Büchner funnel (with 44.25 mm filter paper, Whatman) with distilled water repeatedly until the pH of the washing water was ~7. The product was then heated in a tube furnace at 120 °C for 3 hours under an Ar-flow.

Synthesis of Ni-Si and Cu-Si alloys

$Li_{12}Si_7$ or LiSi precursors were synthesized in Li:Si stoichiometric ratios of 12:7 or 1:1 using an arc furnace with 7% of excess Li to offset Li loss from vaporization. The

resulting Li-Si precursors were ground into powder with a pestle and mortar in an Ar-filled glove box. Li-Ni-Si and Cu-Li-Si precursors were then prepared by ball milling either $Li_{12}Si_7$ (Method 1) or LiSi (Method 2) with Ni or Cu powder (both Ni and Cu powder were 325 mesh, 99.9+%, Aldrich) with 115 g of 3/16" stainless steel balls under an Ar atmosphere for 2 hours in a 65 mL hardened steel vial using a SPEX mill. Table 6.2 listed the mass of each component for preparation of Li-Ni-Si and Cu-Li-Si precursors. Precursors prepared with $Li_{12}Si_7$ were labeled as Ni1 or Cu1, while those prepared with LiSi were labeled as Ni2 or Cu2. The Li-Ni-Si and Cu-Li-Si precursors were delithiated with ethanol using the same method introduced above.

Table 6.2 Mass of LiSi, $Li_{12}Si_7$, Ni and Cu powder for the preparation of Li-Metal-Si alloys.

Sample	**Stoich. Ratio**	**LiSi (g)**	**$Li_{12}Si_7$ (g)**	**Ni (g)**	**Cu (g)**
Ni1	Li:Ni:Si = 12:18:7		0.9338	3.5383	
Cu1	Li:Cu:Si = 12:18:7		0.9066		3.7195
Ni2	Li:Ni:Si = 1:2:1	1.1248		3.7401	
Cu2	Li:Cu:Si = 1:2:1	1.0901			3.9251

Characterization by Microscopy, X-ray Diffraction and Mössbauer Spectroscopy

Particle size and morphology of Fe-Si alloys were studied using with a Phenom G2-pro Scanning Electron Microscope (Nanoscience, Arizona). X-ray diffraction (XRD) patterns of all tested samples were collected with a Rigaku Ultima IV diffractometer

equipped with a copper target X-ray tube, a dual position graphite diffracted beam monochromator and a scintillation counter detector. XRD data was collected between $2\theta = 20° \sim 80°$ (or $20° \sim 60°$) with a step of 0.05° and a 6 second dwell time. Room temperature ^{57}Fe Mössbauer effect spectra of Fe-Si alloys were measured using a See Co. constant acceleration spectrometer equipped with a $Rh^{57}Co$ source. The velocity scale calibration was determined relative to α-Fe at room temperature. Sample density was determined by a helium pycnometer (AccuPyc II 1340, Micrometritics).

Electrochemical Characterization

Electrodes were prepared from a slurry of 62.5 vol.% Fe-Si, Ni-Si or Cu-Si active materials, 18 vol.% carbon black (Super-P, Erachem Europe) and 19.5 vol.% polyimide (PI, PI-2555, HD Microsystems) in N-methyl pyrrolidinone (NMP, 99.50%, Sigma). The slurry was mixed with a planetary ball mill (Retsch PM 200) with four 7/16" tungsten carbide balls at 100 rpm for 1 hour. The resulting slurries were spread on Cu foils (Furukawa Electric, Japan) with a 0.004 inch coating bar and then dried at 120 °C under vacuum overnight. Circular working electrodes (d = 13 mm) were punched from coated foils and heated in a tube furnace at 300 °C under an Ar-flow for 3 hours, in order to cure the PI binder.

Electrodes were transferred into an Ar-filled glove box and assembled in 2325 coin-type cells with a lithium foil as the reference/counter electrode. Two layers of Celgard 2300 separators were used in each coin cell. 1M $LiPF_6$ (BASF) in a solution of monofluoroethylene carbonate (FEC), ethylene carbonate (EC) and diethyl carbonate

(DEC) (volume ratio 1:3:6, all from Novolyte Technologies) was used as electrolyte. All coin cells were charged and discharged at 30.0 ± 0.1 °C between 50 mV ~ 0.9 V using a Maccor Series 4000 Automated Test System at a C/20 rate and trickle discharged to C/40 rate for the 1st cycle, and at a C/5 rate and trickle discharged to a C/20 rate for the following cycles based on the theoretical capacity of the electrode. All coin cells had a rest period of 15 minute at open circuit at the end of each half-cycle. To determine volume expansion, electrodes thickness was measured to within ±1 μm with a Mitutoyo 293-340 precision micrometer in an Ar-filled glove box before assembling cells and after one full lithiation (C/20 constant current, discharged to 0.005 V, C/40 trickle).

6.3 Results and Discussion

Fe-Si alloys

Figure 6.4 shows the Fe-Li-Si ternary system. Red spots represent the compositions of Fe-Li-Si precursors and blue spots represent the compositions of Fe-Si alloys prepared by the delithiation of Fe-Li-Si. Figure 6.5(a-e) show the XRD patterns of Fe-Li-Si alloys after milling Fe and $Li_{12}Si_7$ powder, corresponding to red dots (a-e) in Figure 6.4. Two sharp peaks were observed at 45 and 65 degrees in each of Figure 6.5(a-e). These peaks correspond to Fe metal. There was also a narrow peak near 50 degrees as shown in Figure 6.5(e), which was identified as FeSi. No FeSi peaks were observed in Figure 6.5(a-d) and no $FeSi_2$ peaks were observed in each of Figure 6.5(a-e), which is different from previous studies [76-79, 82]. No Li-Si compound peaks were observed in Figure 6.5(a-e), indicating that Li-Si compound might have become amorphous.

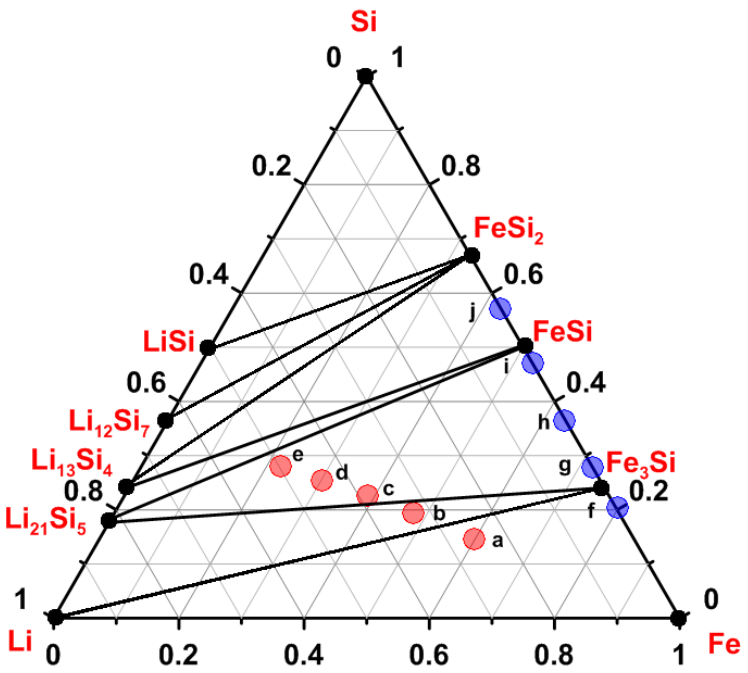

Figure 6.4 The Fe-Li-Si ternary system at 0 K as predicted by the Materials Project [103, 104]. Red dots (a-e) represent the compositions of Fe-Li-Si alloys synthesized by ball milling in Fe:Si stoichiometric ratios of 80:20, 72:28, 63:37, 53:47, and 42: 58, respectively and blue dots (f-j) represent corresponding Fe-Si alloy compositions after the delithiation.

Bulk quantities of Fe-Si powders were prepared by delithiation of Fe-Li-Si alloys with ethanol under an inert atmosphere, presumably according to the reaction below:

$$LiSi_xFe_y\ (s) + R\text{-}OH\ (l) \rightarrow R\text{-}OLi\ (s) + \tfrac{1}{2}\ H_2\ (g) + Si_xFe_y\ (s). \qquad (6.1)$$

The alkoxide products (R-OLi) were insoluble in ethanol, and were subsequently washed away by rinsing with distilled water. The resulting Fe-Si alloys were produced in an average yield of 70 % by weight.

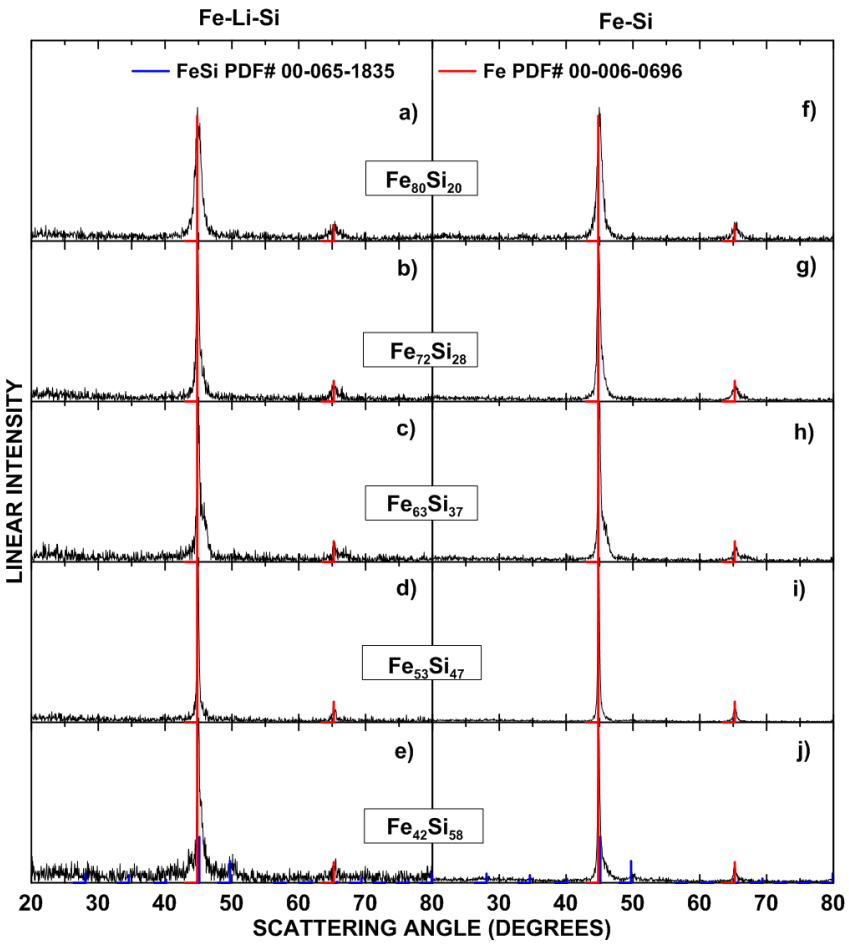

Figure 6.5 XRD patterns of (a-e) Fe-Li-Si alloys and (f-j) Fe-Si alloys in Fe:Si stoichiometric ratios of 80:20, 72:28, 63:37, 53:47, and 42:58.

Figure 6.5(f-j) show the XRD patterns of Fe-Si alloys in different Fe:Si stoichiometric ratios, corresponding to blue dots (f-j) in Figure 6.4. The XRD patterns of the Fe-Si alloys are similar to that of their corresponding Fe-Li-Si precursors. Two sharps peaks (at 45 and 65 degrees) are indicative of Fe phase in Figure 6.5(f-j). No broad a-Si peaks were observed near 29 and 51 degrees, possibly because the intensity of a-Si peaks was too weak compared to that of Fe. The FeSi peaks also appear in Figure 6.5(j). In contrast, no FeSi or $FeSi_2$ peaks were observed in Figure 6.5(f-i).

Figure 6.6 shows the Mössbauer spectra of the Fe-Si alloys. All spectra were fit using a combination of two distinct Fe sites. The hyperfine parameters obtained from the analysis of spectra are listed in Table 6.3, including center shifts (δ), magnetic fields (H), quadrupole splitting (Δ), half width at half maximum (HWHM), and site populations (Area). There are one sextet and one doublet components with center shifts near 0 mm/s and +0.25 mm/s, respectively, in the Mössbauer spectra of all Fe-Si samples. The magnetically split sextet in all spectra shows a hyperfine field of ~33.0 T and a center shift near 0 mm/s, indicative of α-Fe phase in the Fe-Si alloys [115-118].

Table 6.3 Mössbauer parameters of the Fe-Si alloys. Center shifts (δ), internal magnetic fields (H), HWHM, quadrupole splittings (Δ) and site populations (Area) for the sextet and doublet components. Typical uncertainties are ±0.005 mm/s for all velocities, ±0.1 T for hyperfine fields and ±5% for site populations.

	Sextet				**Doublet**		
Sample	**δ (mm/s)**	**H (T)**	**HWHM (mm/s)**	**Area (%)**	**δ1 (mm/s)**	**Δ1 (mm/s)**	**Area (%)**
$Fe_{80}Si_{20}$	0.003	34	0.195	90.3±4.5	0.264	0.492	9.7±0.5
$Fe_{72}Si_{28}$	0.003	32	0.155	89.4±4.5	0.268	0.495	10.6±0.5
$Fe_{63}Si_{37}$	0.003	32	0.154	84.9±4.2	0.248	0.503	13.1±0.7
$Fe_{53}Si_{47}$	0.004	33	0.145	79.0±4.0	0.253	0.496	21.0±1.1
$Fe_{42}Si_{58}$	0.004	33	0.148	71.6±3.6	0.247	0.485	28.4±1.4

As shown in Table 6.3, the hyperfine field (H) is almost the same for all samples, indicative of similar Fe-Fe ferromagnetic coupling. The doublet can be associated with the FeSi phase [115-118]. Similar hyperfine parameters for FeSi and α-$FeSi_2$ make it difficult to distinct these two phases on the basis of Mössbauer measurements alone [115-117], but the XRD pattern shown in Figure 6.5(j) indicates the presence of a FeSi phase in the $Fe_{42}Si_{58}$ sample. Desimoni *et al*. has reported the values of +0.28 and 0.50 mm/s for the center shift and quadrupole splitting, respectively, for FeSi phase [116]. McGraw *et al*. also reported that the center shift had a value of +0.26 mm/s and the quadrupole splitting had a value of 0.55 mm/s in a sputtered $Si_{100-x}Fe_x$ sample when x approaches 50 [117]. Dézsi *et al*. reported that the center shift had a value of +0.28 mm/s and the quadrupole splitting had a value of 0.49 mm/s for FeSi phase [118]. These values in previous studies are similar to those reported in Table 6.3, indicating the appearance of FeSi phase in the as-prepared Fe-Si alloys. Although most XRD patterns of Fe-Si alloys show no FeSi peaks except that of $Fe_{42}Si_{58}$ in Figure 6.5, the Mössbauer spectra suggest that all Fe-Si alloys are composed of Fe and FeSi. The relative intensity of the doublet component increases gradually as the Si content increases, indicating that Fe-Si alloys containing more Si also contain more FeSi.

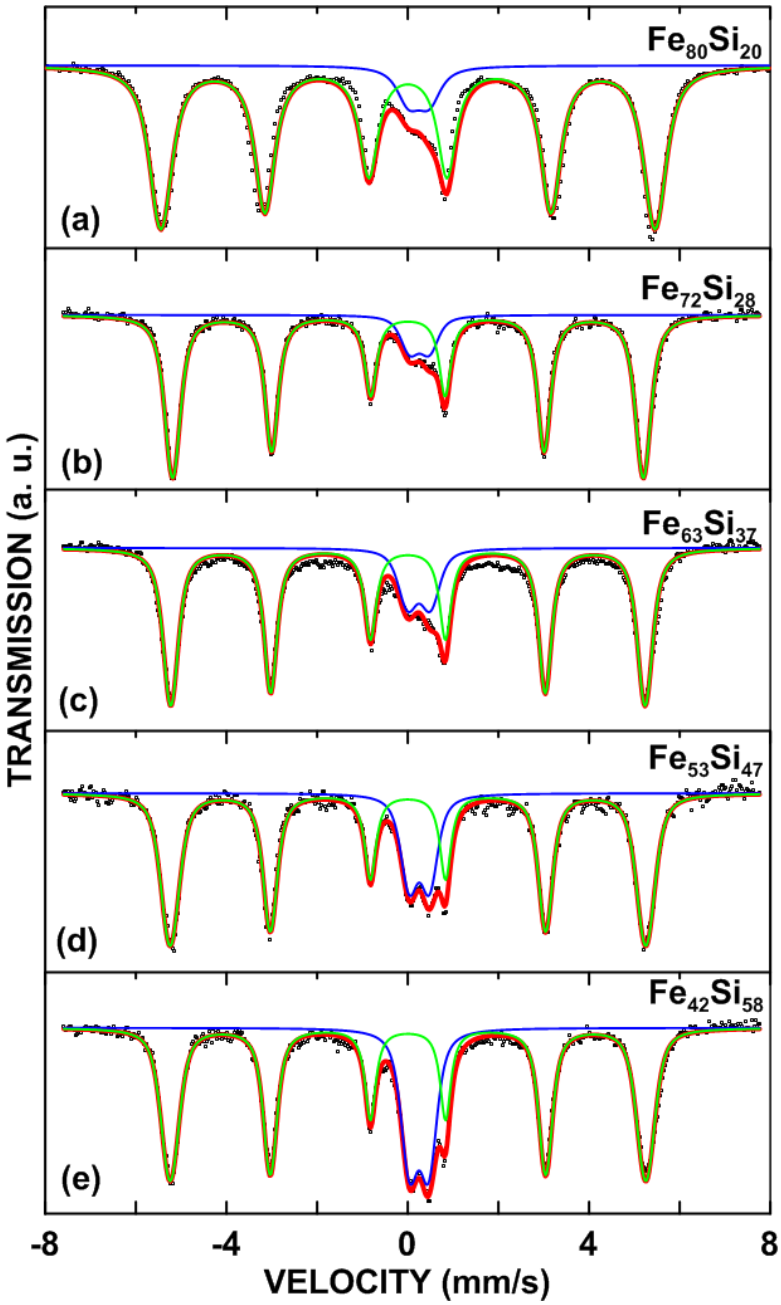

Figure 6.6 Room temperature ^{57}Fe Mössbauer effect spectra of the Fe-Si alloys. The velocity scale is measured relative to room temperature α-Fe. The black dots represent the initial data. The red solid lines through the data represent the total fit. The green lines represent the sextet components and the blue lines represent the doublet components.

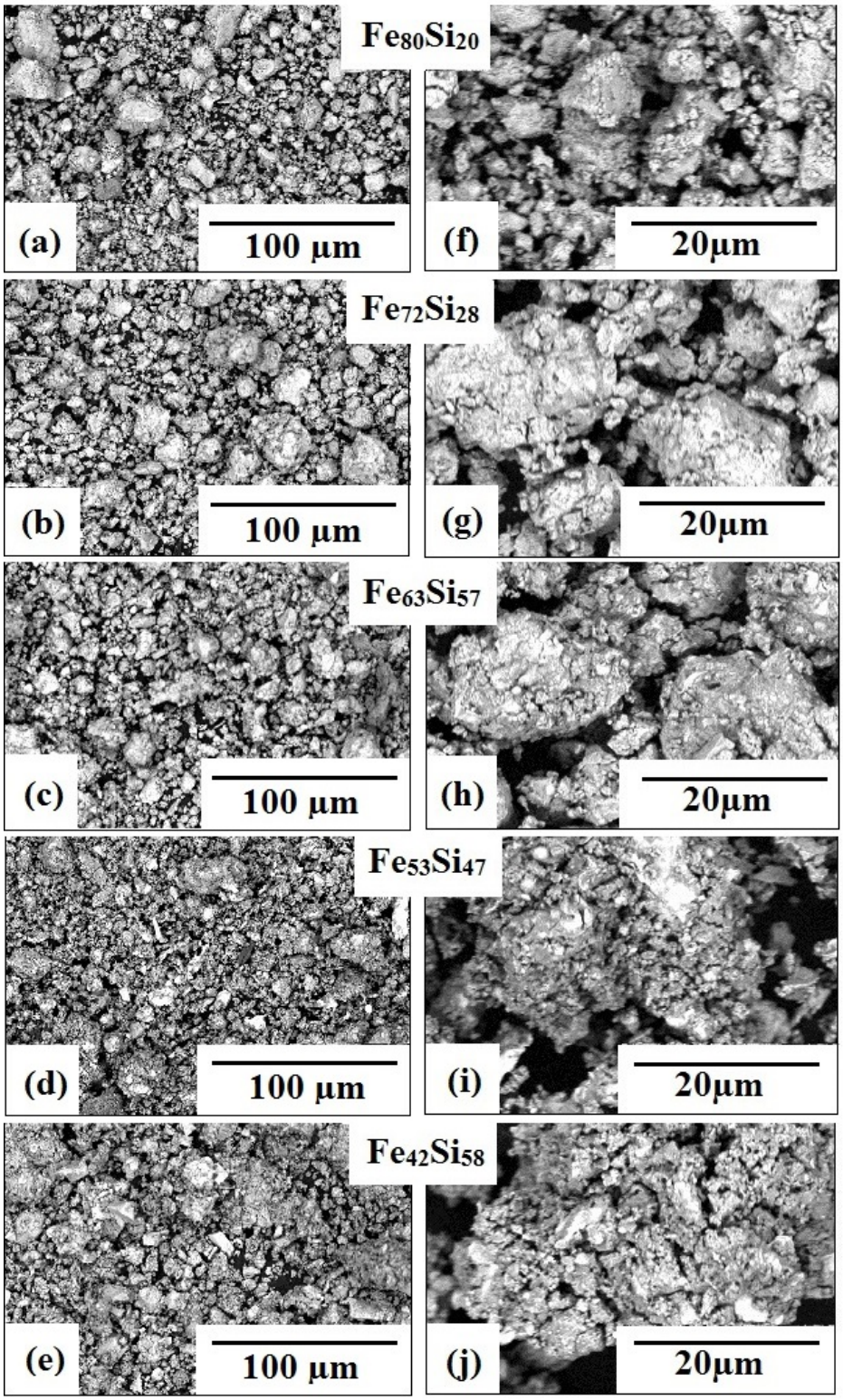

Figure 6.7 SEM images of Fe-Si alloys (labeled in stoichiometric ratios of Fe:Si = 80:20, 72:28, 63:37, 53:47, and 42:58) at different magnifications.

The morphology and particle size of Fe-Si powders were characterized by SEM. Figure 6.7 shows the SEM images of the Fe-Si alloys in serial Fe:Si stoichiometric ratios at different magnifications. The overall particle size of all samples ranges from 2 to 50 μm. Most particles range from 10 to 30 μm in size. No obvious difference in particle size can be observed among different Fe-Si alloys. Different Fe:Si ratios seem not to influence particle size. In Figure 6.7(f-h), fine primary particles combine together to form large secondary particles. In Figure 6.7(i-j), it seems that the large secondary particles are porous. This porosity formed presumably due to the extraction of Li. There is no layered structure (as observed in a-Si prepared with ethanol) observed in Figure 6.7.

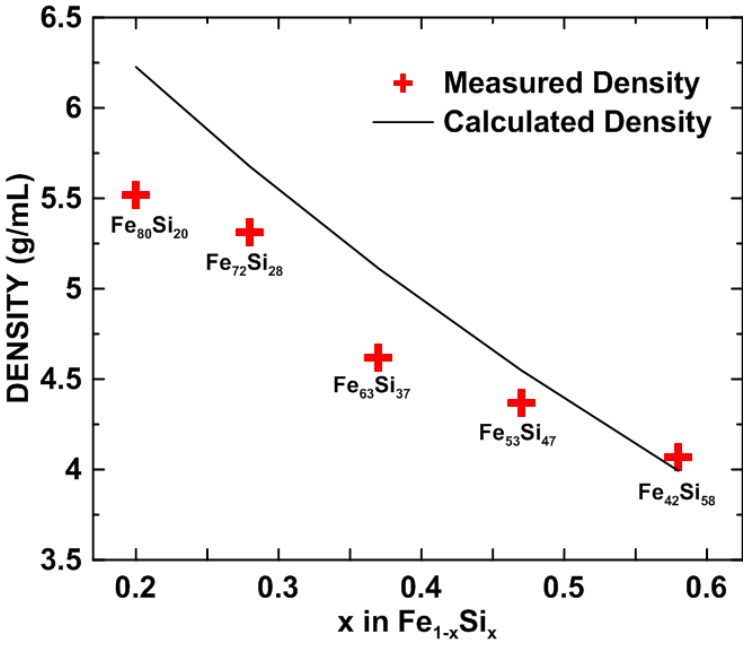

Figure 6.8 Density of Fe-Si alloys measured by a helium Pycnometer (AccuPyc II 1340, Micrometritics. Red spots represent the measured density and the black solid line represents the calculated density.

The density of all Fe-Si alloys ranges between that of Fe (7.87 g/mL) and Si (2.33 g/mL). The density of Fe-Si alloys decreases as the silicon content increases, as shown in Figure 6.8. The black solid line in Figure 6.8 represents the calculated density based on the Fe powder density of 7.87 g/mL and the Si powder density of 2.33 g/mL. Densities of most Fe-Si alloys ($Fe_{80}Si_{20}$, $Fe_{72}Si_{28,}$ $Fe_{63}Si_{37}$, and $Fe_{53}Si_{47}$) are less than calculated values. This might due to (1) the loss of Fe during delithiation reaction and (2) the formation of porosity within the secondary Fe-Si particles that is inaccessible to He gas. However, the density of $Fe_{42}Si_{58}$ is close to the calculated value. This might result from a greater porosity and therefore a greater connectivity of pores in this sample.

Figure 6.9 shows the voltage curves and differential capacity curves of Fe-Si electrodes in Li cells. $Fe_{80}Si_{20}$ electrode has almost no capacity, as shown in Figure 6.9(a) and its differential capacity curve has no characteristic peak in Figure 6.9(f). The voltage curve (Figure 6.9(b)) of $Fe_{72}Si_{28}$ electrode has two sloping plateaus during lithiation and delithiation, indicative of typical single-phase regions of a-Si lithiation and a-Li_xSi delithiation [31]. These sloping plateaus correspond to broad peaks in Figure 6.9(g). Previous studies have found that the formation of cr-$Li_{15}Si_4$ was suppressed by using nano-structured (active Si) / inactive alloys, leading to improved cycling [45, 75]. It was speculated that the matrix phase in (active Si) / inactive alloys may suppress cr-$Li_{15}Si_4$ formation via the generation of high mechanical stresses during volume expansion [9]. However, the voltage curves of $Fe_{63}Si_{37}$, $Fe_{53}Si_{47}$, and $Fe_{42}Si_{58}$ electrodes have a well-defined plateau during delithiation in Figure 6.9(c-e), indicative of a two-phase

region, corresponding to cr-$Li_{15}Si_4$/a-Li_xSi [31]. As shown in Figure 6.9(h-j), the peak near 0.44 V during delithiation becomes sharper as the Si content increases, suggesting that high Si content may lead to the formation of cr-$Li_{15}Si_4$. A short narrow peak can also be observed in Figure 6.9(i-j) near 0.01 V during lithiation, indicating the formation of cr-$Li_{15}Si_4$. Therefore, the formation of the cr-$Li_{15}Si_4$ during lithiation is likely avoided in Fe-Si electrodes containing small amount of Si (*i.e.* $Fe_{80}Si_{20}$ and $Fe_{72}Si_{28}$ electrodes). As the Si content increases, cr-$Li_{15}Si_4$ formation cannot be effectively suppressed (*i.e.* $Fe_{63}Si_{37}$, $Fe_{53}Si_{47}$, and $Fe_{42}Si_{58}$ electrodes).

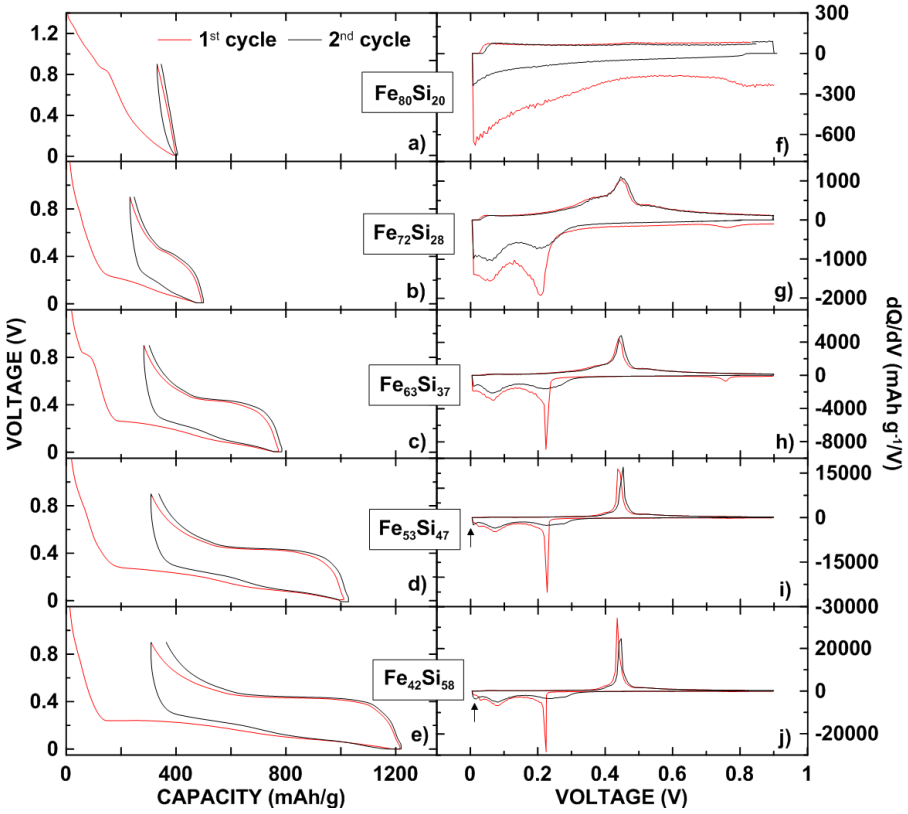

Figure 6.9 (a-e) Voltage curves of Fe-Si electrodes and (f-j) differential capacity curves of Fe-Si electrodes. The peaks in (i-j) labeled by arrows might indicate the formation of cr-$Li_{15}Si_4$.

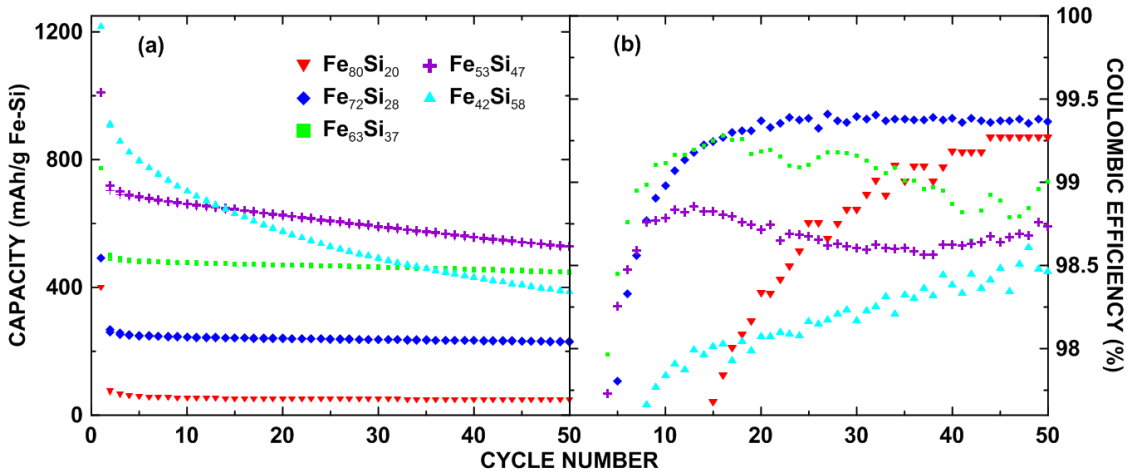

Figure 6.10 (a) Cycling performance and (b) coulombic efficiency (CE) of Fe-Si electrodes.

Table 6.4 Cycling performance of Fe-Si electrodes. Here, RC = the 1st cycle reversible capacity, IC = the 1st cycle irreversible capacity percentage, 50th Capacity = specific capacity after 50 cycles, Retention = 50th Capacity/RC, initial and final porosity was obtained by calculating.

Active Material	**RC (mAh/g)**	**IC (%)**	**50th Capacity (mAh/g)**	**Retention (%)**	**Volume Expansion (%)**	**Initial Porosity (%)**	**Final Porosity (%)**	**Porosity Reduction (%)**
$Fe_{80}Si_{20}$	68±1	83±1	47±1	70	5±2	84±1	78±1	7.1±1
$Fe_{72}Si_{28}$	261±3	47±1	230±2	88	50±2	84±2	80±2	4.8±1
$Fe_{63}Si_{37}$	489±4	37±2	447±5	91	84±3	74±1	70±1	5.4±1
$Fe_{53}Si_{47}$	702±9	31±3	527±7	75	111±12	86±2	81±2	5.8±4
$Fe_{42}Si_{58}$	906±13	25±5	388±11	43	128±13	82±1	80±1	2.4±2

Figure 6.10 and Table 6.4 show the cycling performance of Fe-Si electrodes in Li cells. The only active component in Fe-Si alloys is Si. Fe-Si alloys composed of more Si displayed higher reversible capacity. When the Si content was low ($Fe_{80}Si_{20}$, $Fe_{72}Si_{28}$, and $Fe_{63}Si_{37}$), the cycling performance was quite stable. However, the $Fe_{80}Si_{20}$ electrode displayed very low capacity (only 47 mAh/g at the 50^{th} cycle). The $Fe_{72}Si_{28}$ and $Fe_{63}Si_{37}$ electrodes displayed higher capability (230 mAh/g and 447 mAh/g, respectively) after 50 cycles than that of $Fe_{80}Si_{20}$ electrode. Although $Fe_{53}Si_{47}$ and $Fe_{42}Si_{58}$ electrodes exhibited smaller irreversible capacity (31% and 25%, respectively), they had worse cycling stability. After 50 cycles, $Fe_{42}Si_{58}$ electrode even had lower capacity than that of $Fe_{63}Si_{37}$ electrode. Here, the low capacity of Fe-Si electrodes might be due to the formation of FeSi compounds. The poor cycling stability of $Fe_{53}Si_{47}$ and $Fe_{42}Si_{58}$ electrodes might be due to mechanical failure, of which $Li_{15}Si_4$ formation may be a symptom. Figure 6.10(b) shows the coulombic efficiency (CE) of Fe-Si electrodes. After 40 cycles, electrode containing more Si had lower CE ($Fe_{80}Si_{20} \sim Fe_{72}Si_{28} > Fe_{63}Si_{37} > Fe_{53}Si_{47} > Fe_{42}Si_{58}$). All Fe-Si electrodes had low coulombic efficiency.

Figure 6.11 shows the calculated and measured capacities of Fe-Si electrodes. Similar to previous studies, it was observed that the measured capacities of Fe-Si electrodes were almost linearly dependent on the Si content [80]. The blue line was calculated based on (1) the theoretical capacity of Si (3579 mAh/g) and (2) the assumption that Fe and Si did not react. Most measured capacities were 50~60% of the calculated values of the blue line except that of $Fe_{80}Si_{20}$ electrode (only 17%). Those low

values arise from the formation of FeSi during ball milling (confirmed by the Mössbauer spectra in Figure 6.6).

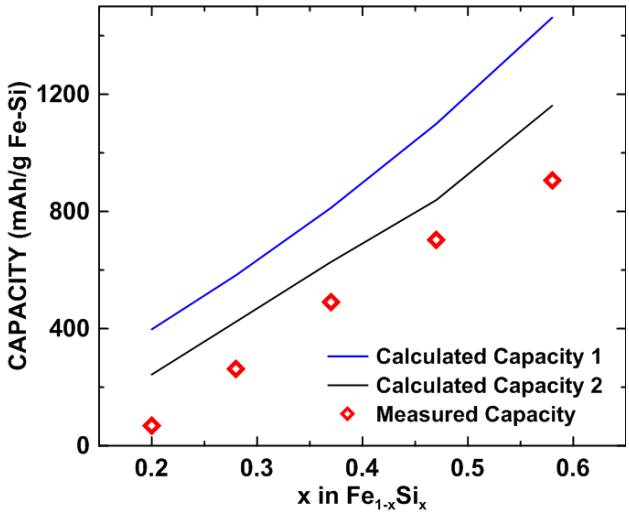

Figure 6.11 Calculated and measured reversible capacities of Fe-Si electrodes *vs*. x in $Fe_{1-x}Si_x$. The blue solid line represents the calculated capacity without considering the FeSi formation. The black solid line represents the calculated capacity when the FeSi formation was taken into account. The FeSi content was estimated based on the Mössbauer spectra of Fe-Si alloys.

The content of FeSi compound was then estimated according to relative intensities of Fe and FeSi components of the Mössbauer spectra, as shown in Table 6.5. The black solid line in Figure 6.11 was calculated considering the FeSi formation. Here, the FeSi content was calculated based on the values from Mössbauer spectroscopy, listed in Table 6.5. The calculated capacities of the black line are still more than the measured values. Therefore, it is speculated that besides FeSi formation during ball milling, the

low capacity of Fe-Si electrodes might arise from dissolution of Si during chemical delithiation, isolation of some Si particles during chemical delithiation or formation of Si-O phases during chemical delithiation.

Table 6.5 The estimated FeSi/(FeSi+Fe) in Fe-Si alloys by Fe atomic percent calculated based on the site populations of Mössbauer spectra of Fe-Si alloys. The typical uncertainty is ±5% for site populations.

	FeSi/(Fe + FeSi) (Fe at.%)
$Fe_{80}Si_{20}$	10
$Fe_{72}Si_{28}$	11
$Fe_{63}Si_{37}$	13
$Fe_{53}Si_{47}$	21
$Fe_{42}Si_{58}$	28

To investigate the volume expansion of Fe-Si alloys, electrode thickness was measured before and after one full lithiation. As shown in Table 6.4, higher silicon content leads to larger volume expansion of the Fe-Si electrodes. The $Fe_{80}Si_{20}$ electrode only has 5% volume expansion. This is consistent to its low active Si content and low capacity. The $Fe_{72}Si_{28}$ and $Fe_{63}Si_{37}$ electrodes also have low volume expansion (50% and 84%, respectively), corresponding to their stable cycling performance. As the Si content increases ($Fe_{53}Si_{47}$ and $Fe_{42}Si_{58}$), the volume expansion increases to values above 100%

(similar to that of a-Si delithiated from $Li_{12}Si_7$ with ethanol). Correspondingly, $Fe_{53}Si_{47}$ and $Fe_{42}Si_{58}$ electrodes exhibited poor cycling stability.

Table 6.6 Density of electrode components in g/mL.

	$Fe_{80}Si_{20}$	**$Fe_{72}Si_{28}$**	**$Fe_{63}Si_{37}$**	**$Fe_{53}Si_{47}$**	**$Fe_{42}Si_{58}$**	**PI**	**Super-P**	**MAG-E**
Density	5.5169 ±0.0060	5.3133 ±0.0071	4.623 ±0.0089	4.3732 ±0.0027	4.0758 ±0.0166	1.43	2.00	2.26

A previous study has shown that the volume expansion of alloy electrodes is mainly related to the expansion of alloy particles with slight change in electrode porosity [45]. However, it was found that the porosity of some C-Si electrodes reduced greatly after one full lithiation in Chapter 5. In this chapter, the porosity of Fe-Si electrodes was also obtained and analyzed. To calculate the initial porosity, the solids volume of each electrode component was first determined using the density listed in Table 6.6. The electrode pore volume equaled to the difference of the total coating volume minus the solids volume. Initial porosity was expressed as the proportion of pore volume to the total coating volume. Then the volume expansion of Si was calculated by assuming the molar volume of Li in Li-Si after full lithiation is 9mL/(mol Li) [107]. The volume change caused by the lithiation of Si plus the initial solid volume gave the final solid volume. Similarly, the final porosity was expressed as the proportion of the final pore volume to the total coating volume. The calculation results are shown in Table 6.4. Different from previous results [45], most Fe-Si electrodes displayed a porosity reduction

of 5~7% except that of the $Fe_{42}Si_{58}$ electrode (2.4%). Here, the reduction of porosity indicates that porosity within the Fe-Si particles can accommodate alloy volume expansion. This may account for the stable cycling performance of some Fe-Si alloys. The poor cycling performance of $Fe_{42}Si_{58}$ electrode might result from its low porosity reduction.

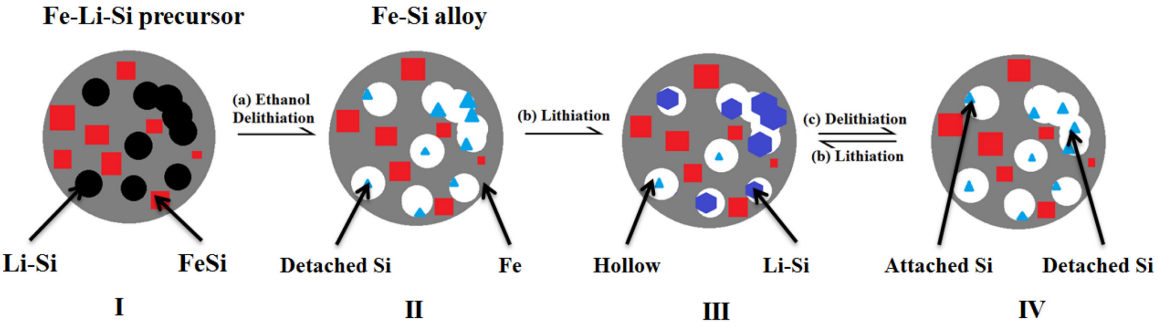

Figure 6.12 Possible structure transitions of Fe-Li-Si after (a) ethanol delithiation and structure transitions of Fe-Si alloys during (b) lithiation and (c) delithiation.

A model was proposed to illustrate the structure transitions of Fe-Li-Si alloys during ethanol delithiation and of Fe-Si alloys during electrochemical lithiation/delithiation, as shown in Figure 6.12. After ball milling, evenly distributed Fe-Li-Si alloys are formed, composed of Fe, Li-Si and FeSi (Figure 6.12(I)). After reacting with ethanol overnight, Li is extracted from Fe-Li-Si alloys, leaving hollows where Si particles reside (Figure 6.12(II)). After chemical delithiation, some Si particles keep attaching to the Fe/FeSi matrix while other Si particles might become disconnected. When Fe-Si alloys are cycled as electrodes, Si converts into Li-Si phases during

lithiation, resulting in the volume expansion of Si (Figure 6.12(III)). The Li-Si phase converts back to Si during delithiation, resulting in the volume contraction of Li-Si (Figure 6.12(IV)). During the contraction process, some Si particles remain in contact with the Fe/FeSi matrix while other Si particles become isolated. The isolated Si particles cannot be lithiated again, resulting in capacity loss. Fe and FeSi are inactive phases, displaying no phase transitions during electrochemical cycling. When the Si content is low ($Fe_{80}Si_{20}$, $Fe_{72}Si_{28}$ and $Fe_{63}Si_{37}$), the Fe/FeSi matrix works effectively to diminish the volume expansion of Si, and thus the whole volume expansion of Fe-Si electrode is low. However, if the Si content is higher ($Fe_{53}Si_{47}$ and $Fe_{42}Si_{58}$), there is not enough room for "hollows" to form in the Fe/FeSi matrix. Thus, the whole Fe-Si electrode volume expansion is high. This model can also help to understand why the porosity of Fe-Si electrodes changed after lithiation. The calculated porosity includes the space between different particles (Fe-Si, PI and carbon black particles) and hollows within Fe-Si particles. After lithiation, the proportion of the space between particles to the whole volume might not change, according to Reference 45, but the proportion of hollows became smaller. Therefore, the calculated porosity of Fe-Si electrodes reduced after lithiation. The porosity reduction of Fe-Si electrodes after lithiation was smaller than that of most C-Si electrodes in Chapter 5.

Ni-Si and Cu-Si alloys

As mentioned in Section 6.2, two types of Li-Si ($Li_{12}Si_7$ and LiSi) were used to prepare Li-Metal-Si as shown in Table 6.2. Li-Metal-Si prepared with $Li_{12}Si_7$ (Method 1)

are labeled as Ni1 and Cu1. Li-Metal-Si prepared with LiSi (Method 2) are labeled as Ni2 and Cu2. Figure 6.13 shows the Li-Ni-Si and Cu-Li-Si ternary system. Red dots represent the compositions of Ni1 and Cu1 and blue dots represent the compositions of their products ($Ni_{72}Si_{28}$ and $Cu_{72}Si_{28}$) after ethanol delithiation. Red stars represent the compositions of Ni2 and Cu2 precursors and blue stars represent the compositions of their possible products ($Ni_{67}Si_{33}$ and $Cu_{67}Si_{33}$) after ethanol delithiation.

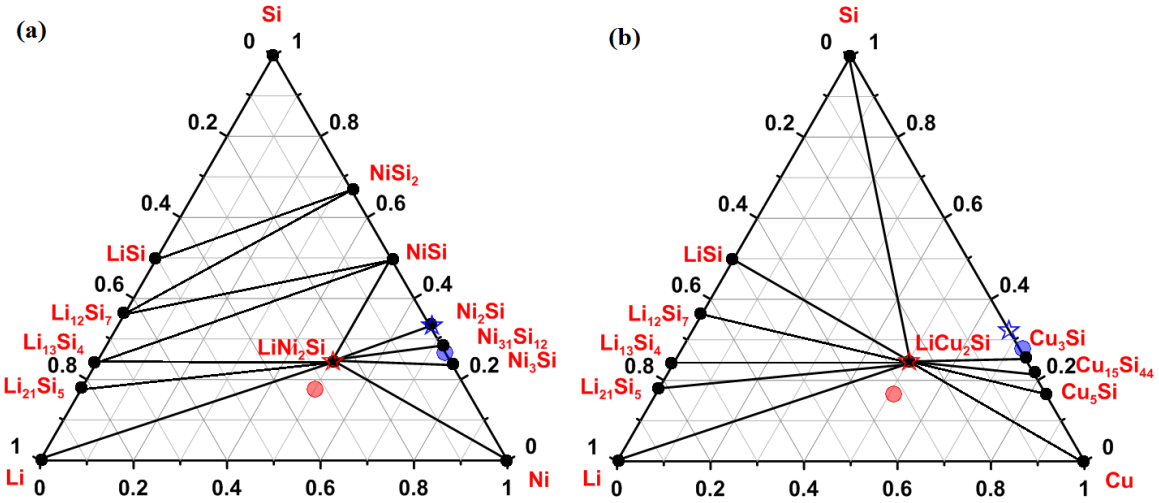

Figure 6.13 The (a) Li-Ni-Si and (b) Cu-Li-Si ternary systems at 0 K as predicted by the Materials Project [103, 104]. Red dots represent the compositions of Ni1 and Cu1 and blue dots represent the compositions of their products ($Ni_{72}Si_{28}$ and $Cu_{72}Si_{28}$) of ethanol delithiation. Red stars represent the compositions of Ni2 and Cu2 and blue stars represent the compositions of their possible products ($Ni_{67}Si_{33}$ and $Cu_{67}Si_{33}$) of ethanol delithiation.

A previous study has shown that when the Si content is high (>75 at.%), NiSi and $NiSi_2$ peaks can be observed in the XRD patterns of ball milled Ni-Si alloys while when

the Si content is low (<60 at.%), NiSi peaks can be observed [111]. In Figure 6.14, Ni, NiSi and Ni_2Si peaks were identified in the XRD patterns of Ni1 before and after delithiation, indicative of the reaction between Ni and Si during ball milling. No Li-Si compound peaks were observed in the Ni1 alloy, presumably because the Li-Si compound became amorphous. After delithiation, no Si peaks were observed. Presumably the Si phase expected to be produced after delithiation was also amorphous.

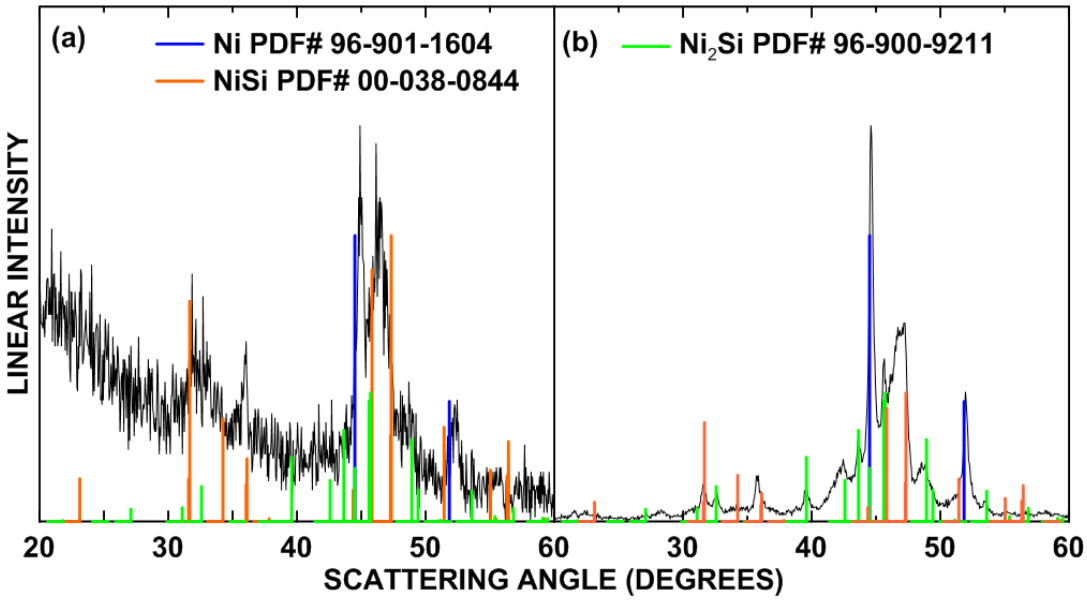

Figure 6.14 XRD patterns of (a) Ni1 and (b) $Ni_{72}Si_{28}$.

Figure 6.15 show the XRD patterns of the Cu1 alloy before and after delithiation. In the XRD pattern of Cu1 shown in Figure 6.15(a), Cu peaks were observed while no Cu-Si compound peaks were detected. The peak near 45 degrees might be from an Fe impurity introduced from the stainless steel balls during ball milling. No Li-Si compound peaks were observed in the XRD pattern of Cu1, indicative of amorphous Li-Si phase/phases. More peaks were observed after the Cu1 alloy was delithiated, as shown in

Figure 6.15(b). These peaks were identified to be Cu, Fe, Cu_3Si and Cu_5Si, and, apart from the Fe impurity, are consistent with previous studies [82, 109, 110]. No Si peaks were detected. Presumably, any Si phase present is in an amorphous state.

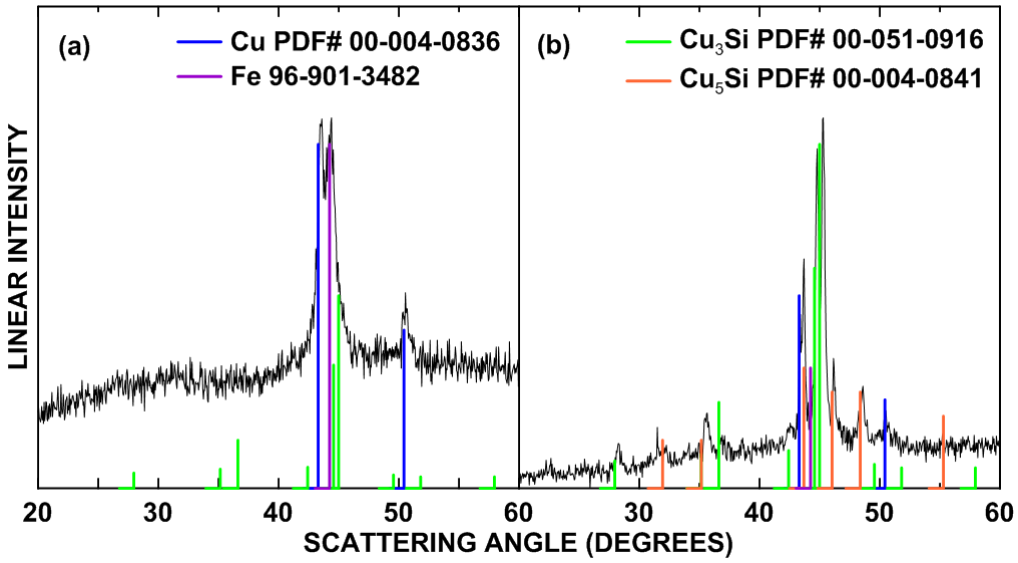

Figure 6.15 XRD patterns of (a) Cu1 and (b) $Cu_{72}Si_{28}$.

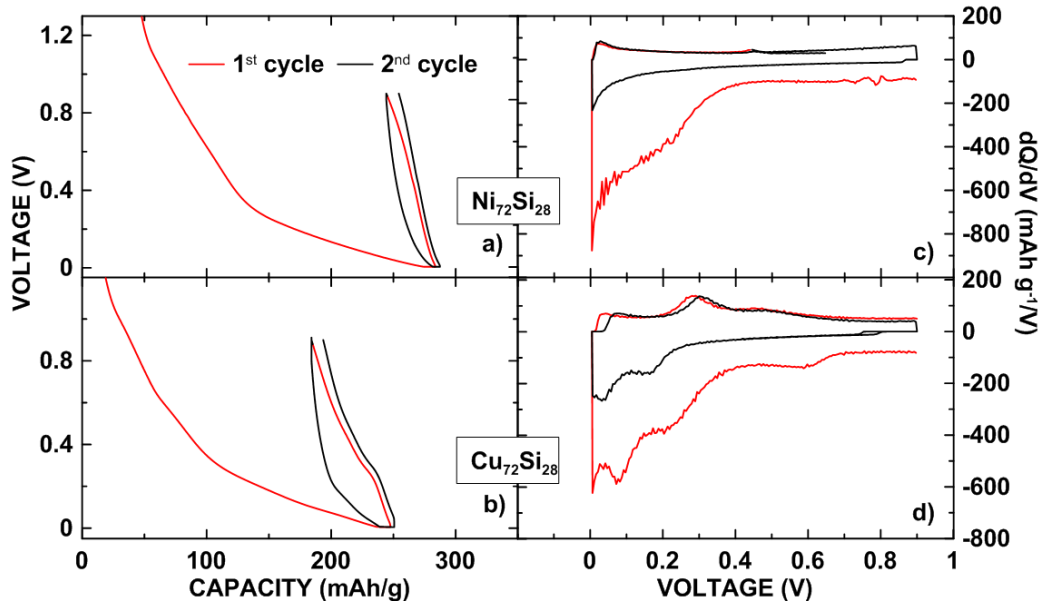

Figure 6.16 (a-b) Voltage curves of $Ni_{72}Si_{28}$ and $Cu_{72}Si_{28}$ electrodes and (c-d) differential capacity curves of $Ni_{72}Si_{28}$ and $Cu_{72}Si_{28}$ electrodes.

Figure 6.16 shows the voltage curves and differential capacity curves of $Ni_{72}Si_{28}$ and $Cu_{72}Si_{28}$ electrodes. $Ni_{72}Si_{28}$ electrode has no distinct differential capacity peaks or voltage plateaus, as shown in Figure 6.16 (a) and (c). In comparison, the $Cu_{72}Si_{28}$ electrode has two broad differential capacity peaks near 0.2 V and 0.05 V during lithiation and another two broad peaks near 0.3 V and 0.45 V during delithiation, indicative of a-Si lithiation and a-Li_xSi delithiation. Correspondingly, there are also two sloping voltage plateaus near 0.5 V and 0.2 V during lithiation and another two voltage plateaus near 0.7 V and 0.3 V during delithiation.

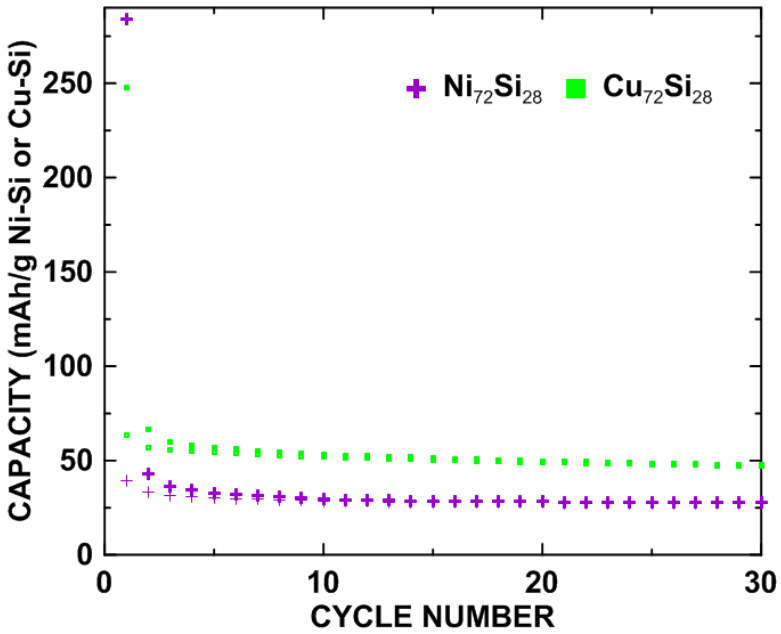

Figure 6.17 Cycling performance of $Ni_{72}Si_{28}$ and $Cu_{72}Si_{28}$ electrodes.

When cycled as in Li cells, $Ni_{72}Si_{28}$ and $Cu_{72}Si_{28}$ alloys displayed stable cycling performance but low capacity as shown in Figure 6.17. The low capacity might be due to most of the Si reacting with Ni or Cu during ball milling, resulting in only a small amount

of active Si left. Du *et al*. studied sputtered thin film Ni-Si system ($0 \leq x \leq 0.65$ in Ni_xSi_{1-x}) [83]. They found when the Si content was low ($0.5 > x$ in Ni_xSi_{1-x}), the Ni-Si electrode also showed low reversible capacity. In comparison, when the Si content increased ($0.5 \leq x$ in Ni_xSi_{1-x}), the Ni-Si electrode displayed higher reversible capacity. It is speculated that if the Si content increased in Ni-Si alloys prepared in this study, higher capacity could be achieved. Kim *et al*. prepared Cu-deposited Si powder as negative electrodes [82]. The as-prepared Cu-Si electrodes displayed high reversible capacities (1400~2300 mAh/g). However, these Cu-Si electrodes had poor cycling performance. In this study, the $Cu_{72}Si_{28}$ electrode displayed stable cycling performance though its capacity was low. It is speculated that improved capacity could be achieved by increasing the Si content in Cu-Si alloys prepared in this study.

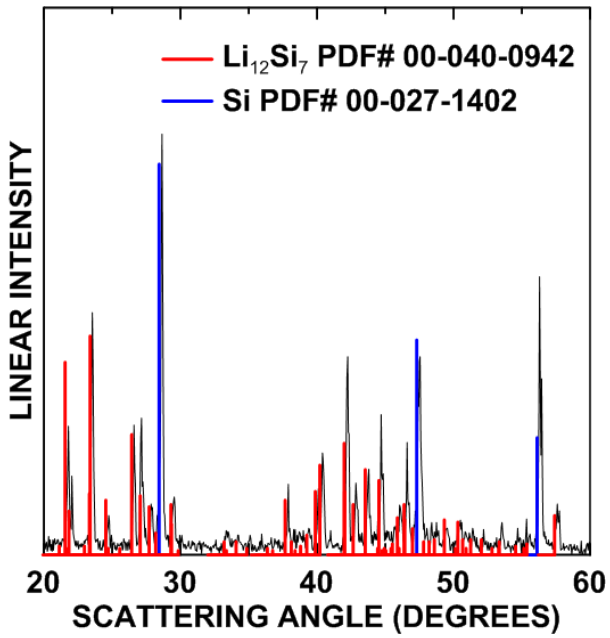

Figure 6.18 XRD pattern of LiSi prepared with an arc furnace.

Li-Metal-Si precursors prepared with LiSi were labeled as Ni2 and Cu2 as shown in Table 6.2. Red stars in Figure 6.13 represent the compositions of Ni2 and Cu2. Figure 6.18 shows the XRD pattern of LiSi prepared with an arc furnace. Though there is a LiSi phase shown in the Li-Si binary system in Figure 2.4, the as-prepared LiSi was identified to be a mixture of $Li_{12}Si_7$ and crystalline Si. Figure 6.19 shows the XRD patterns of the Ni2 and Cu2 samples synthesized by ball milling and their products of ethanol delithiation. The XRD patterns of the Ni2 and Cu2 samples match well with the reference peaks of $LiNi_2Si$ and $LiCu_2Si$ compounds, respectively. After ethanol delithiation, the positions of experimental peaks remained unchanged, with slight change of peak intensity. Bubbles were observed during chemical delithiation of Ni2 and Cu2, indicating Ni2 and Cu2 reacted with ethanol to produce H_2. One explanation for the slight change in XRD patterns is that ethanol is not an efficient delithiant to extract Li from Ni2 and Cu2 or that the reaction time was not long enough. Another possible reason is that Li has been extracted from Ni2 ($LiNi_2Si$) and Cu2 ($LiCu_2Si$), but the crystal structure of the compounds remained unchanged. If the chemical delithiated compounds can be electrochemically re-lithiated, it should exhibit capacity. Further tests by cycling the chemical delithiated ternary compounds as electrodes in Li cells are in progress to confirm this hypothesis.

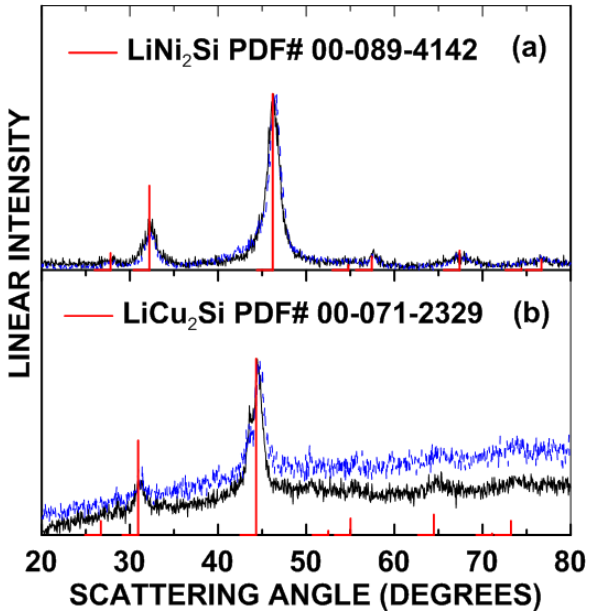

Figure 6.19 XRD patterns of (a) Ni2 and (b) Cu2 before and after delithiation reactions with ethanol. Black lines represent the Li-Metal-Si phases before ethanol delithiation and blue lines represent the Li-Metal-Si phases after ethanol delithiation.

6.4 CONCLUSION

In this chapter, bulk quantities of Fe-Si alloys were prepared by ethanol delithiation of Fe-Li-Si alloys in serial Fe:Si stoichiometric ratios. XRD, SEM, Mössbauer spectra and electrochemical measurements of the Fe-Si alloys were performed and analyzed. The Fe-Si alloys were composed of Fe, FeSi and amorphous Si. Some Fe-Si electrodes displayed lower volume expansion compared to that of bulk cr-Si. This might stem from the porosity within Fe-Si particles being able to accommodate the volume expansion of the Si. Fe-Si alloys also exhibited better cycling performance compared to that of bulk cr-Si. However, the cycling stability of Fe-Si electrodes with

high Si content was poor, presumably from mechanical failure of the alloy particles, of which cr-$Li_{15}Si_4$ formation may be a symptom. The alcohol delithiation method represents an effective means of producing Fe-Si alloys as negative electrode materials for Li cells.

Bulk quantities of $Ni_{72}Si_{28}$ and $Cu_{72}Si_{28}$ alloys were prepared by ethanol delithiation of Ni1 and Cu1 precursors. When used as negative electrodes for Li cells, $Ni_{72}Si_{28}$ and $Cu_{72}Si_{28}$ electrodes displayed stable cycling performance but low capacity. It is speculated that by increasing the Si content in Ni-Si and Cu-Si alloys, higher capacity could be achieved.

Ni2 and Cu2 compounds were synthesized as precursors to prepare Ni-Si/Cu-Si materials with the ethanol delithiation method. The Ni2 and Cu2 compounds were identified as $LiNi_2Si$ and $LiCu_2Si$ by XRD measurements. However, the XRD patterns of Ni2 and Cu2 were changed little after ethanol delithiation. Further investigations, including utilizing the delithiated compounds as negative electrodes in Li cells, are in progress.

CHAPTER 7 CONCLUSION

The objective of this work was to study Si-based alloys as negative electrode materials for Li-ion batteries. Previous studies have shown a number of methods to prepare nano-structured Si [38-43], C-Si alloys [44-46] and (Si active) / inactive alloys [47] as negative electrodes for Li cells. In this thesis work, a chemical delithiation method was described to prepare amorphous Si. This method was also utilized to synthesize C-Si and Metal-Si alloys as Li-ion battery negative electrodes.

7.1 CONCLUSION

The chemical delithiation method was detailed discussed in Chapter 4. Bulk quantities of amorphous silicon were prepared by alcohol delithiation of Li-Si compounds. Both ethanol and isopropanol were used for this purpose. Ethanol was found to be a more convenient delithiant than isopropanol and resulted in higher yields and products having superior cycling performance. Amorphous Si prepared from ethanol delithiation of $Li_{12}Si_7$, Li_7Si_3, $Li_{13}Si_4$ and $Li_{22}Si_5$ resulted in layered products, except in the case of $Li_{22}Si_5$, which was composed of dense particles. Amorphous Si prepared from ethanol delithiation of $Li_{12}Si_7$ had the most orderly layered structure, with the layers being highly exfoliated. All amorphous Si samples prepared from delithiation had superior cycling performance compared to that of crystalline Si. This may be attributed to the low volume expansion (as low as 52 %) measured for these particles during cycling. It is thought that the porous layered structure of these materials can accommodate the Si volume expansion during lithiation, resulting in low overall particle

expansion. When heated to high temperatures, the layered structure collapsed and cycling performance deteriorated as a result.

Applications of the chemical delithiation method for the synthesis of Si alloys were discussed in Chapter 5 and 6. In Chapter 5, bulk quantities of C-Si alloys were prepared by ethanol delithiation of C-Li-Si precursors in serial C:Si stoichiometric ratios. XRD, SEM and electrochemical measurements were performed and analyzed. C-Si electrodes exhibited lower volume expansion (as low as 21%) compared to that of bulk crystalline Si. This might account from the carbon matrix working as a diluent and the hollows formed within C-Si alloys accommodating the volume expansion of the Si phase. C-Si alloys also exhibited superior cycling performance than that of bulk crystalline Si. After 50 cycles at C/20 rate, the capacity of cells with C-Si electrodes remained as high as 1800 mAh/g. The differential capacity curves show that no transition occurs between crystalline $Li_{15}Si_4$ and amorphous lithiated silicon when the voltage was below 0.05 V. A model was proposed to illustrate the structure transitions of C-Li-Si alloys during ethanol delithiation and of C-Si alloys during electrochemical lithiation/delithiation.

In Chapter 6, bulk quantities of Fe-Si alloys were prepared by ethanol delithiation of Fe-Li-Si alloys in serial Fe:Si stoichiometric ratios. XRD, SEM, Mössbauer spectra and electrochemical measurements of the Fe-Si alloys were performed and analyzed. The Fe-Si alloys were found to be composed of Fe, FeSi and amorphous Si. Some Fe-Si electrodes displayed lower volume expansion compared to that of bulk crystalline Si. This might stem from that the porosity within Fe-Si particles being able to dilute the

volume expansion of the active Si phase. Fe-Si alloys also exhibited better cycling performance than that of bulk crystalline Si. However, the cycling stability of Fe-Si electrodes with high Si content was poor, presumably from mechanical failure of the alloy particles, of which the formation of $Li_{15}Si_4$ may be a symptom. A model was proposed to illustrate the structure transitions of Fe-Li-Si alloys during ethanol delithiation and of Fe-Si alloys during electrochemical lithiation/delithiation.

The ethanol delithiation method represents an effective means of producing C-Si and Fe-Si alloys with low volume expansion, good cycling performance and high capacity.

In Chapter 6, bulk quantities of $Ni_{72}Si_{28}$ and $Cu_{72}Si_{28}$ alloys were prepared by ethanol delithiation of Ni1 and Cu1 precursors. $Ni_{72}Si_{28}$ and $Cu_{72}Si_{28}$ electrodes displayed stable cycling performance but low capacity when cycled in Li cells. It is speculated that by increasing the Si content in Ni-Si and C-Si alloys, higher capacity could be achieved.

Ni2 ($LiNi_2Si$) and Cu2 ($LiCu_2Si$) compounds were also synthesized as precursors to prepare Ni-Si/Cu-Si materials with ethanol delithiation method as described in Chapter 6. However, the XRD patterns of the Ni2 ($LiNi_2Si$) and Cu2 ($LiCu_2Si$) compounds have small changes before and after ethanol delithiation.

7.2 Ongoing and Future Work

In Chapter 5, one narrow peak was observed in the XRD patterns of some C-Si alloys ($C_{60}Si_{40}$, $C_{50}Si_{50}$, and $C_{40}Si_{60}$) as shown in Figure 5.3(j-l). This peak is speculated

to be from FeSi or Fe impurities, where the Fe is introduced from stainless steel balls during ball milling. However, it was difficult to identify the impurity and its content just according to the XRD patterns. Further tests by inductively coupled plasma (ICP) analysis and Mössbauer spectroscopy are in progress to confirm the Fe impurity identity and its content.

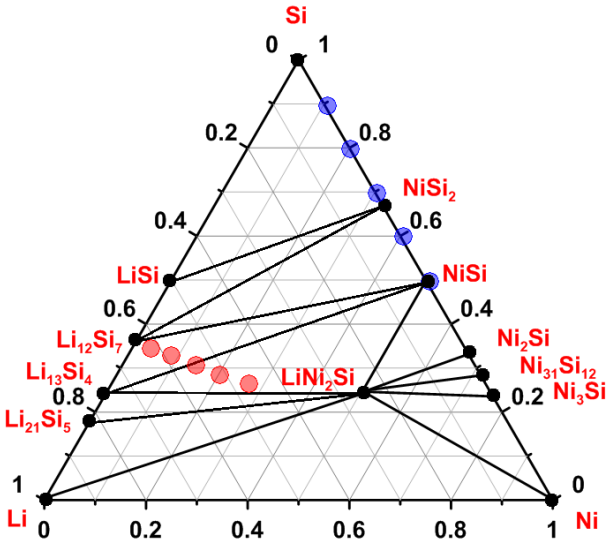

Figure 7.1 The Li-Ni-Si and ternary systems at 0 K as predicted by the Materials Project [103, 104]. Red dots represent the compositions of Li-Ni-Si alloys that will be prepared by ball milling $Li_{12}Si_7$ and Ni powder in future work; blue dots represent the compositions of Ni-Si alloys by ethanol delithiation of Li-Ni-Si alloys.

In Chapter 6, Fe-Si alloys in serial stoichiometric ratios were prepared and tested as negative electrodes. However, only one Ni-Si ($Ni_{72}Si_{28}$) alloy and one Cu-Si ($Cu_{72}Si_{28}$) alloy were synthesized. XRD and electrochemical measurements of the $Ni_{72}Si_{28}$ and $Cu_{72}Si_{28}$ alloys were performed and analyzed. The $Ni_{72}Si_{28}$ and $Cu_{72}Si_{28}$

electrodes displayed stable cycling performance but low capacity. In Reference 83, Ni-Si alloys ($0 \leq x \leq 0.65$ in Ni_xSi_{1-x}) prepared by sputtering displayed superior electrochemical performance than that of crystalline Si. Low capacity was obtained when Ni content was more than 50 at.% because at this composition the lithiation voltage was suppressed to below 0 V. In Reference 106, Ni_xSi_{1-x} alloys ($0 \leq x \leq 0.5$) prepared by ball milling displayed stable cycling performance even when silicon content is high (80 at.%). In future work, Ni-Si alloys composed of more Si content (Si content more than 50 at.%) should be prepared from Li-Ni-Si alloys by ethanol delithiation, as shown in Figure 7.1, and tested as negative electrodes in Li cells.

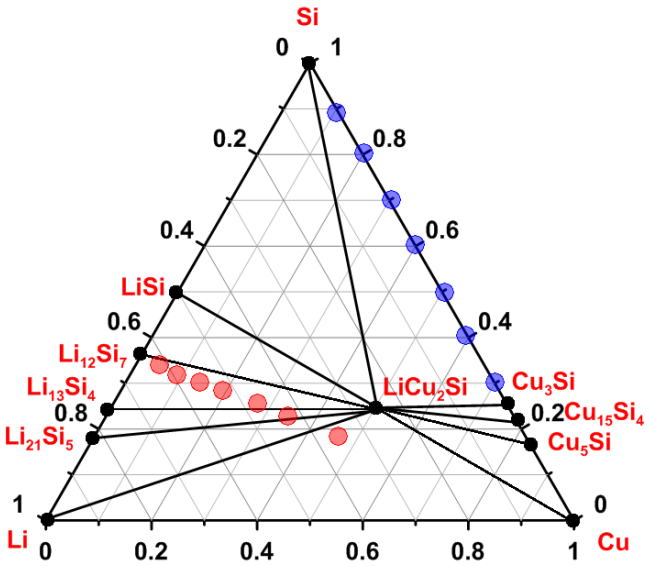

Figure 7.2 The Cu-Li-Si and ternary systems at 0 K as predicted by the Materials Project [103, 104]. Red dots represent the compositions of Cu-Li-Si alloys that will be prepared by ball milling $Li_{12}Si_7$ and Cu powder in future work; blue dots represent the compositions of Cu-Si alloys by ethanol delithiation of Cu-Li-Si alloys.

The $Cu_{72}Si_{28}$ electrode displayed stable cycling performance in Chapter 6. However, its capacity is low. In future work, Cu-Si alloys composed of more Si content should be prepared from Cu-Li-Si alloys by ethanol delithiation, and tested as negative electrodes as shown in Figure 7.2.

Besides XRD and electrochemical measurements, SEM should also be performed to analyze the morphology and particle size of Cu-Si and Ni-Si alloys. The expansion of Ni-Si and Cu-Si electrodes should also be measured.

In Chapter 6, $LiNi_2Si$ and $LiCu_2Si$ ternary compounds were prepared by ball milling LiSi with Ni or Cu powder. The XRD patterns of $LiNi_2Si$ and $LiCu_2Si$ compounds before and after ethanol delithiation have small changes. Further measurements, including utilizing the delithiated ternary compounds as negative electrodes in Li cells, are in progress. If it turns out that the delithiated ternary compounds do not have capacity, then ethanol might not be an effective delithiant. If in this case, other solutions should be tried as delithiants for these compounds, such as acetic acid or water.

The synthesis of C-Si or Metal-Si alloys by the chemical delithiation method introduced in this thesis has never been previously reported. This method provides a new direction to prepare Si-based alloys from Li-Metal-Si precursors as negative electrodes for Li-ion batteries. Besides C, Fe, Ni and Cu, other materials can be used to prepare Si-based alloys from Li-Metal-Si precursors with this method, such as Co. In a previous study, Co-Si alloys have displayed improved cycling performance compared to that of

crystalline Si [119]. Li-Si-X-Y precursors can also be prepared by ball milling Li-Si with two types of materials and then delithiated to prepare Si-X-Y alloys as negative electrodes of Li-ion cells. Cu-Fe-Si alloys have displayed improved cycling performance than that of crystalline Si in a previous study [120].

Mg-Si-X, Ca-Si-X and Na-Si-X alloys, besides Li-Si-X, can also be prepared by ball milling Mg-Si, Ca-Si or Na-Si compounds with other materials and then de-alloyed with proper oxidizing solvents. These studies have never been reported before. It would be of technical importance for the development of Li-ion battery negative electrodes to investigate the applications of the chemical de-alloying method in other ternary systems (Mg-Si-X, Ca-Si-X and Na-Si-X, *etc.*).

References

[1] ICT Facts and Figures - The world in 2015, ITU (2015).

[2] M. Yoshio, R. J. Brodd, and A. Kozawa, *Lithium-Ion Batteries Science and Technologies*, Springer (2009).

[3] B. Scrosati, J. Hassoun, and Y.-K. Sun, *Energy Environ. Sci.*, **4**, 3287 (2011).

[4] T.B. Reddy, *Linden's Handbook of Batteries 4th Edition,* McGraw Hill Professional (2011).

[5] J. M. Tarascon and M. Armand, *Nature*, **414**, 359 (2001).

[6] http://www.teslamotors.com (accessed September 2, 2015).

[7] http://www.byd.com/na/auto/e6.html (accessed September 2, 2015).

[8] C. Pillot, AVICENNE Energy market review, 2014. http://www.rechargebatteries.org/wp-content/uploads/2015/01/Avicenne-market-review-Nive-2014.pdf (accessed September 2, 2015).

[9] M. N. Obrovac and V. L. Chevrier, *Chem. Rev.*, **114**, 11444 (2014).

[10] G. Pancaldi, *Volta: Science and culture in the age of enlightenment*, Princeton University Press (2005).

[11] B. Scrosati and J. Garche. *J. Power Sources,* **195**, 2419 (2010).

[12] D. Aurbach, *Nonaqueous Electrochemistry 1st edition*, CRC Press (1999).

[13] T. Zheng, J. N. Reimers, and J. R. Dahn, *Phys. Rev. B*, **51**, 734 (1995).

[14] H. Selig and L. B. Ebert, *Adv. Inorg. Chem. Radiochem*., **23**, 281 (1980).

[15] K. M. Colbow, R. R. Haering, and J. R. Dahn, *J. Power Sources* **26**, 397 (1989).

[16] T. Ohzuku, A. Ueda, and N. Yamamoto, *J. Electrochem. Soc.*, **142**, 1431 (1995).

[17] W. J. Zhang, *J. Power Sources*, **196**, 5674 (2011).

[18] M. T. McDowell, S. W. Lee, W. D. Nix, and Y. Cui, *Adv. Mater*., **25**, 4966 (2013).

[19] B. Liang, Y. Liu, and Y. Xu, *J. Power Sources*, **267**, 469 (2014).

[20] C.-M. Park, J.-H. Kim, H. Kim, and H.-J. Sohn, *Chem. Soc. Rev*., **39**, 3115 (2010).

[21] A. Ulus, Y. Rosenberg, L. Burstein, and E. Peled, *J. Electrochem. Soc*., **149**, A635 (2002).

[22] H. Kim, J. Choi, H. J. Sohn, and T. Kang, *J. Electrochem. Soc*., **146**, 4401 (1999).

[23] M. Wachtler, J. O. Besenhard, and M. Winter, *J. Power Sources*, **94**, 189 (2001).

[24] H. Zhao, Z. Zhu, C. Yin, H. Guo, and D. H. L. Ng, *Mater. Chem. Phys*., **110**, 201 (2008).

[25] J. Yang, M. Wachtler, M. Winter, and J. O. Besenhard, *Electrochem. Solid-State Lett.*, **2**, 161 (1999).

[26] H. Li, L. Shi, W. Lu, X. Huang, and L. Chen, *J. Electrochem. Soc*., **148**, A915 (2001).

[27] C. J. Wen and R. A. Huggins, *J. Solid State Chem*., **37**, 271 (1981).

[28] M. H. Braga, M. Helena, A. Dębski, and W. Gąsior, *J. Alloys Comp*, **616**, 581 (2014).

[29] M. N. Obrovac and L. Christensen, *Electrochem. Solid-State Lett*., **7**, A93 (2004).

[30] J. Li and J. R. Dahn, *J. Electrochem. Soc*., **154**, A156 (2007).

[31] M. N. Obrovac and L. J. Krause, *J. Electrochem. Soc*., **154**, A103 (2007).

[32] S. P. V. Nadimpalli, V. A. Sethuraman, S. Dalavi, B. Lucht, M. J. Chon, V. B. Shenoy, and P. R. Guduru, *J. Power Sources*, **215**, 145 (2012).

[33] V. A. Sethuraman, V. Srinivasan, and J. Newman, *J. Electrochem. Soc.*, **160**, A394 (2013).

[34] V. L. Chevrier and J. R. Dahn, *J. Electrochem. Soc*., **157**, A392 (2010).

[35] L. Baggetto, R. A. H. Niessen, F. Roozeboom, and P. H. L. Notten, *Adv. Funct. Mater*., **18**, 1057 (2008).

[36] V. A. Sethuraman, V. Srinivasan, A. F. Bower, and P. R. Guduru, *J. Electrochem. Soc*., **157**, A1253 (2010).

[37] W. J. Zhang, *J. Power Sources*, **196**, 877 (2011).

[38] W. Wang, R. Epur, and P. N. Kumta, *Electrochem. Commu.*, **13**, 429 (2011).

[39] H. Wu, G. Chan, J. W. Choi, I. Ryu, Y. Yao, M. T. McDowell1, S. W. Lee, A. Jackson, Y. Yang, L. Hu, and Y. Cui, *Nat. Nanotechnol*., **7**, 310 (2012).

[40] L. B. Chen, J. Y. Xie, H. C. Yu, and T. H. Wang, *J. Appl. Electrochem*., **39**, 1157 (2009).

[41] J. P. Maranchi, A. F. Hepp, and P. N. Kumta, *Electrochem*. *Solid-State Lett*., **6**, A198 (2003).

[42] H. Jung, M. Park, Y. Yoon, G. Kim, and S. Joo, *J. Power Sources*, **115**, 346 (2003).

[43] R. Epur, M. Ramanathan, F. R. Beck, A. Manivannan, and P. N. Kumta, *Mat. Sci. Eng. B-Solid*, **177**, 1157 (2012).

[44] D. Wang, M. Gao, H. Pan, J. Wang, and Y. Liu, *J. Power Sources*, **256**, 190 (2014).

[45] Z. Du, R. A. Dunlap, and M. N. Obrovac, *J. Electrochem. Soc*., **161**, A1698 (2014).

[46] S. Jang, J. Miyawaki, M. Tsuji, I. Mochida, and S. Yoon, *Carbon*, **47**, 3383 (2009).

[47] O. Mao, R. L. Turner, I. A. Courtney, B. D. Fredericksen, M. I. Buckett, L. J. Krause, and J. R. Dahn, *Electrochem. Solid-State Lett.*, **2**, 3 (1999).

[48] S. S. Zhang, *J. Power Sources*, **162**, 1379 (2006).

[49] S. Dalavi, P. Guduru, and B. L. Lucht, *J. Electrochem. Soc*., **159**, A642 (2012).

[50] I. Kovalenko, B. Zdyrko, A. Magasinski, B. Hertzberg, Z. Milicev, R. Burtovyy, I. Luzinov, and G. Yushin, *Science*, **334**, 75 (2011).

[51] A. Ammar, C. Cros, M. Pouchard, N. Jaussaud, J. Bassat, G. Villeneuve, M. Duttine, M. Ménétrier, and E. Reny, *Solid State Sci*., **6**, 393 (2004).

[52] P. F. McMillan, J. Gryko, C. Bull, R. Arledge, A. J. Kenyon, and B. A. Cressey, *J. Solid State Chem*. **178**, 937 (2005).

[53] D. Neiner, H. W. Chiu, and S. M. Kauzlarich, *J. Am. Chem. Soc*. **128**, 11016 (2006).

[54] C. Yang, R. Bley, S. Kauzlarich, H. Lee, and G. Delgado, *J. Am. Chem. Soc*., **121**, 5191 (1999).

[55] L. Wang, N. Lin, J. Zhou, Y. Zhu, and Y. Qian, *Chem. Commun*., **51**, 2345 (2015).

[56] Y. Hwa, W. Kim, B. Yu, J. Kim, S. Hong, and H. Sohn, *J. Power Sources*, **252**, 144 (2014).

[57] R. Epur, L. Minardi, M. Datta, S. Chung, and P. Kumta, *J. Solid State Chem*., **208**, 93 (2013).

[58] J. Liang, X. Li, Z. Hou, C. Guo, Y. Zhu, and Y. Qian, *Chem. Commun*., **51**, 7230 (2015).

[59] H. Nakano, *J. Ceram. Soc. Jpn.,* **122**, 748 (2014).

[60] M. R. Tchalala, M. A. Ali, H. Enriquez, A. Kara, A. Lachgar, S. Yagoubi, E. Foy, E.Vega, A. Bendounan, M. G. Silly, F. Sirotti, S. Nitshe, D. Chaudanson, H. Jamgotchian, B. Aufray, A. J. Mayne, G. Dujardin, and H. Oughaddou, *J. Phys. Condens. Matter*, **25**, 442001 (2013).

[61] K. Xu, L. Ben, H. Li, and X. Huang, In press.

[62] M. Zeilinger, L. A. Jantke, L. M. Scherf, F. J. Kiefer, G. Neubüser, L. Kienle, A. J. Karttunen, S. Konar, U. Häussermann, and T. F. Fässler, *Chem. Mater.*, **26**, 6603 (2014).

[63] K. Annou, M. Pelosi, G. Gershinsky, F. Favier, Y. Cuminal, M. Tillard, and D. Zitoun, *Mater. Renew. Sustain. Energy*, **3**, 1 (2014).

[64] H. Y. Lee and S. M. Lee, *J. Power Sources*, **112**, 649 (2002).

[65] M. Yoshio, T. Tsumura, and N. Dimov, *J. Power Sources*, **146**, 10 (2005).

[66] S. Hwang, C. Cho, and H. Kim, *Electrochim. Acta*, **55**, 3236 (2010).

[67] Y. Liu, Z. Y. Wen, X. Y. Wang, A. Hirano, N. Imanishi, and Y. Takeda, *J. Power Sources*, **189**, 733 (2009).

[68] M. K. Datta and P. N. Kumta, *J. Power Sources*, **165**, 368 (2007).

[69] M. L. Terranova, S. Orlanducci, E. Tamburri, V. Guglielmotti, and M. Rossi, *J. Power Sources*, **246**, 167 (2014).

[70] Y. Yin, S. Xin, L. Wan, C. Li, and Y. Guo, *J. Phys. Chem. C*, **115**, 14148 (2011).

[71] C. Paireau, S. Jouanneau, M.-R. Ammar, P. Simon, F. Béguin, and E. Raymundo-Piñero, *Electrochim. Acta*, **174**, 361 (2015).

[72] M. Holzapfel, H. Buqa, F. Krumeich, P. Novak, F-M. Petrat, and C. Veit, *Electrochem. Solid-State Lett.*, **8**, A516 (2005).

[73] H. Tao, L. Fan, W. Song, M. Wu, X. He, and X. Qu, *Nanoscale*, **6,** 3138 (2014).

[74] X. Li, P. Meduri, X. Chen, W. Qi, M. H. Engelhard, W. Xu, F. Ding, J. Xiao, W. Wang, C. Wang, J. Zhang, and J. Liu, *J. Mater. Chem.*, **22**, 11017 (2012).

[75] V. L. Chevrier, L. Liu, D. B. Le, J. Lund, B. Molla, K. Reimer, L. J. Krause, L. D. Jensen, E. Figgemeier, and K. W. Eberman, *J. Electrochem. Soc*., **161**, A783 (2014).

[76] G. X. Wang, L. Sun, D. H. Bradhurst, S. Zhong, S. X. Dou, and H. K. Liu, *J. Power Sources*, **88**, 278 (2000).

[77] A. Netz, R. A. Huggins, and W. Weppner, *J. Power Sources*, **119**, 95 (2003).

[78] A. Netz and R. A. Huggins, *Solid State Ionics*, **175**, 215 (2004).

[79] T. Li, Y. L. Cao, X. P. Ai, and H. X. Yang, *J. Power Sources*, **184**, 473 (2008).

[80] M. Fleischauer, J. Topple, and J. R. Dahn, *Electrochem. Solid-State Lett.*, **8**, A137 (2005).

[81] X. Zhao, R. A. Dunlap, and M. N. Obrovac. *J. Electrochem. Soc.* **161**, A1976 (2014).

[82] J. W. Kim, J. H. Ryu, K. T. Lee, and S. M. Oh, *J. Power Sources*, **147**, 227 (2005).

[83] Z. Du, T. D. Hatchard, R. A. Dunlap, and M. N. Obrovac, *J. Electrochem. Soc.*, **162**, A1858 (2015).

[84] A. Anani and R. A. Huggins, *J. Power Sources*, **38**, 351 (1992).

[85] A. Anani and R. A. Huggins, *J. Power Sources*, **38**, 363 (1992).

[86] B. D. Culity, *Elements of X-ray Diffraction 2nd edition*, Addison-Wesley Longman Inc (1978).

[87] R. D. Deslattes, E. G. Kessler Jr., P. Indelicato, L. de Billy, E. Lindroth, and J. Anton, *Rev. Mod. Phys.*, **75**, 35 (2003).

[88] R. Brundle, C. Evans, and S. Wilson, *Encyclopedia of materials characterization*, Gulf Professional (1992).

[89] N.N. Greenwood and T.C. Gibb. *Mössbauer Spectroscopy*, Chapman and Hall Ltd., London (1971).

[90] R. Mossbauer, *Nobel lecture* (1961).

[91] http://www.rsc.org/membership/networking/interestgroups/mossbauerspect/intro.asp (accessed October 1, 2015).

[92] R. B. Firestone, *Table of Isotopes 8th Edition* (Wiley-Interscience, 1996).

[93] T. Marks, S. Trussler, A. J. Smith, D. Xiong, and J. R. Dahn, *J. Electrochem. Soc.*, **158**, A51 (2011).

[94] A. M. Wilson and J. R. Dahn, *J. Electrochem. Soc*., **142**, 326 (1995).

[95] M. N. Obrovac. "Nanostructured Electrode Materials for Lithium Ion Batteries." Ph.D. thesis. Dalhousie University (2001).

[96] V.L. Chevrier, J.W. Zwanziger, and J.R. Dahn, *J. Alloys Compd.*, **496**, 25 (2010).

[97] S. Dupke, T. Langer, R. Pöttgen, M. Winter, S. Passerini, and H. Eckert, *PCCP*, **14**, 6496 (2012).

[98] K. Momma and F. Izumi, *J. Appl. Crystallogr*., **41**, 653 (2008).

[99] H. Axel, H. Schäfer, and A. Weiss, *Z. Naturforsch. B*, **21**, 115 (1966).

[100] H. Van Leuken, G.A. De Wijs, W. Van der Lugt, and R.A. De Groot, *Phys. Rev. B*, **53**, 10599 (1996).

[101] R. W. Olesinski and G. J. Abbaschian, *J. Phase Equilibria*, **5**, 486 (1984).

[102] F. Disma, L. Aymard, L. Dupont, and J-M. Tarascon, *J. Electrochem. Soc.*, **143**, 3959 (1996).

[103] A. Jain, S. P. Ong, G. Hautier, W. Chen, W. D. Richards, S. Dacek, S. Cholia, D. Gunter, D. Skinner, G. Ceder, and K. A. Persson, *Appl. Phys. Lett. Mater.*, **1**, 011002 (2013).

[104] P. Ong, W. D. Richards, A. Jain, G. Hautier, M. Kocher, S. Cholia, D. Gunter, V. L. Chevrier, K. A. Persson, and G. Ceder, *Comp. Mater. Sci.*, **68**, 314 (2013).

[105] Z. G. Yang and L. L. Shaw, *Nanostruct. Mater.*, **7**, 873 (1996).

[106] J. R. Dahn, *Phys. Rev. B*, **44**, 9170 (1991).

[107] T. D. Hatchard and J. R. Dahn, *J. Electrochem. Soc.*, **151**, A838 (2004).

[108] M. N. Obrovac, L. Christensen, Dinh Ba Le, and J. R. Dahn, *J. Electrochem. Soc.*, **154**, A849 (2007).

[109] Y. NuLi, B. Wang, J. Yang, X. Yuan, and Z Ma. *J. Power Sources,* **153**, 371 (2006).

[110] P. Zuo, G. Yin, X. Hao, Z. Yang, Y. Ma, and Z. Gao. *Mater. Chem. Phys.,* **104**, 444 (2007).

[111] Z. Du, S. N. Ellis, R. A. Dunlap, and M. N. Obrovac. *J. Electrochem. Soc.*, **163**, A13 (2016).

[112] H. Okamoto, *Phase diagrams of binary iron alloys*, ASM International, (1993).

[113] P. Nash and A. Nash, *Bull Alloy Phase Diagr*, **8**, 6 (1987).

[114] R. W. Olesinski and G. J. Abbaschian, *Bull Alloy Phase Diagr*, **7**, 170 (1986).

[115] K. Vojtěchovský and T. Zemčík, *Czech. J. Phys. B*, **24**, 171 (1974).

[116] J. Desimoni and F. H. Sanchez, *Hyperfine Interact.*, **122**, 277 (1999).

[117] J. D. McGraw, M. D. Fleischauer, J. R. Dahn, and R. A. Dunlap, *Philos. Mag*., **86**, 5017 (2006).

[118] I. Dézsi, C. Fetzer, L. Bujdosó, J. Brötz, and A. G. Balogh, *J. Alloys Compd*., **508**, 51 (2010).

[119] Y. Kim, H. Lee, S. Jang, S. Lim, S. Lee, H. Baik, Y. Yoon, and S. Lee. *Electrochim. Acta*, **48**, 2593 (2003).

[120] C. Doh, H. Shin, D. Kim, Y. Jeong, S. Moon, B. Jin, H. Kim, K. Kim, D. Oh, and A. Veluchamy, *J. Alloys Compd.*, **461**, 321 (2008).